

POLITECNICO DI TORINO

Master of Science in Biomedical Engineering

Master Thesis

Using IMUs for the assessment of knee
flex-extension angle in presence of
soft tissue artefacts



Supervisors

Prof. Laura Gastaldi

Ing. Valeria Rosso

Ing. Elisa Digo

Prof. Stefano Pastorelli

Candidate

Clara Gino

March 2021

TABLE OF CONTENTS

1. ABSTRACT	3
2. INTRODUCTION TO GAIT ANALYSIS	5
2.1. GAIT ANALYSIS WITH INERTIAL SENSORS	9
2.1.1. INERTIAL SENSORS ORIENTATION	10
2.1.2. CENTRE OF ROTATION ESTIMATION	13
2.1.3. SENSORS PLACEMENT	16
2.2. KALMAN FILTER AND POSSIBLE ALTERNATIVE METHODS	18
2.3. INERTIAL SENSOR IN CHILDREN MOVEMENT ANALYSIS	22
2.4. OVERWEIGHT CHILDREN GAIT CHARACTERISTICS	27
3. MATERIALS AND METHODS	31
3.1. MATERIALS	31
3.1.1. POLYCENTRIC KNEE JOINT MODEL	31
3.1.2. XSSENS MTx INERTIAL SENSORS	33
3.1.3. SILICON IMPLANTS	37
3.1.4. KINOVEA SOFTWARE	44
3.2. METHODS	47
3.2.1. PROTOCOL: PRELIMINARY TESTS	47
3.2.2. PROTOCOL: EXPERIMENTAL TEST	50
3.2.3. DATA ANALYSIS: KNEE ANGLE ESTIMATION	53
4. RESULTS	63
4.1. PRELIMINARY TEST	63
4.2. EXPERIMENTAL TRIALS	69
4.2.1. XSSENS RESULTS	67
4.2.2. IMUFILTER RESULTS	71
5. CONCLUSION	91
6. REFERENCES	93

1. ABSTRACT

Overweight people commonly conduct a sedentary lifestyle because of difficulties in walking. To quantitatively monitor their gait and reduce soft tissue artefacts, optoelectronic systems are usually adopted, but also inertial measurement units (IMUs) have shown promising results. Considering overweight children, the long preparation time of optoelectronic systems could be a disadvantage. On the contrary, IMUs could simplify the walking acquisition protocol.

In light of these considerations, a pilot study was conducted exploring the use of IMUs during the flex-extension of a polycentric knee model in presence and absence of simulate soft tissue. In detail, the aims of the work were: (i) to evaluate the filtering effect on knee flex-extension movements calculated using IMUs, and (ii) to calculate knee flex-extension movements from linear acceleration and angular velocity of lower limb segments.

Two silicone implants were obtained using silicone ECOFLEX 0030, which mimics soft tissue properties. The two implants had different size to fit the thigh (diameter 9.5-10.5 cm, thickness 3.5 cm) and the shank (diameter 9 cm, thickness 2.5 cm) segments, respectively. The implants were fixed on the lateral part of the thigh and the frontal part of the shank of the polycentric knee model. Three knee flex-extension trials were performed: (1) thigh segment kept steady in horizontal direction and shank segment moving, (2) thigh segment kept steady in vertical direction and shank segment moving, (3) shank segment kept steady in vertical position and thigh segment moving. For each trial, two Xsens IMUs were fixed on the thigh and two on the shank: (i) one on the rigid segment and (ii) one on the implant. In addition, one Xsens sensor was fixed on the ground as reference.

For comparing knee flex-extension movements in presence and absence of soft tissue, Xsens orientation data calibrated with an internal Kalman filter were used. Rotation matrices of each IMU sensor were first referred to a static position. Then, knee flex-extension angle was calculated from the relative orientation between IMUs on the shank and on the thigh. This procedure was repeated for the sensors on the rigid segments and on the implant. Results showed very similar trends in presence and absence of soft tissue.

To calculate knee flex-extension movements from linear acceleration and angular velocity of lower limb segments, the raw data collected with Xsens were used. A procedure consisting of sensor fusion and a Kalman filter was implemented both for IMUs on the rigid segments and on the implant. This post-processing allowed comparing results obtained from raw data to those obtained from Xsens showing an overall agreement and even an improvement in some condition, particularly for angle estimated from sensors on the implants. It should be noted that filter implemented for fusion sensor's

data depend deeply to the initial properties set. In addition, it is possible to observe that performance of filter could vary significantly with the type of movement considered.

In conclusion, this pilot study showed promising results; however, further investigations on overweight children should be conducted to confirm the suitability of IMUs to assess knee flex-extension angle. Furthermore, future studies could investigate the optimization of *imufilter* parameters suitable for walk trial analysis.

2. INTRODUCTION TO GAIT ANALYSIS

Gait Analysis is the systematic study of human locomotion, through the use of instrumentation to measure body movements and mechanics as well as muscle activity. Daily activities like moving, walking, jumping, running, getting up and sitting are determined by nervous system that controls skeletal-muscular system, letting possible such movements. Gait analysis allows to characterize in an objective and quantitative way human movement, detecting relation between the motion control system and the path dynamics.

Gait analysis is nowadays utilized in different field, mainly divided into two categories: clinical gate assessment and gait research. Clinical applications directly allow to detect pathological behaviour, while gait research aims to improve our understanding of gait in order to improve medical diagnosis or treatment in the future. Gait analysis is also used in the improvement of sports performance and reduction of the number and severity of injuries. [1]

The study of human deambulation starts from identifying a “gait cycle” that represent the time interval between two successive occurrences of one of the repetitive events of locomotion (heel contact, *figure 1*). The human gait cycle is split in two principal phases: the stance phase, when the foot is in contact with the ground, and the swing phase, during which the limb is crossing the counter-lateral limb. These two phases are partially offset between the two legs, determining single-limb support and double-limb-support periods. Others sub-phases are then identified based on foot support.

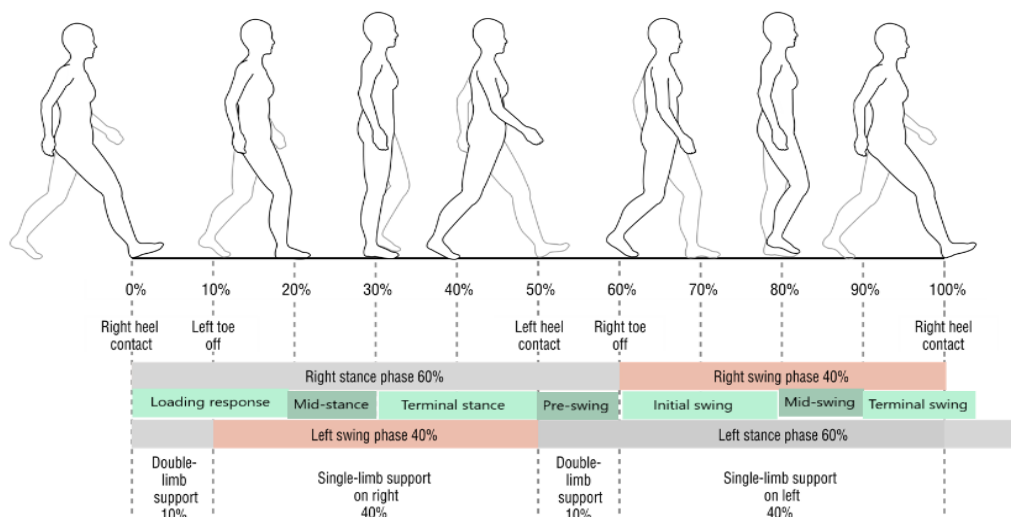


Figure 1 Gait cycle [1]

Spatiotemporal parameters can be considered to describe the gait cycle and to identify standard human walking characteristics. Each of these descriptors can and should be very similar for both limbs in physiological gait. Common parameters generally discussed are:

- Stride time: time for a full gait cycle. Time between successive heel strikes of the same foot
- Step time: time for completion of heel strike of right foot to heel strike of left foot
- Stride length: the distance between two successive heel strikes of the same foot
- Step length: the distance between two successive heel strikes of two different feet
- Step/Base width: the lateral distance between the heel centres of two consecutive foot contacts
- Cadence: number of steps per minute
- Walking/gait speed: distance covered in a given amount of time.

Also, angular parameters are often studied to assess joint movements. Concerning angular parameters, angular displacement, angular velocity, and angular acceleration are considered. The evaluation of this parameters allows to describe human joint movement through kinematic and dynamic analysis. Indeed, by determining angular parameter, study of intra and inter-segment forces of articulation can be conducted.

To evaluate angular parameters, electrogoniometers are usually utilized to measure angle between two segments and then derive angular velocity and acceleration. Electrogoniometers allow kinematic assessment, directly measuring the angle between two segments. Electrogoniometers consist in transducers that transform angular displacement in a measurable signal. Positioning sensors on lateral side of the segments of the joint, the measurement of the angles in sagittal plane are allowed. Electrogoniometers represent a technology easy to use, that do not obstruct natural movements. Nevertheless, their accuracy is limited, and soft tissue artifact can affect measurement.

Since the 1960s gait analysis systems based on optoelectronic techniques has been developed and they are still widely used. These kinematics systems are used in gait analysis to record position and orientation of body segments. Through the identification of spatial position of significant points, during the time, the movement of body segments is reconstructed.

These kinematics systems are used in gait analysis to record the position and orientation of the body segments, the angles of the joints and the corresponding linear and angular velocities and accelerations, through the identification of the spatial position of significant points, called "landmarks". Reflecting markers are utilized to track the position of anatomical points with stereophotogrammetry.

The spatial position of the markers is defined from multiple 2D images using the principle of stereoscopic vision on which optical human system is based. At least two images from two video

cameras in different positions, are needed to define coordinates of the markers (*figure 2*). The recording and the elaboration of the positions allow to also obtain the velocities and the accelerations of the points along the trajectory.

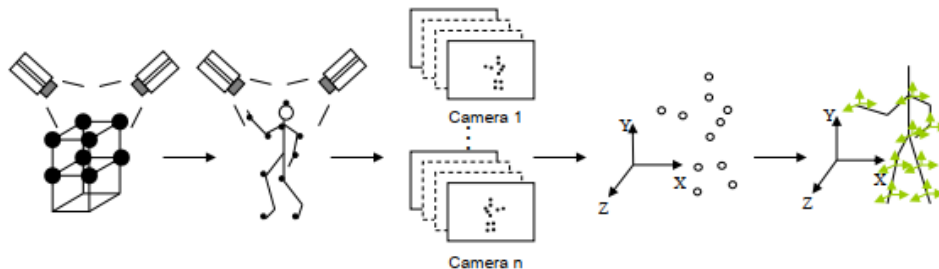


Figure 2 Stereophotogrammetry

This technique nowadays is considered as the gold standard because of its great reliability and accuracy. All data obtained can be referred to an absolute reference system (laboratory reference system) and markers on the body do not cause any obstacles to the movement. Nevertheless, an optoelectronic system presents some important disadvantages, such as it is bound to be used within a laboratory with the appropriate instrumentation, which results to be expensive. An accurate calibration process is also crucial to obtain good results. In addition, it is affected by different types of errors, such as instrumental ones, errors due to determination of landmarks and soft tissue artifacts.

In addition to optical capture systems, there are also non-optical capture systems, not based on the use of cameras, but on other types of sensors. They mainly consist of electromagnetic systems, electromechanics systems and inertial systems. In recent years inertial sensor are increasingly being used for human gait analysis because of their characteristics are much improved as they are widely used in other fields.

Inertial Measurement Unit (IMU) is a device that measures angular velocity and orientation of the body on which it is placed, using the combination of triaxial accelerometer, gyroscope and sometimes magnetometer data. IMUs performance in terms of reliability and accuracy are improving as well as their dimension decreasing, allowing the system to be wearable. The development of inertial technology for the electronic marketplace, let these sensors to be less expensive from an economic and battery consumption point of view. Inertial sensors have the significant advantage of being able to be used outside a laboratory. Measurements in a free environment result more truthful because subjects are less influenced during trials and to be able to carry out tests in any space, has allowed development of movement analysis also in the sport field.

Gait analysis, besides body segments spatial position, considers other measurements to better describe human movements. Therefore, in gait analysis laboratories there are often dynamometric platforms that measure 3D ground reaction force. The “butterfly diagram” of this reaction force during the gait cycle, can be obtained and evaluated. Also resulting moment can be calculated in 3D components. During walking muscular forces and dynamic forces, determined by segments movement, are get involved and so measuring them it is possible to assess gait characteristics.

Evaluation of gait dynamic also utilizes the electromyography technique that measure muscle activity as electrical signals from appropriate electrodes, those could be placed on the skin (surface electrodes) or directly inserted into the muscle (needle electrodes). The activity of different muscles is assessed during deambulation and for each gait phase active and passive muscles can be determined. Evaluate muscular activity can be useful to detect pathologies or injurious gait strategics not observables with spatiotemporal parameters.

2.1 GAIT ANALYSIS WITH INERTIAL SENSORS

Most of the studies on movement analysis carried out so far utilize optoelectronic systems, but in recent years inertial sensing technology is expanding its potential in human movement analysis. One of principal advantage over optoelectronic system are that IMUs are independent of the specific environment. In fact, they allow data recording outside a laboratory, without the use of specific cameras positioned inside. Because inertial sensors are used in the consumer electronics market products their price and their power consumption keep dropping while miniaturization enhances, and their performance improves increasing reliability and accuracy.

Inertial sensor unit generally includes a triaxial accelerometer, gyroscope, and magnetometer whose complementary information is utilized to estimate the orientation of the sensor coordinate system (SCS) with respect to a global coordinate system (GCS). GCS refers to Earth fixed reference system that depend on the direction of gravity and Magnetic Nord. When sensor is attached to an object in motion, to measure its orientation over time, an alignment procedure need to be implemented to describe the relative orientation between the object coordinate system and the SCS. Regarding human limb motion analysis, SCS need to be referred to body segment coordinate system (BSC) on which IMU is fixed. Most simple procedure is a manually alignment of the case sensor with the longitudinal body segment sensor ^[2], but studies have been carried out to define this relative position more accurately.

One of major challenge using IMU technology is to implement an effective anatomical calibration procedure to refer information to BSC. A possible approach is to use the direction of gravity during known calibration postures (e.g., upright standing posture) to initialize the joint kinematics. Then, other studies include functional methods, the imposition of a joint constraints and the direct identification of anatomical landmark.

One of the main causes of error in inertial sensor measurement is due to soft tissue, that involves the presence of a relative motion between the sensor case and the bony segment below. So, soft tissue artifact (STA) describes error in measurement due to the relative motion between the sensor case and the bony segment. This unintended movement is because the sensor moves on the skin and because of the presence of the soft tissues. Sensors need to be firmly attached to the body segments during movement, to reduce as possible the translation on the skin surface. On the other hand, IMUs attachment should result comfortable so that subjects can act naturally movements.

The influence of STA in the joints kinematic analysis is greater in obese subjects due to the greater thickness of the layer between the sensor and the bone, that means a grater relative motion.

While there are a lot of studies about the procedure to treat STA using optical stereophotogrammetry systems, there are still many outstanding issues in using inertial systems. To reduce this type of error, we need to accurately estimate the position of joint center of rotation and inertial sensor orientation. To bring this purpose it is important both to develop algorithm and software that allow to compute accurate estimation and utilize reliable instrumentation and appropriate protocols for measurements. In the next paragraphs these aspects have been deepened in order to understand which could be a future research direction. All the studies proposed below related to the STA issue and presenting possible solution with regard to different prospects.

2.1.1. INERTIAL SENSORS ORIENTATION

While calculating IMU orientation, a downside is the accelerometer and gyroscope noise and the ferromagnetic disturbance that could undermine the estimation of sensor orientation. This error could be minimized by determining biomechanical constrains. Caruso et al. [3] propose a method to estimate the knee flexion-extension (FE) angle with the aim of minimizing the ferromagnetic disturbance that can cause discrepancies in the measurement of the orientation of the sensors on the shank and on the thigh to the GCS. IMUs have been mounted on the tibial plateau and on the lateral side of the thigh (*figure 3*). Considering the knee joint a pure hinge joint, allows to describe its kinematics as a rotation around the FE axes. The direction of this axes is assumed to be coincident with the one of the mean relative angular velocity vector. Exploiting the constraints that the FE axis must have the same orientation in the two GCSs, at each time step the two references system are realigned.

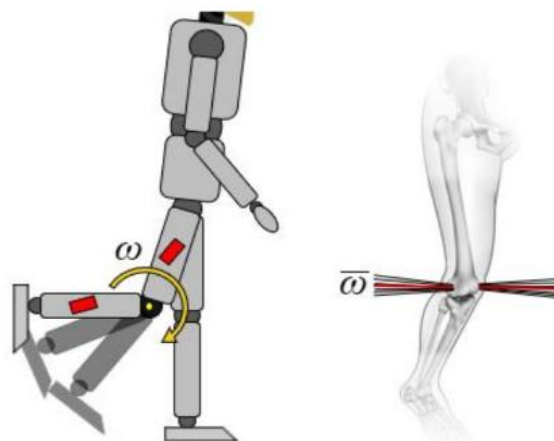


Figure 3 FE axis assumed to be coincident with the mean relative angular velocity vector [3]

One of the existing issues for inertial sensors to capture human motion is that they can only register orientation of the body segment, instead of spatial position. For this reason, often body skeleton dimension needs to be determined using other external measurement devices. A most adopted approach to measure limbs dimension is to consider a mathematical relationship between the body segment length and the stature, and to compute the relevant ratios. However, this manner results inaccurate because the physiological and pathological anthropometric variability. Despite for upper limbs, Crabolu et al. [4] proposed a method to in vivo estimation of a body segment length that defined the humerus length as the distance between the elbow and the shoulder FE axis. In the study one IMU was fixed on the wrist (figure 4). The study exploits the null acceleration point algorithm to estimate the shoulder center of rotation during shoulder sagittal elevation. One vector (vector r_s , figure 4) expresses the relative position between the shoulder center of rotation and the origin of the sensor coordinate system. In the same manner, a second vector (vector r_e , figure 4), obtained during elbow flexion-extension movement, represents the distance between elbow center of rotation and SCS origin. Humerus length is calculate as the modulus of the difference between the two vectors r_s and r_e . Validation of the method was conducted using measure computed from magnetic resonance imaging as the gold standard.

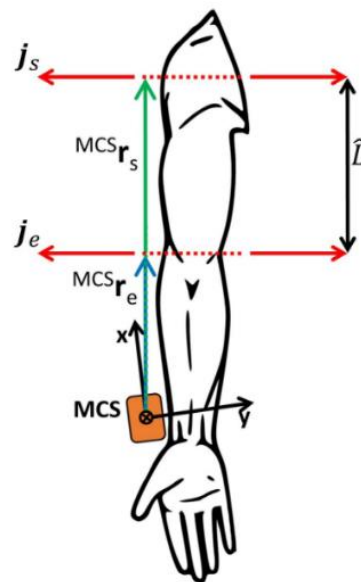


Figure 4 r_s and r_e with respect to the SCS during shoulder elevation in the sagittal plane and an elbow flexion-extension, and resulting humerus [4]

This thesis has been focused on the estimation of the knee angle and so the interest would be more on lower limb length estimation. The last proposed method lends itself to be used for thigh or shank length in vivo measurement. Nevertheless, it worth to mention a correlate study carried out by Yuan et al. [5] describing a skeleton calibration template-based method during which the lower limb dimension be estimated. It is a quick, free from asymmetric problem and self-contained calibration procedure that utilizes a template of foot positions, like which represented in *figure 5*. A set of posture of the person are measured with known relative position of feet on the template as that during measuring, when the subject matches the feet on the pre-designed footprints, relative positions are defined. Subsequently, with the measured orientation of limbs and the known end-effector postures, the skeleton dimension can be calibrated. To demonstrate the methods, in this study five IMU sensors were attached to the subject: one sensor was positioned central on the lower part of the back and for each leg one sensor was placed on the thigh and one on the shank, both on frontal side, to analyze lower limbs movement, and a footprint template was used to define the dimension of the thigh and the shank and the distance between the two hips.

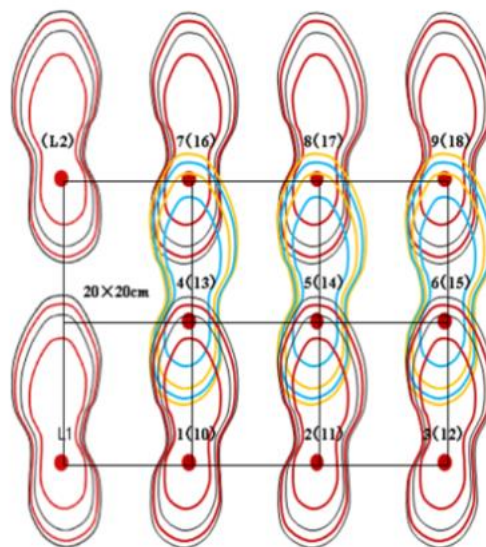


Figure 5 footprint template [5]

The last aspect related to IMU orientation is that IMUs do not directly measure position and orientation, but just acceleration or angular velocity data of body segments they are attached to. Then, an important challenge is to translate these data into a meaningful three-dimensional positional data, as the joint angles of the lower limbs during gait. Potentially inertial sensor position could be obtained integrating angular velocity data or double integrating acceleration data, but it resulted an inaccurate

measurement due to drift. Tadano et al. [6] proposed a method for three-dimensional gait analysis using wearable sensors. The method describes the gait posture as the product of initial posture and the subsequent angular displacement. As in most studies in the literature, the three coordinate systems (SCS, GCS, BCS) were defined and therefore a calibration procedure was proposed for establish the relation between SCS and GCS and between GCS and BCS. First, a static calibration was performed of standing upright and sitting with outstretched legs, to align sensors unit to the sagittal plane and minimize attachment errors due to misalignment of coordinate system (figure 6). From the two calibration postures gravity is measured (g_{stand} and g_{sit}). From their directions, axes for GCS are defined as Z axes being opposite direction of g_{stand} , Y axes the cross-product of g_{stand} and g_{sit} , and X axes the cross- product of Z and Y. In this way a rotation matrix R_{SG} that converts the three orthogonal axis of the SCS to the GCS was define.

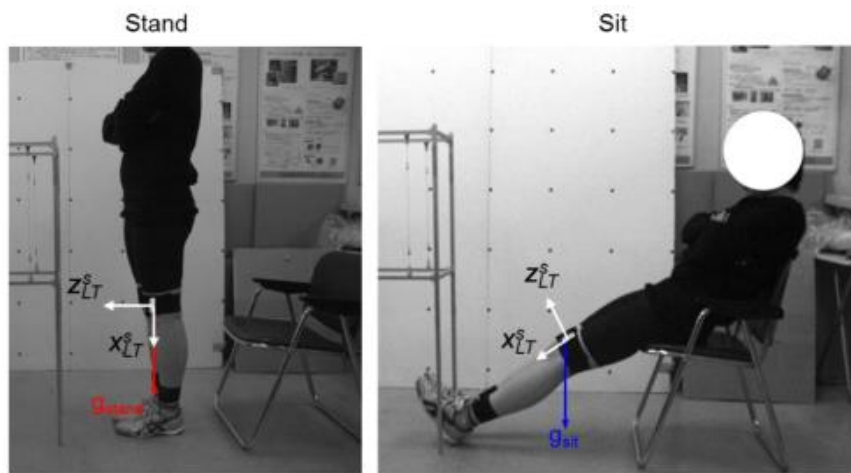


Figure 6 calibration positions [6]

Therefore, 18 reflective markers were attached to anatomical characteristics positions of the lower limbs, digital images were taken from the front and the side of the subject and from them another rotation matrix R_{GB} converting GCS to the BCS, was defined. Combining the two rotations, the rotation matrix to convert SCS to BCS was derived: $R_{SB} = R_{SG} \cdot R_{GB}$.

2.1.2. CENTRE OF ROTATION ESTIMATION

The localization of the joint centres is fundamental to define anatomical frames of bony segments used to human movement analysis. Determination of joint center position can be obtained via predictive method (e.g., Harrington Equations) or using marker-based functional methods (categorized as sphere-fitting or transformation approaches). [1] In the recent years methods to trace

the joint centres using inertial sensor have been developed, thanks to the increasing use of these for human movement measurement.

Crabolu et colleagues [7] investigate the influence of some parameters that could affect the accuracy of a functional method exploited to determine the center of rotation position. They made trials on a mechanical device that simulated a human spherical joint and the following experimental factors were assessed: (a) joint angular velocity, (b) type of joint motion, (c) amplitude of the angular range of motion (ROM), (d) distance between the IMU and the center of rotation, (e) model of the IMU. The evaluation, articulated on three levels, derived an analytical model of the error to facilitate the interpretation of the result. To reduce gyroscope bias, the value obtaining by averaging the first 4s of the static phase, was subtracted from each IMU records. Angular velocity rather was filtered before differentiation, using decimate wavelet denoising approach. The major considerations about center of rotation estimation, arose from Crabolu et al. work was that: joint angular velocity has a great impact on center of rotation calculation and specifically that slow joint movement produce more errors in measurements. Another significant result was relative to sensor position on the segment since it should be better attached close to the center of rotation. On the opposite, type of joint motion and angular ROM seem do not influence the CoR identification.

Limitations highlighted more currently in literature are the non-stationarity of the joint center and the presence of soft tissue artifact, that decrease the accuracy of the measurement in trials on human subject. by E. Frick and S. Rahmatalla developed a method to estimate joint center [8]. They assumed the STA as the combination of four transformation: translation, rotation, scaling, and shearing. Since the first two are considered the main determinants of kinematic accuracy and together constitute the rigid component of STA-induced motion, they proposed a model to represent STA by these two components. This model considers the STA rigid component by attaching a virtual sensor to the pendulum through a spring (simulate translation) and by applying a series of rotation matrix to data (simulate rotation). A scheme of the setup is shown in figure 7.

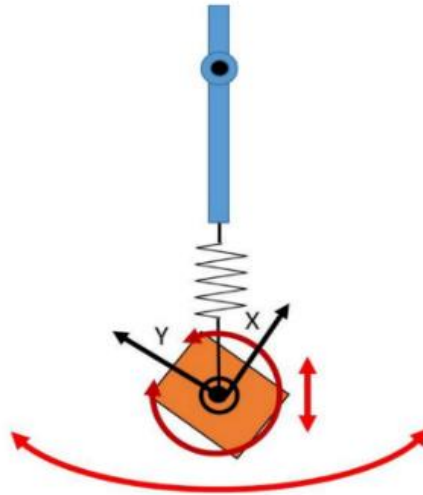


Figure 7 simulated pendulum simulate STA ^[8]

The methods to estimate the centre of rotation position, proposed in Frick and Rahmatalla study is based on the hypothesis that due to the impact of STA, the centre of rotation varies relative position in the articulation, at each frame of time. So, a joint centre vector has been defined as the time series of rigid-body realization calculated from Single Frame Optimization algorithm for each individual frame of data. The SFO algorithm aim is to quantify and mitigate STA error by improving calculation of joint kinematics. This approach allows to achieve a time-varying solution, highly correlated with the real condition. The simulation result indicates that rotation component impact more negatively the SFO accuracy.

The second part of Frick and Rahmatalla study ^[9] validated SFO physically recreating the simulation. A pendulum device (1 DoF) was employed to mimic human joint motion, while effects of STA were simulated by affixing the inertial sensor to the pendulum indirectly through a vacuum-sealed meet. A second sensor attached directly to the pendulum was also used for the experimental tests. The relative translation due to STA was then calculated by subtracting the location of the rigidly mounted IMU from that of the meat-mounted IMU. The rotation of the meat-mounted sensor relative to the rigidly mounted sensor was obtained by projecting the rotation matrix defying the orientation of the meat-mounted IMU to the GCS, into the coordinate system of the rigidly mounted IMU. The orientation of the rigidly mounted IMU's coordinate system was defined by the pendulum's orientation, meaning that any rotation still present after the projection was a result of the meat-mounted IMU moving relative to the pendulum.

2.1.3. SENSORS PLACEMENT

Finally, an important aspect to consider, to reduce STA effects, is the better placement for IMU on body segments. A. Forner-Cordero ^[10] et al. proposed a method for the validation of the attachment of skin-mounted sensors in presence of STA to characterize the frequency behaviour of the soft tissue between a bone and a skin-mounted sensor (*figure 8*). Behaviour of STA was characterized as a second order model representing the attachment on the skin and consisting of a spring of stiffness K , a dashpot with damping C and a mass M . These parameters are related to the physical properties of the attachment: the mass of the holder-accelerometer arrangement, while K and C are related to the mechanism properties of the skin and underlying soft tissue.

Three experimental steps were carried out. In the first one, different stimuli to excite the attachment were evaluated: manual displacement of the sensor, heel-drop (heels impact after free fall from standing on tiptoes) and gait. The heel drop was chosen for subsequent experiment because its lower variability. Then, in the second step heel-drop stimulus was applied under different attachment conditions: “unloaded” (sensor placed on the skin without adhesive tape or strapping bandage), “loaded” (elastic bandage firmly straps the sensor to the leg, compressing the skin without discomfort for the subject), or “load + mass” (bandage mass increased). The third part compared results against the model of the system sensor-skin.

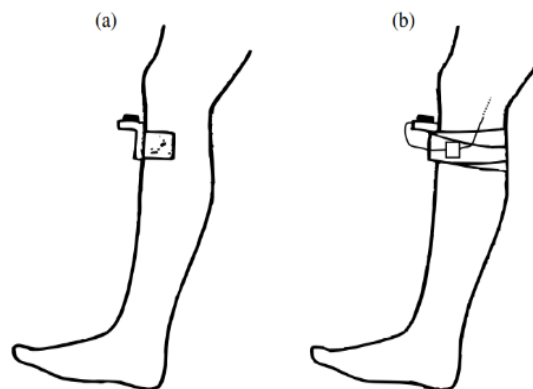


Figure 8 Schematic of the accelerometer attachment on the skin ^[10]

The experiment revealed that the damped and natural frequencies with the soft strapping were smaller than those with the hard one. Also arise a trend to increase the natural frequency of the system if the mass of the sensor was smaller. It is important that the natural frequency of the system be really distant from the frequency band of interest: frequency content of normal gait is considered to lie within a band between 4 and 6 Hz.

Another important aspect that deserves to be assessed is the optimal mounting position of inertial sensors to reduce STA. Y. Shimada work [11] focused on this aspect comparing knee angle data obtained from sensors mounted in different positions. IMUs were attached to the thigh and shank with elastic bands in three different patterns, described in *table 1* and represented in *figure 9*.

Table 1 IMUs attachment patterns [11]

Attached Position	Thigh	Shank
LATERAL	1	4
ANTERIOR	2	5
LATERAL AND ANTERIOR	3	6

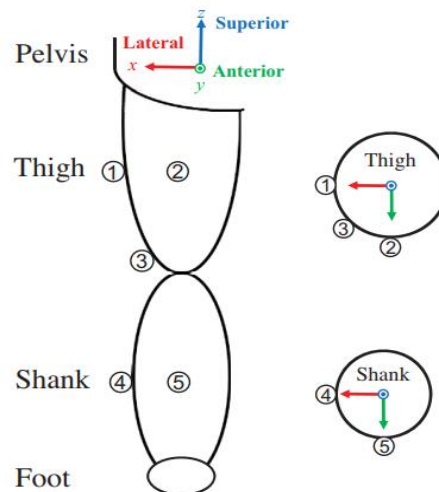


Figure 9 Schematic view of sensor positions [11]

Participants were instructed to do knee FE and knee flexion/valgus/external rotation. Lateral position results preferable than other two for motion measurement of the lower extremities. From the outcomes obtained it can also be derived that the significant error factor that affect angle estimation, is the mounting position and not the mounting direction.

Furthermore, also one of results obtained from F. Öhberg *et al.* [12] worth to be mentioned because they evaluated the precision and accuracy of adaptative filter used for studying different lower human body segments. Accuracy and precision for angular measurements of the shank were in general slightly worse than for pelvis and thigh. This could be since shank moves more than other segments during tests performed in that study. This observation could be taken into account when the positioning of the sensors is defined and could be used as an indication to understand what may be the major sources of error.

2.2. KALMAN FILTER AND POSSIBLE ALTERNATIVE METHODS

Wearable motion sensors are increasingly used for clinical applications in human motion analysis, but they present important limitation due to electromagnetic noise disturbances and oscillations those affect estimation of orientation and position. The accumulative integration errors, those arise from bias drift, can be handled with different adaptative filtering techniques. The most commonly used technique in recent years is Kalman Filter (KF) but there are many variations implemented from this or other solutions, also considered.

KALMAN FILTER

The Kalman filter was firstly published by Rudolf Kalman in 1960 and it is a technique for solving the linear quadratic Gaussian problem, estimating the instantaneous state of a system from its output, using linear transition function. It is an optimal estimator with respect to any quadratic function that estimates the error. Since it is optimal, it has remained relatively unchanged since it was first introduced but has received many extensions to apply it to more than just linear Gaussian systems. In fact, as described by Montella literature review ^[13], KF comes with some assumptions: (1) the state transition is linear, (2) the measurement is linear, and (3) the system is continuous.

The algorithm is structured in a predictor-corrector form: using the measurement of the system's observable quantities, the prediction of the state forward is corrected at each step. The error of the estimation is used to correct the state estimation. The gain K allows to weigh the error and to bring it inside of the model in order to correct the estimation of the state (*figure 10*). As outlined in the C. Montella study ^[13] the algorithm can be divided into two distinct phases:

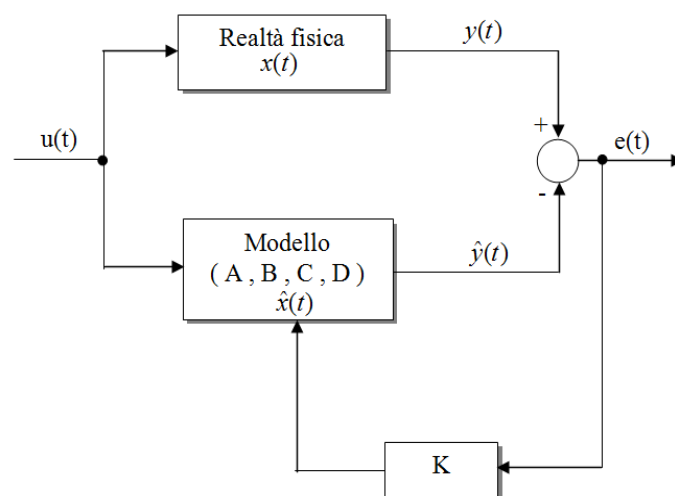


Figure 10 General scheme of Kalman algorithm functioning

- I. TIME UPDATE PHASE: the state, that is a Gaussian distribution, and his respective covariance are projected forward, in order to be updated:
- II. MEASUREMENT UPDATE PHASE: dependent variable (the observable one) is measured and fused with the prior distribution to estimate the posterior. Then the Kalman Gain is calculated based on covariance and Gaussian noise. The difference between the expected observation and the actual observation is known as *innovation*. The posterior distribution is then calculated from the combination of precedent equations that allows to correct the mean and covariance. These outputs are used as inputs to subsequent observation.

EXTENDED KALMAN FILTER

C. Montella in his literature review ^[13] compared Kalman filter with another version of the same filter, named Extended Kalman filter (EKF). It has been developed to extend the field of application of based Kalman algorithm and allow to widen the set of problem to which solve optimally. In fact, the KF can be used only with problems with linear measurement with added Gaussian noise.

EKF works through a process of linearization, where the nonlinear transition and observation functions are approximated by Taylor series expansion. The process update and the observation model are characterized by two potentially nonlinear functions:

$$\mathbf{s}_t = \mathbf{g}(\mathbf{s}_{t-1}, \mathbf{u}_t) \quad (5)$$

$$\hat{\mathbf{z}}_t = \mathbf{h}(\mathbf{s}_{t-1}) \quad (6)$$

Functions are approximated as a line tangent to the actual function at the mean value: the line is the first order approximation of the Taylor Series around the mean in which the nonlinear function is expanded. Equations of \mathbf{s}_t and $\hat{\mathbf{z}}_t$ are linearized taking the gradient of each with respect to the state \mathbf{s}_t , allowing therefore a predictor-correction form as original KF, with two phases:

- I. TIME UPDATE PHASE that propagates covariance forward as in KF but with a different relation
- II. MEASUREMENT UPDATE PHASE: mostly the same as in the original KF, EKF presents two crucial differences. First, the Gain is calculated using a Jacobian, making it that this can no longer be considered optimal. Second, the innovation is calculated differently since the observation model can be nonlinear.

How far from optimal the Gain will result depend on two aspect. The accuracy of the filter is influenced from how linear the transition and observation models are around the mean. Also, the modality of these two models is significative because if functions are multimodal, the filter can diverge.

Other than the FL and the EKF, several adaptive filters are proposed to advance the measurement techniques in human motion capture. For example, F. Öhberg et al. [12] in their study compared different filtering techniques used for sensor fusion of data from inertial sensors. Further, they evaluated how the precision and accuracy of adaptive filter could vary with different body segment of the lower limb: right and left thigh, right and left shank and pelvis were considered. Raw data came from sensors on these segments during functional tests performed by five subjects. Motion sensor data were calculated in the form of quaternions and the quaternion-based fusion of gyroscopic and accelerometric data was done using different filters: (1) normalized least mean square filter, (2) recursive least mean square filter, (3) quasi-static sensor fusion, (4) standardize Kalman filter and (5) modified Kalman filter. For all segment and test the modified KF and the quasi-static sensor fusion algorithm resulted most accurate solutions.

QUASI-STATIC SENSOR FUSION ALGORITHM

Quasi-static sensor fusion algorithm, implemented by Favre et al. [14], continuously monitors each sensor's activation to identify quasi-static events and to determine the change in angular output between two samples. Quasi-static events are defined by values of acceleration and angular velocity combined with some parameters empirically estimated from a previously collected gait recording. When a quasi-static event occurs, the algorithm adjusts the sensor fusion so that the quaternion is weighted in favour of the accelerometric-based orientation; otherwise, it favours the gyroscopic-based orientation. Algorithm performance improves by looking at the previous static event and making a linear regression between these two subsequence states to adjust the baseline between them.

MODIFIED KALMAN FILTER

Standard KF functioning is based on fusing orientation derived from accelerometric and gyroscopic data and modified KF uses the same model but in this case accelerometric-based orientation and gyroscopic-based orientation have different weight because they are calculated with different parameters. In addition, the measurement noise, monitored during each step, is used as a weighting factor to both standard and modified KF and it is defined on two levels. The weighted factor will be set in favour of one of them based on the quasi-static events, selecting the signal that most trustworthy. For the standard KF the choice was between one orientation based on gyroscopic-based orientation alone and one orientation based on a mix of gyroscopic-based and accelerometric-based. In contrast, orientation for the modified KF the choice was between a mix of gyroscopic-based and accelerometric-based with high accelerometer threshold and one with low accelerometer threshold.

MADGWICK FILTER

Another orientation filter applicable to IMU and MARG (Magnetic, Angular, Rate, Gravity) sensors is the Madgwick filter (MF) [15]. This filter performance exceeds the accuracy of base KF and presents the following advantages and innovative aspects:

1. Computationally inexpensive
2. Effective at low sampling rates thanks to an analytically derived and optimized gradient-descent algorithm
3. Contain one (IMU) or two (MARG) adjustable parameters defined by observable system characteristic.
4. On-line magnetic distortion compensation algorithm and bias drift compensation

Estimation of orientation of the sensor fusion frame relative to the earth frame is obtained through the fusion of the orientation calculations (in quaternion form) ${}^S_E q_{\omega,t}$ (from angular rate) and ${}^S_E q_{\nabla,t}$ (from vector observation). This filter employs a quaternion representation of orientation to describe the coupled nature of orientation in three-dimensions and is not subjected to the problematic singularities associated with a Euler angle representation. ${}^S_E q_{\omega,t}$ is calculated by integrating the quaternion derivate describing the rate of change of orientation of the GCS to SCS, obtained from the gyroscope measurement of the angular rate about x, y and z axis. Instead ${}^S_E q_{\nabla,t}$ is calculated using the gradient descent algorithm, an optimization method characterized by an initial condition ${}^S_E \hat{q}_0$ and a step size μ and by an objective function depending on the predefined reference direction of the field in the GCS ${}^E \hat{d}$ and on the measured direction of the field in the sensor frame.

The fusion of two type of orientation calculations depends on a parameter γ_t that defines weights applied to each orientation calculation. An optimal value of γ_t can be defined to ensure that the weighted divergence of ${}^S_E q_{\omega,t}$ is equal to the weighted convergence of ${}^S_E q_{\nabla,t}$. The magnitude of the filter gain that influences this weight parameter, need to be low enough that the divergence caused by magnetic and gravitational field observations is reduced to an acceptable level, but it has also a minimum value accepted dependent on gyroscope measurement error. The MF estimate the gyroscope measurement error as a gradient of error surface created by the magnetometer and accelerometer measurements, using an analytical derivation of the Jacobian and operating on a normalized gradient of the error surface. For this reason, this filter results low computational load and enables the formulation of an optimal filter gain based on system characteristics.

2.3. INERTIAL SENSOR IN CHILDREN MOVEMENT ANALYSIS

Although inertial sensor systems are becoming a widely used tool for gait analysis for clinical and research practice, in both healthy and pathological adult populations, there are still few data on the validity of these systems for use with children. Inertial sensor in addition to represent a useful alternative to optoelectronic systems being easy to apply and self-contained and allowing natural movement patterns analysis, also have increased possibilities in both paediatric and neurological population.

Gait requires complex neuromuscular coordination and walking is an emblematic part of development by allowing the child to explore and interact with the environment. Reference values from typically developing children and young adults are necessary to inform clinicians and researchers on typical gait maturation patterns, guide clinical practice and compare motor outcomes in children with gait abnormalities. S Voss and colleagues ^[16] tried to provide a normative database of spatiotemporal gait parameters in healthy children and young adults 5-30 years old. The parameters selected included: stride length, stride length variability, gait speed, cadence, stance and swing as percentage of gait cycle, double support time, foot strike angle, toe-off angle, toe-out angle, turn duration, peak turn velocity and number of steps to turn (*Table 2*). A database provides standard values, based on statistical population, to which researchers and clinicians can measurement obtained in their studies on pathological subjects.

The commercially available Mobility Lab Opal system (*figure 11*) has been used in Voss work. It consists in six sensors to place on the dorsal aspect of each foot and wrist, on the lumbar trunk at approximately L5, and approximately two centimetres below the sternal notch. Data recorded are collected by a laptop wireless and processed by Mobility Lab software containing the instrumented walk test; spatiotemporal parameters are then quantified with algorithm developed by manufacturer.

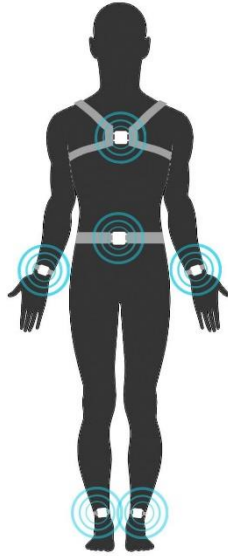


Figure 11 Mobility Lab sensors placement [16]

Evaluation of the data collected from the tests, was made by dividing the subjects by age, based on previous studies in the literature: 5-6, 7-8, 9-10, 11-13, 14-21, 22-30 years old. Participants were asked to perform the i-WALK test, that consists in two minute walk along a 25m walkway, in two directions. Test was performed under two conditions: at self-selected speed and walking as fast as possible. Descriptive statistics were therefore applied to all parameters. For the database determination, data were considered with absolute values and normalized to height. The study also analysed age specific changes in spatiotemporal gait and turning parameters. Results arise the increasing absolute stride length and gait speed and decreasing cadence, in both speed conditions, with advancing developmental age that is related to increasing stature. Indeed, stride length normalized to height do not vary between age groups in either condition. It is worth mentioning that all measures of foot position in children ages 7-8 demonstrated high standard deviation, possibly reflecting the maturation of the neural control mechanism for gait stability. In addition, results suggested that gait may not be mature until age 12.

Table 2 spatiotemporal gait parameters in healthy children and young adult database defined by S.Voss study [16]

Normative reference gait and turn data for the self-selected pace condition.

i-WALK domain parameters	5–6 (n = 22)	7–8 (n = 28)	9–10 (n = 21)	11–13 (n = 30)	14–21 (n = 25)	22–30 (n = 35)
Gait speed						
Stride length (m)	0.99 ± 0.11	1.10 ± 0.13	1.20 ± 0.13	1.32 ± 0.13	1.34 ± 0.16	1.42 ± 0.12
Stride length (% stature)	85.46 ± 9.38	85.37 ± 7.79	84.70 ± 8.73	83.53 ± 7.07	79.69 ± 7.97	81.56 ± 6.16
Gait speed (m/s)	1.11 ± 0.12	1.19 ± 0.16	1.25 ± 0.17	1.34 ± 0.14	1.28 ± 0.15	1.36 ± 0.17
Gait speed (% stature/s)	96.41 ± 10.13	92.70 ± 12.00	87.87 ± 11.68	85.23 ± 11.69	76.57 ± 9.62	78.34 ± 10.22
Gait variability						
Stride length CoV	0.14 ± 0.12	0.09 ± 0.05	0.05 ± 0.02	0.05 ± 0.02	0.04 ± 0.02	0.03 ± 0.01
Female	0.18 ± 0.15****	0.08 ± 0.04	0.05 ± 0.02	0.04 ± 0.02	0.05 ± 0.03	0.03 ± 0.02
Male	0.09 ± 0.05****	0.09 ± 0.07	0.04 ± 0.02	0.05 ± 0.02	0.04 ± 0.02	0.03 ± 0.01
Gait rhythm						
Cadence (steps/min)	138.95 ± 9.06	131.09 ± 11.79	124.20 ± 9.02	122.03 ± 10.94	115.35 ± 8.18	114.84 ± 9.78
Normalized cadence	120.65 ± 11.87	102.24 ± 14.23	87.54 ± 7.53	77.78 ± 11.91	69.29 ± 8.44	66.18 ± 8.40
Gait cycle phase						
Swing (%)	42.09 ± 1.82	41.32 ± 1.99	41.38 ± 1.59	42.19 ± 1.22	41.07 ± 1.64	41.21 ± 1.07
Stance (%)	57.91 ± 1.82	58.68 ± 1.99	58.62 ± 1.59	57.81 ± 1.22	58.93 ± 1.64	58.79 ± 1.07
Double support (%)	16.29 ± 3.61	17.57 ± 3.79	17.28 ± 3.11	15.67 ± 2.37	17.85 ± 3.29	17.58 ± 2.12
Movement transition						
Peak turn velocity (degrees/s)	275.86 ± 55.05	318.01 ± 77.25	308.33 ± 75.17	288.79 ± 47.94	235.68 ± 45.47	220.93 ± 44.76
Turn duration (s)	1.50 ± 0.37	1.50 ± 0.33	1.61 ± 0.25	1.61 ± 0.27	1.82 ± 0.33	1.93 ± 0.31
Number steps to turn	3.07 ± 0.82	2.93 ± 0.97	3.01 ± 0.57	2.99 ± 0.52	3.18 ± 0.64	3.38 ± 0.52
Foot position						
FSA (degrees)	–	35.88 ± 19.06	28.07 ± 4.61	26.82 ± 3.78	25.76 ± 4.83	25.96 ± 3.90
TOA (degrees)	–	33.43 ± 14.06	38.77 ± 2.86	38.92 ± 2.00	39.37 ± 3.24	39.43 ± 3.53
Toe out angle (degrees)	–	3.21 ± 8.73	4.60 ± 6.27	4.71 ± 4.52	5.83 ± 7.37	6.24 ± 5.28

Data presented as female and male only when statistically significant differences were observed between the sexes. Key: FSA, Foot strike angle; TOA, Toe off angle
****p < 0.0001.

Normative reference gait and turn data for the fast pace condition.

i-WALK domain parameters	5–6 (n = 20)	7–8 (n = 28)	9–10 (n = 22)	11–13 (n = 29)	14–21 (n = 24)	22–30 (n = 37)
Gait speed						
Stride length (m)	1.04 ± 0.09	1.17 ± 0.16	1.31 ± 0.13	1.45 ± 0.16	1.50 ± 0.18	1.61 ± 0.19
Female	1.08 ± 0.07	1.11 ± 0.16*	1.29 ± 0.15	1.45 ± 0.13	1.42 ± 0.14***	1.5 ± 0.18****
Male	0.97 ± 0.06	1.23 ± 0.15*	1.33 ± 0.11	1.45 ± 0.18	1.62 ± 0.16***	1.72 ± 0.12****
Stride length (% stature)	89.08 ± 10.45	90.88 ± 9.50	92.15 ± 8.88	91.20 ± 8.36	89.31 ± 8.37	92.58 ± 7.95
Gait speed (m/s)	1.26 ± 0.17	1.46 ± 0.14	1.59 ± 0.19	1.70 ± 0.16	1.65 ± 0.17	1.81 ± 0.22
Gait speed (% stature/s)	107.87 ± 14.17	114.30 ± 8.55	111.95 ± 13.08	106.85 ± 13.02	98.58 ± 10.35	103.84 ± 10.88
Gait variability						
Stride length CoV	0.19 ± 0.21	0.10 ± 0.08	0.07 ± 0.05	0.06 ± 0.05	0.04 ± 0.03	0.03 ± 0.01
Gait rhythm						
Cadence (steps/min)	147.62 ± 17.80	150.92 ± 9.97	148.04 ± 11.03	140.80 ± 13.23	132.73 ± 8.84	134.32 ± 9.34
Normalized cadence	126.52 ± 16.08	118.41 ± 13.22	104.17 ± 9.11	88.83 ± 13.73	79.49 ± 9.53	77.63 ± 8.61
Gait cycle phase						
Swing (%)	41.76 ± 3.58	42.63 ± 2.42	43.61 ± 1.48	44.48 ± 1.32	43.09 ± 1.84	43.59 ± 1.35
Stance (%)	58.24 ± 3.58	57.37 ± 2.42	56.39 ± 1.48	55.52 ± 1.32	56.91 ± 1.84	56.41 ± 1.35
Double support (%)	15.74 ± 5.47	15.34 ± 4.48	13.56 ± 2.16	11.45 ± 3.03	14.14 ± 3.31	13.27 ± 2.22
Movement transition						
Peak turn velocity	300.21 ± 58.07	360.45 ± 69.84	357.33 ± 72.57	341.14 ± 50.18	281.75 ± 45.34	277.63 ± 54.84
Turn duration (s)	1.55 ± 0.36	1.40 ± 0.20	1.39 ± 0.27	1.47 ± 0.23	1.65 ± 0.27	1.67 ± 0.25
Number steps to turn	3.07 ± 0.98	3.11 ± 0.60	3.03 ± 0.84	3.16 ± 0.60	3.40 ± 0.74	3.41 ± 0.64
Foot position						
FSA (degrees)	–	36.78 ± 19.94	28.91 ± 4.35	29.22 ± 2.98	28.89 ± 4.85	28.74 ± 3.83
TOA (degrees)	–	35.28 ± 15.18	40.67 ± 3.17	40.57 ± 1.85	41.71 ± 2.90	41.17 ± 3.94
Toe out angle (degrees)	–	6.21 ± 13.12	4.18 ± 6.73	4.22 ± 4.84	5.39 ± 6.66	4.49 ± 4.92

Data presented as female and male only when statistically significant differences were observed between the sexes. Key: FSA, Foot strike angle; TOA, Toe off angle
*p < 0.05 ***p < 0.001 ****p < 0.0001.

Take into account the different sizes and anatomical proportions in children is important when using adult-developed protocols and algorithms. Achieving functional gait and maximizing ambulatory independence are two of the most important functional outcomes for children suffering from musculoskeletal and neurological pathologies. It is crucial for clinicians to be able to analyse gait children to recognize and attempt to correct any impairments and sub-optimal movement patterns that may be limiting functional capacity. As demonstrated in the J. L. Lanovaz [17] study, neglecting the different anthropometric characteristics can lead to greater errors in the movement analysis of children.

J. L. Lanovaz et al. proposed to validate spatiotemporal data from the MobilityLab, system before mentioned, comparing it to a 3D motion capture system using Bland-Altman method. While temporal measurements were similar between the two systems, MobilityLab demonstrated a consistent bias with respect to measurement of the spatial data, whose error is due to difference in relative leg length and gait characteristic in children. In fact, indirect measurement such as spatiotemporal parameters, often rely on algorithms with assumptions and reference values based on adult data. To data collection, height was obtained using a stadiometer and leg length was estimated as a percentage of it and defined as the vertical distance between great trochanter and the ankle during standing. The four variables compared between the two systems are: stride time, stance time, stride length and stride velocity. While stride time and stance time were comparable between the two systems, stride length and stride velocity showed larger biases, attributable to error in leg length values that is a fixed percentage of total height based on published data for adults (49,1%). In children, leg length proportion is smaller: mean 42,7% in this study. MobilityLab collects angular motion data only from the shank and uses a prediction formula, also based on adult data, to estimate the thigh position. J. L. Lanovaz developed a stepwise linear regression to model stride length error that includes the independent variables shank range of motion, stride time and leg length. Error correction was added to the original stride length to generate the correct value.

As mentioned above, a crucial issue about IMU is the calibration procedure and the definition of the anatomical coordinate systems. In children gait analysis we need to consider, further to different anatomical proportions, also the less collaborative approach that is possible to aspect from children. In this regard, it is worth mentioning the Outwalk protocol, developed in A. G. Cutti work ^[18] to easily measure the thorax-pelvis and lower-limb 3D kinematics on children with cerebral palsy. This kinematic model assumes thorax, pelvis, thigh, shank and foot as rigid segments. Thorax-pelvis, hip and ankle joint are deemed as ball and socket, while knee is assumed as a “loose” double- hinge joint, with one rotation (flexion–extension) occurring about a mediolateral axis fixed in the distal femur and the other rotation (internal–external) occurring about a longitudinal axis fixed in the tibia.

To estimate the knee FE axis direction is the first step to define the anatomical coordinate systems of the thigh and shank segments. The orientation of the IMU over thigh and shank is measured during pure knee FE task. To allow the possibility to perform the test on a wider population, FE movement can be done autonomously standing in an upright posture by a patient able to do that, or passively with the subject lying in supine position while a therapist executes the knee FE movement.

To define the anatomical coordinate systems of body segments and to express their orientation in the corresponding SCSs, the orientation of these last are measured during a static trial. Also, two static posture were proposed:

1. upright position with the back straight, looking forward, knee centre aligned to the ASIS (anterior superior iliac spine) and the line from the 2nd metatarsal head to the calcaneus of the right foot parallel to the same line of the left foot (*figure 12*)
2. supine position with the back on a mat, the hip flexed h degrees and the knee flexed k degrees, the knee centre aligned with the ASIS and feet in neutral position and parallel to each other as in posture 1 (*figure 13*).



Figure 12 upright calibration posture

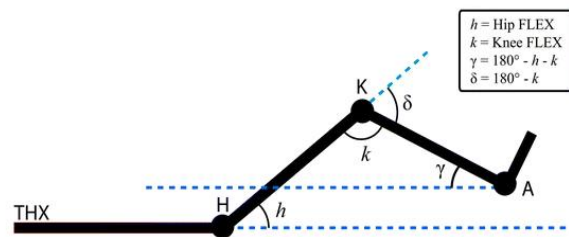


Figure 13 supine calibration posture

The Outwalk protocol takes about ten minutes to complete and does not need any specialized device other than the inertial sensors. The definition of the distal knee CS presents an advantage with respect to the CS recommended by the ISB. Indeed, the medio-lateral axis (Z) of the CS is defined along the mean FE axis of rotation of the knee, while in the ISB the femur Z axis is obtained as the last axis after the longitudinal and posterior axes are computed. This means that the medio-lateral axis of rotation of the knee in the ISB anatomical CS is not directly controlled, and its direction can be different from the inter-epicondylar axis.

2.4. OVERWEIGHT CHILDREN GAIT CHARACTERISTICS

Obesity is associated with numerous health problems such as hypertension, type 2 diabetes, but it is also associated with orthopaedic problems due to the overload on musculoskeletal structures. Being obese/overweight has been linked to various changes in musculoskeletal structures and mobility, those predispose subjects to greater soft tissue and skeletal injury with repetitive loading task and this may negatively affect their desire to engage in physical activities. Gait analysis on obese and overweight subjects and therefore the identification of its characteristics could allow clinicians to recognize other disease. Previous literature showed differences in spatiotemporal parameters similar to those in obese adults, with longer gait cycle and stance phase duration and a reduced cadence. Also, flatter foot pattern at heel contact was reported.

N. Pathare^[19] and colleagues work proposed a comparison between healthy weight, overweight or obese children to investigate difference in gait, balance, muscle strength and physical activities. Velocity, cadence, stride length, heel-to-heel base of support and stance cycle were measured during a walk performance with GAITRite portable single layer sensitive walkway system. Balance was assessed using the OLST (one leg stance test) in the eyes-open condition and handgrip strength was the method considered to evaluate the upper extremity strength. Children involved in this study were 5-9 years old, distributed in the three groups based on body mass index (BMI), calculated using the Center of Disease Control and Prevention's BMI Percentile Calculator for Child and Teen.

Experimental results arise a significant difference in heel-to-heel base of support distance showing greater values in overweight /obese children compared with health weight. It could be related to increased adipose tissue in the thigh and a need to increase postural stability. Regarding balance has been found that overweight/obese children were not able to maintain single limb stance as long as the healthy weight children. Authors report that impaired balance could be due to inadequate muscle function or caused by the altered joint torque needed to stabilize the body, over a reduced base of support. Whether impaired balance is due to inadequate muscle function or altered joint torque needed to stabilize the body over a reduced base of support is not known. Obese children had a higher grip strength than their counterparts, maybe because they develop more fat-free mass with increased adiposity that could help support extra load. On the contrary lower leg strength results greater in healthy weight children that present a significantly greater vertical jump height than overweight. (table 3)

Table 3 parameters measured by GAITRite system during a walk performance [19]

Velocity, cm/s		
HW	127.46 ± 20.56	.181
OW/obese	133.71 ± 15.98	
Cadence steps/min		
HW	143.5 ± 18.32	.271
OW/obese	138.94 ± 14.06	
Stride length (left), cm		
HW	107.59 ± 13.48	.006 ^{a,b}
OW/obese	116.37 ± 10.85	
Stride length (right), cm		
HW	107.27 ± 13.84	.007 ^{a,b}
OW/obese	115.88 ± 10.60	
Heel-to-heel base of support (left), cm		
HW	7.63 ± 2.24	.038 ^a
OW/obese	8.83 ± 2.31	
Heel-to-heel base of support (right), cm		
HW	7.49 ± 2.21	.033 ^a
OW/obese	8.70 ± 2.27	
Stance of cycle (left), %		
HW	57.79 ± 1.46	.246
OW/obese	58.21 ± 1.46	
Stance of cycle (right), %		
HW	57.86 ± 1.50	.225
OW/obese	58.29 ± 1.39	

Abbreviations: HW, healthy weight; OW, overweight.

^aSignificant difference between the two groups at $P < .05$.

^bHowever, when controlling for leg length, no significant differences were found in stride length on either side between the groups of healthy weight and overweight/obese.

From literature is clear that obese children move less and with greater difficulty than normal weight counterparts but expend comparable energy. Increased metabolic cost have been attributed to poor biomechanics leading to a worse performance, although flexibility and absolute muscle strength are comparable in overweight and health weight children. S. P. Shultz et al. study [20] assessed 3D lower extremity joint powers in two walking cadences. They calculated mechanical power at the hip, knee, and ankle, in sagittal, frontal and transverse planes during self-selected and fast walking speed (*figure 14*). Obese children require larger sagittal plane joint powers to control the trunk and prevent the collapse of the lower limb, while promoting locomotion through greater propulsion. They also required greater frontal plane joint powers at the hip and knee to control external adductor moments during weight acceptance and raise the pelvis quickly for adequate toe clearance. Greater mass and cadence create a gait cycle that requires more mechanical power. It has also been noticed that obese children had considerably greater differences between walking cadences than normal weight children. Increased muscular power to maintain to maintain a faster cadence may cause obese children to fatigue more quickly and have difficulty managing faster paced walking.

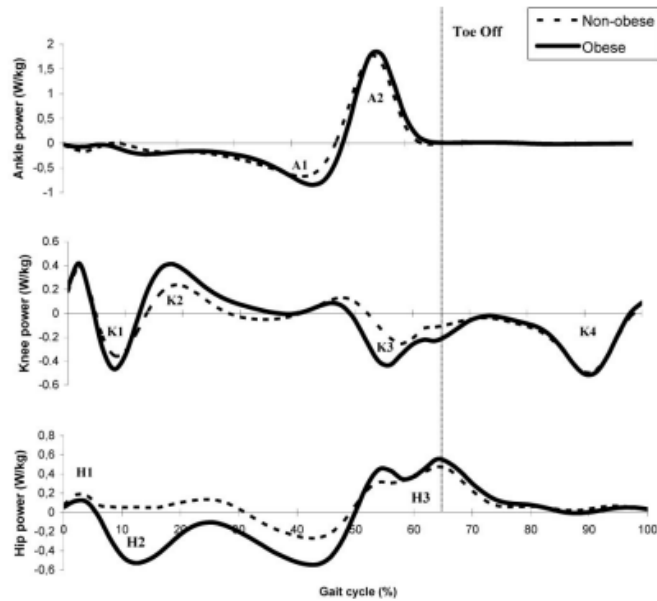


Figure 14 3D lower extremity joint powers in two walking cadences [20]

J. Nantel et al. [21] specifically studied the different gait strategy developed by obese children, analysing mechanical power spent during walk task. Their work had the aim to determine the impact of excessive body weight on gait parameter through the comparison of spatiotemporal, kinematic, and kinetic parameters in obese and non-obese children during self-spaced walking. Statistical analysis on kinematics parameters showed the single support phase duration shorter in the obese group compares with the normal-weight children group and consequently the double stance phase longer in the first.

Another important result from J. Nantel work is that obese children modified their hip motor patterns by shifting from extensor generation to flexor absorption earlier in gait cycle, compared with non-obese children. This led obese children to significantly decrease the mechanical work done by hip flexor because this early eccentric hip flexor contraction requires less energy than a concentric contraction. Mechanically, when a muscle absorbs energy by lengthening its muscle fibres, the energy can be transferred to the subsequent concentric (power generation) phase. To quantify the amount of energy transferred from the hip absorption to the hip generation phases, the ratio was used. Obese children are mechanically less efficient at transferring energy, since the mechanical work in hip generation was comparable in two groups, while the ratio was higher in obese children. Some energy maybe lost as heat, in the passive biological components, or transferred to another plane such as frontal plane. Another possibility is that this energy absorbed during the eccentric contraction could be used to control the larger trunk inertia that needs to be stabilized during walking.

It is worth noting another effective way to detecting gait anomalies in terms of symmetry, through study of trunk acceleration: the harmonic ratio, a parameter computed after processing trunk acceleration in frequency domain. Harmonic ratio is calculated for anteroposterior, vertical and mediolateral directions, quantifies step-by-step or stride-by-stride symmetry being higher values of harmonic ratio representative of greater symmetry. The V. Cimolin study [21] aimed to assess the applicability of harmonic ratio as a parameter useful in discriminating difference in gait associated with a lack or excess of body mass in cohort of healthy children and early adolescents. Participants to the experiment were 7-14 years old subject, those were divided in three groups: underweight, normal weight and overweight. The findings of V. Cimolin study indicated some interesting difference in harmonic ratio values of three groups, particularly in medio-lateral direction where underweight children present reduced symmetry, while overweight children exhibit highest values of harmonic ratio in the medio-lateral direction. This result may be correlated with the larger step width previously observed in obese subjects to increase stability. A non-linear relationship between harmonic ratio and BMI exists and is represented by a curve with a steeper gradient for BMI values 12-20 kg/m² and a plateau after for higher BMI (*figure 15*). Hence harmonic ratio could represent a useful complement to the conventional spatiotemporal parameters and could give a point of view on the gait focused on center of mass, instead of to lower limbs.

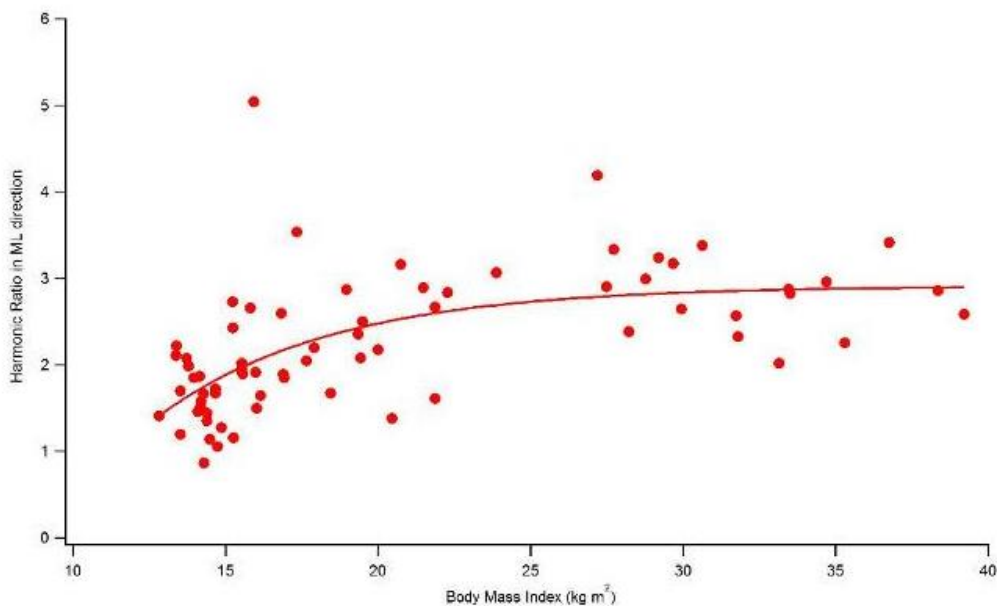


Figure 15 Trend of HR in the ML direction, with the BMI for all participants [21]

3. MATERIALS AND METHODS

3.1 MATERIALS

3.1.1. POLYCENTRIC KNEE JOINT MODEL

Knee joint is a really important articulation, that results essential for activities of human lower extremity, such as gait. It is formed by many different components such as menisci, cartilages, ligaments, and muscles allowing complex mechanical responses to different types of physiological loads. The study of human articulations movement requires, besides reliable motion capture techniques, body modelling that best represent structures and operations. [23]

In most of human motion analysis studies, body articulations are assumed as standard single hinge joints or monocentric spherical ones, characterized by just one axis of rotation or center of rotation. Therefore, most of the authors choose the model of lower limbs consisting of seven segments (pelvis, thighs, shanks, and feet), connected by six joints (hips, knees and ankles). However, this assumption, especially for the knee joint, represents an approximation. The human knee is comprised of three rigid bodies: femur, tibia and patella. It has been demonstrated that during joint motion patella remains in contact with the femur but rotates and translates with respect to the tibia. Interaction between these three rigid bodies makes modelling it more difficult with respect to others human joints. [23]

Even if physiologically the knee joint allows a flexion-extension, internal-external rotation, and abduction-adduction, in the literature only the flexion-extension movement is usually analysed since it has the greatest range of motion. Hence, the analysis of knee kinematics is reduced to the sagittal plane (1) as a rotation around FE axis estimated as the line passing through-out the medial and lateral epicondyles (predictive methods) or (2) as the relative motion between shank and thigh (functional methods).

In this work, the knee joint model that has been used also includes the effect of the roto-translation kinematics, considering two AoR: fixed axes of rotation (fAoR) and mobile axes of rotation (mAoR). As it is explained in the report of M. Galletto *et al.* [24] the model is composed by three elements connected with flat hinges. Each hinge is then rigidly coupled to a cogwheel, so as to realize a gear in the center of the middle element, constraining the entire movement of the three elements. Therefore, if the first element is fixed and the second one rotates of θ angle with respect to its orientation, the third element rotates of 2θ angle. The mechanism of the utilized prototype consists in

two equal hinges rigidly fixed on three rectangular beams. The whole thing is assembled into a dummy leg model, reproducing both a thigh and a shank (Figure 16)

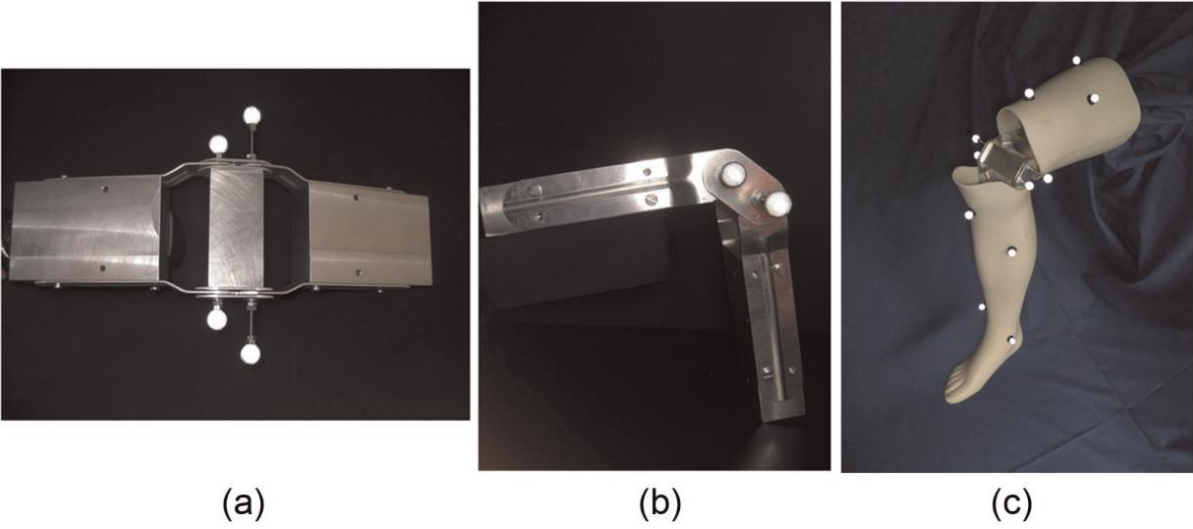


Figure 16 (a) frontal view of the polycentric hinge, (b) side view of the polycentric hinge, (c) dummy leg model based on the mechanical polycentric hinge. [24]

Considering this model during the FE movement where the shank moves relative to the thigh, if the shank rotates of $\Delta\theta$ with respect to the intermediate element, it rotates of $2\Delta\theta$ with respect to the thigh. (figure 17)

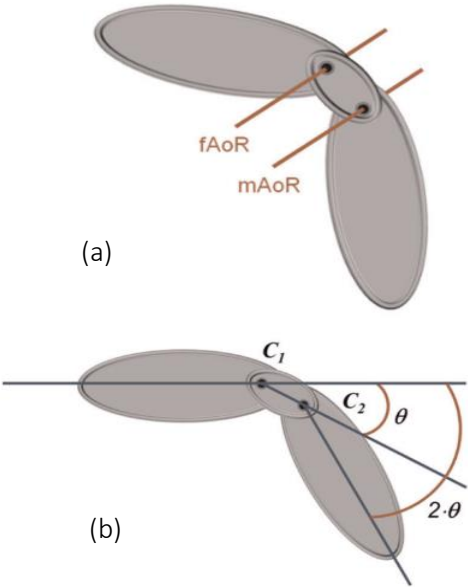


Figure 17 (a) polycentric hinge model, (b) polycentric hinge degree of freedom. [29]

3.1.2. XSENS MTx INERTIAL SENSORS

Xsens MTx is a complete miniature inertial measurement unit (*figure 18*) containing a tri-axial accelerometer, a tri-axial gyroscope, and a tri-axial magnetometer (Xsens, The Netherlands). Moreover, it includes an embedded processor that allows the sensor to accurately track 3DoF orientation as well as to provide kinematics data (3D acceleration, 3D rate of turn and 3D earth-magnetic field). [25]

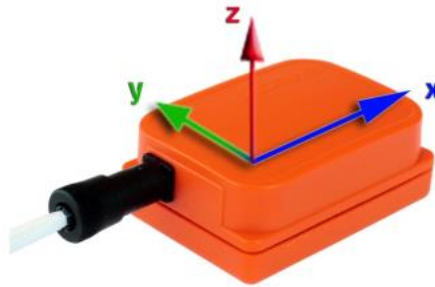


Figure 18 MTx case and SCS

The MTx casing is made of polyamide and it is designed to be as light weight as possible, and to be friendly for use on human body. The housing is dust resistant, but it is not waterproof. The case sensor has a total size about 38 x 53 x 21 mm (*Figure 19*). The origin of the MTx is defined by the physical location of the accelerometer. Although the MTx is primarily an orientation sensor, knowing the position of the true origin is important for application where accelerations are measured. It is reported the translation vector between the origin $O = [0, 0, 0]$ and a screw hole, chosen as reference point on the outside of the casing $O' = [4.5, 7.4, -9.5]$. [25]

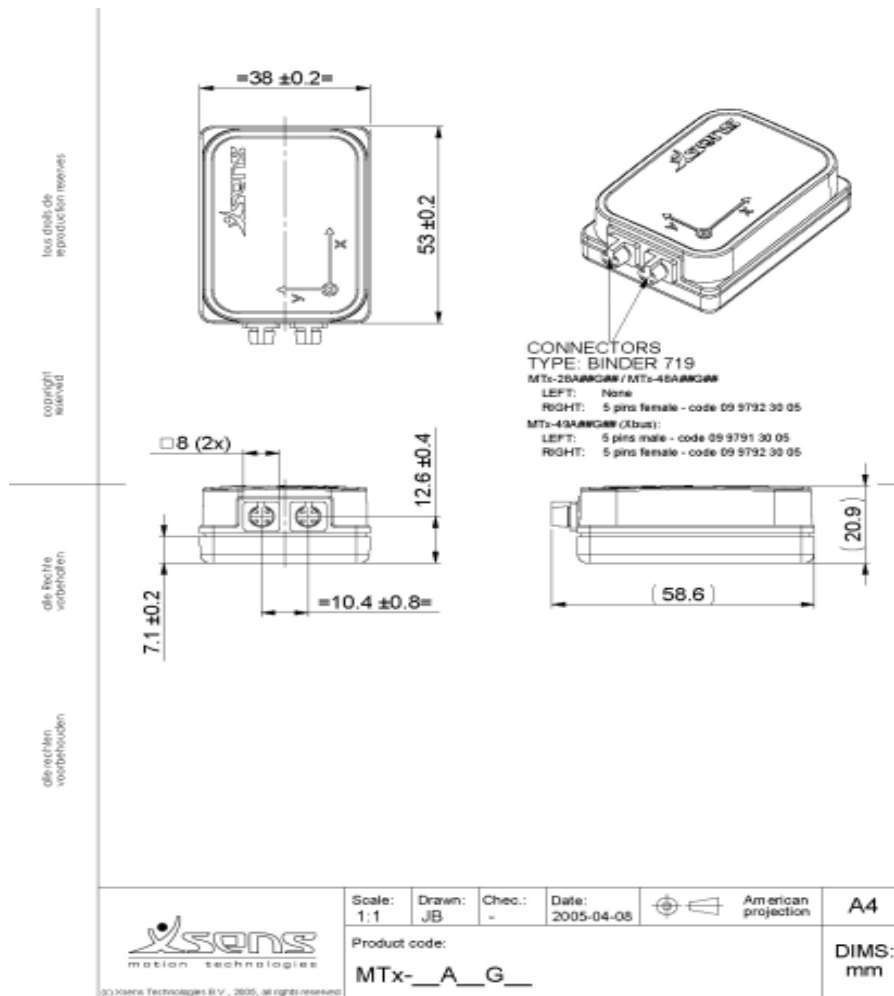


Figure 19 MTx dimensions

Table 4 summarizes the physical properties of the MTx. The average operating power consumption is 350mW ($\sim 70\text{mA} * 5\text{V}$) and the efficiency of the power input decrease with increasing the supply voltage. The small size and the light weight of each MTx contribute to providing an easy to wear and portable technology. Utilizing cable 1 m long, delivered with MTx Development Kit, is possible to chain sensors. One sensor is then connected with the Xbus Master, that allow communication with PC. However, communication between sensors and PC is also enabled through Bluetooth technology.

The MT Manager software for Windows XP/Vista is an interface that allows the user to (1) record data, (2) to view 3D orientation in real-time, (3) to export log files to ASCII, (4) to change and view various device settings and properties, and (5) to interactively “chat” with the MTx through a terminal emulator. [26]

After physically connecting one or more devices to the PC through USB connection or via Bluetooth, MT Manager configures them to start recording data. In order to use the acquired data in other programs such as Excel or MATLAB, MT Manager allows the user to export the data to a text file.

Table 4 MTx physical properties overview [25]

	MTx-28A##G##	MTx-48A##G##	MTx-49A##G##
Communication Interface:	Serial digital (RS-232)	Serial digital (RS-485)	Serial digital (RS-485, Xbus)
Additional Interfaces:	Syncln	-	Analog Input
Operating Voltage ²² :	4.5-30 V	4.5-30 V	4.5-30 V
Power consumption ²³ : (AHRS/3D orientation mode)	350 mW	350 mW	350 mW
Temperature Operating Range:	-20°C - 55°C	-20°C - 55°C	-20°C - 55°C
Specified performance Operating Range:	0°C - 55°C	0°C - 55°C	0°C - 55°C
Outline Dimensions:	38 x 53 x 21 mm (W x L x H)	38 x 53 x 21 mm (W x L x H)	38 x 53 x 21 mm (W x L x H)
Weight:	30 g	30 g	30 g

Inertial and magnetic data could be returned in output in both “calibrated mode” (only physical calibration model applied) and “un-calibrated mode” (which may be useful to analyse the source of the signal). The calibration of MTx is made according to a physical model of sensor response that correlates sampled digital voltage u to a respective physical quantity s , to obtain the *MT Test and Calibration Certificate* provided with the sensors. Calibrated sensor readings are expressed in the right-handed Cartesian Sensor Coordinate System (SCS), which is defined as fixed on the device, lined up to the external housing of the MTx (Figure 19). Alignment between the SCS and the bottom part of the plastic housing is guaranteed to $<3^\circ$. The non-orthogonality between the axis of the SCS is $<0.1^\circ$. [25]

The Global earth-fixed Coordinate System (GCS) is defined as a right-handed Cartesian system with X axis positive when pointing to the magnetic north, Y axis towards West direction, Z axis positive when pointing up. The MTx calculates the orientation of SCS with respect to GCS (Figure 20).

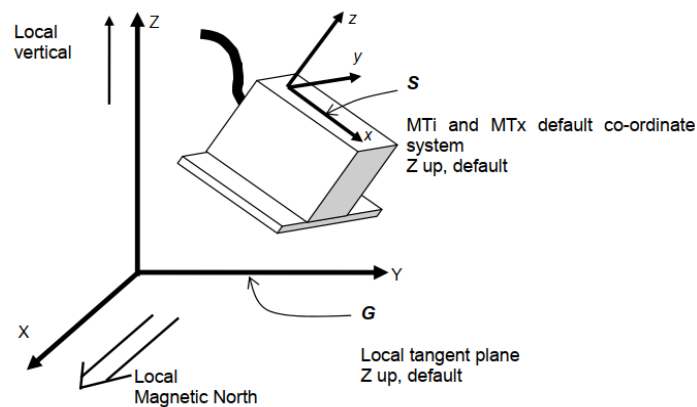


Figure 20 Default local earth-fixed reference co-ordinate system NWU (North-West-Up)

The output orientation can be presented in different parametrizations:

- (1) Unit Quaternion: it represents a rotation about a unit vector n through an angle α . The quaternion q_{GS} rotates a vector in the sensor co-ordinate system (S) to the global reference co-ordinate system (G)

$$q_{GS} = \left(\cos \frac{\alpha}{2}, n \cdot \sin \frac{\alpha}{2} \right) = (q_0, q_1, q_2, q_3) \quad (9)$$

- (2) Euler Angles: XYZ Earth fixed type angles (subsequent rotations around global X, Y and Z axis)

- φ (roll): rotation around X_G , defined from $[-\pi; \pi]$
- θ (pitch): rotation around Y_G , defined from $[-\pi/2; \pi/2]$
- ψ (yaw): rotation around Z_G , defined from $[-\pi; \pi]$

- (3) Rotation Matrix (or Direction Cosine Matrix): it is interpreted as the unit-vector components of the sensor coordinate system S expressed in G. For R_{GS} the unit vectors of S are found in the columns of the matrix.

The output definition in rotation output mode is:

$$\text{output data} = \quad a \quad b \quad c \quad d \quad e \quad f \quad g \quad h \quad i$$

where the rotation matrix is determined like:

$$R_{GS} = \begin{bmatrix} a & d & g \\ b & e & h \\ c & f & i \end{bmatrix} \quad (10)$$

The orientation of the MTx is computed by the Xsens Kalman Filter for 3 DoF orientation (XKF-3). The design of the XKF-3 algorithm can be explained as a sensor fusion algorithm where the measurement of gravity performed by 3D accelerometer and the measurement of the Earth magnetic north performed by the 3D magnetometer compensate for otherwise slowly, but unlimited, increasing errors from the integration of rate of turn data (angular velocity from the rate gyros). This type of drift compensation often characterizes Attitude and Heading Reference.

The accelerometer inside the MTx measures gravitational acceleration and acceleration due to the object movement with respect to its surroundings. Hence, it is used in XKF-3 to stabilize the attitude (roll and pitch) considering the assumption that on average the acceleration due to the movement is zero. The drawback of this hypothesis is that during this time the rate gyroscope must be able to track the orientation accurately, but rate gyroscopes used in MTx are able to track accurately the orientation for a short period, that is often shorter than that required for many applications.

The magnetometer inside the MTx measures the local (earth) magnetic field, which is used to stabilize the heading. XKF-3 is able to track possible disturbances, instead of incorrectly ignoring them. In addition, in case of structural magnetic disturbances, the computed heading will slowly converge to a solution using a “new local magnetic north”. However, heading does not directly affect the inclination estimation.

XKF-3 makes use of different “scenarios” to consider the appropriate assumption since characteristics of the acceleration and magnetic field change for different applications. Scenarios are divided in “human”, “machine”, and “marine” types of motion. In human gait analysis the “human” scenario is adopted for slow movements typical for an indoor environmental, and “human_large_accel” scenario for faster movements.

3.1.3. SILICON IMPLANTS

In order to understand how soft tissue artifacts could be reduced during gait sessions recording, specifically in obese subjects, it is necessary to simulate the soft tissue using a material with similar mechanical characteristics. “Soft tissue” is a collective term for all non-bony tissues, those ones have not been hardened by process of ossification pre calcification. They connect, surround, or support internal organs and bones, and include muscles, tendons, ligaments, fat, fibrous tissue, skin, lymph and blood vessels, fasciae, and synovial membranes. In this work, the interest was firstly oriented to reproduce the behaviour of the fat tissue, that is the component that mostly diversifies overweight and normal weight subjects. [27]

The study of J. L. Sparks et al. [28] evaluated the ability of silicone materials to mimic the distribution of stress in muscle tissue under concentrated loading. The longterm goal of the work was the development of a simulator that mimics the biomechanical conditions of stress and strain in deep muscle. The paper focused on (1) shear modulus, a mechanical property indicative of how stiff a material feels to the touch, and (2) the ability of a material to mimic the nonuniform stress distribution in tissues subjected to indentation type loading, such as that which occurs in muscle compressed by a bony prominence. Authors have considered silicone rubber to mimic soft tissues behaviour because of its ability to retain its shape, its resistance to the degradation and because it can be obtained in different degrees of stiffness to mimic its mechanical properties.

Three silicone formulations were considered: Ecoflex 0030, Ecoflex 0010, and Dragon Skin (Smooth-On, Inc, Easton, Pennsylvania). Unconfined compression experiments were conducted on them to quantify the mechanical properties of candidate silicone materials and compare them with

published values for biological tissues (*table 5*). All three formulations demonstrated shear moduli suitable with biological tissue. On Ecoflex 0030 was also carried out a test to investigate the ability to mimic the nonuniform stress distribution muscle, demonstrated under concentrated leg. Silicone performance was compared with porcine muscle one, observing similar nonuniform stress distribution patterns.

Based on the results of the material characterization experiments (*Tables 4 and 5*), a Patient Simulator Prototype was defined using silicone materials tested to simulate soft tissues: Dragon Skin was used as muscle, Ecoflex 0010 as fat, and Ecoflex 0030 as skin. One limitation that this simulator presents is the fact that the interfaces between the tissue layers (skin-fat, fat-muscle, muscle-bone interfaces) require further development to reflect anatomical structure. The model ultimately must be validated against biologic tissue representing all tissue components covering a bony prominence. However, qualitatively silicone-based tissue analogues are able to mimic the basic trend of a stress concentration developing in the material in the region of a bony prominence, when subjected to compressive loading, but they were not able to mimic all the complex features of biological tissue biomechanics, because of their significantly different structure and composition.

LITERATURE RANGES FOR SHEAR MODULI OF BIOLOGICAL TISSUES: ALL DATA REPORTED FROM COMPRESSION TESTING		
Biological Tissue		G (kPa)
Muscle	Longitudinal	51–105 ^{23–25}
	Transverse	11–54 ^{23,25}
	Active	17.1–30.5 ^{22,25}
	Relaxed	4.6–23.8 ^{6,15,16,22}
Skin		2.8–31.9 ^{6,20,26}
Fat		1.9–31.9 ^{6,20,26}

Table 5 literature ranges for shear moduli of biological tissues. data from compression testing [27]

BEST-FIT HYPERELASTIC MATERIAL CONSTANTS FOR SILICONE RUBBER FORMULATIONS			
Silicone Type	Ogden Model Terms		
	Shear Modulus G (kPa)	Strain Hardening Exponent α	Poisson Ratio ν
Dragon Skin	75.449	5.836	0.4999
Ecoflex 0010	12.605	4.32	0.4999
Ecoflex 0030	22.081	0.825	0.4999

Table 5 best-fit hyperelastic material constants for silicone rubber formulations [27]

In patent Trotta 2019 [28] is presented a concrete example of human tissues simulator that could be considered. The described patient simulator was developed to provide a non-human interactive format for teaching and learning techniques, with a system providing a realistic tactile feedback, on which medical personnel and medical student could train and get familiarity with needle, scalpel, and suture techniques. The patient simulator represented in *figure 21* includes a torso, legs, arms, and a head. We could put the attention to the thigh tissue insert because is where sensors will be positioned in tests carried out in this thesis work (*figure 22*).

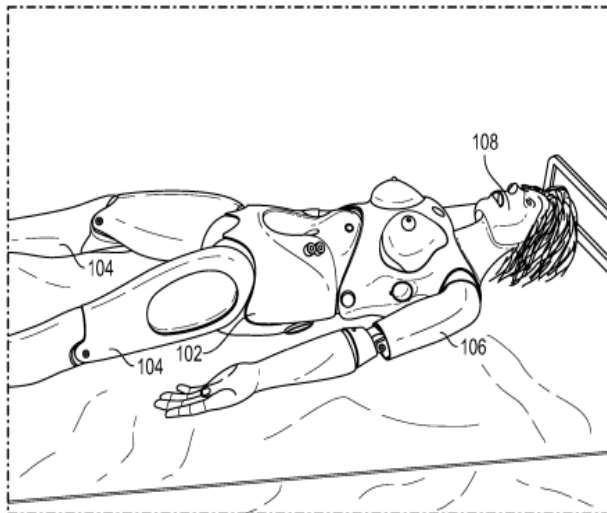


Figure 21 patient simulator No US 10438510B2 [28]

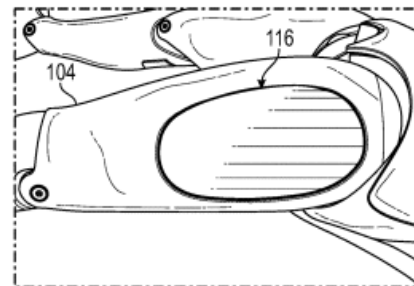


Figure 22 portion of the patient simulator illustrating a thigh tissue insert [28]

All the tissue inserts of the simulator have a similar layered structure, but relative thicknesses of the layers and the size and shape of the insert are adjusted to properly simulate the desired anatomical feature. The layered structure consists of four or five layers, formed from material having appropriate mechanical properties:

- **skin layer** (134 in *figure 23*): the surface layer, manufactured blending materials with a higher shore hardness with materials with a lower shore hardness, to mimic skin characteristics
- **subcutaneous layer** (138 in *figure 23*): intermediate layer manufactured from a blend of silicone types
- **fascia layer** (140 in *figure 23*): dense layer of connective tissue that is resistant to unidirectional tension forces and surrounds muscles, organs, and other soft structures. In some instances, Tyvek is utilized to form the fascia as it responds in a manner similar to the fascia when punctured, cut and/or sutured.
- **muscle layer** (142 in *figure 23*): layer with greater resistance compared with skin and subcutaneous ones.
- **backing layer**: layer that should encapsulate the muscle, fascia, and subcutaneous layers while providing a surface that sits within the insert's recess in the manikin.

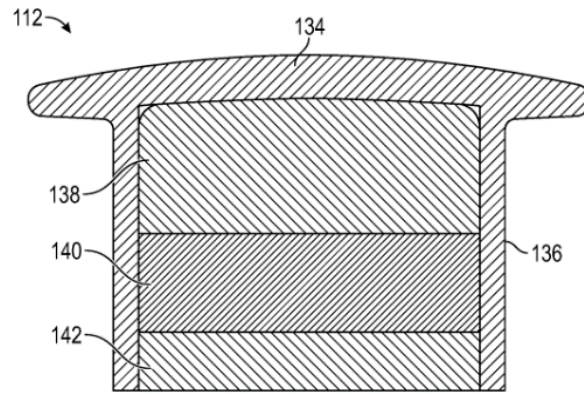


Figure 23 tissue insert layered structure [28]

It could be also considered some studies that describe methods to evaluate human tissues characteristics in order to apply it to define tissues properties in obese subject and then adjust patient simulators designed since normal weight subjects. F. Frauziols et al. [29] proposed a non-invasive method to identify in vivo the passive mechanical properties of deep soft tissues in the human leg. Taking into account the non-linear behaviour of these tissues, the study considered the leg soft tissue composed of different compartments:

- the compartment composed of adipose tissue and skin, which, in this study, is referred to as superficial soft tissues,
- the Fascia cruris, which is a collagenous membrane separating both compartments,
- the compartment of soft tissues surrounded by the fascia cruris, mainly composed of muscular tissue, which, in this study, is referred to as deep soft tissue compartment.

The method proposed combined an axisymmetric multilayer (i.e., skin, adipose tissue) finite element model with an indentation experiment to identify the mechanical properties of each forearm soft tissue. Finite element models of the leg in a relaxed initial state and a compressed state with stocking were compared to MRI scans of the legs in the same two states. The finite element model was composed of two compartments of soft tissues, allowing a distinction between the mechanical properties of adipose tissue and muscular tissue. (figures 24)

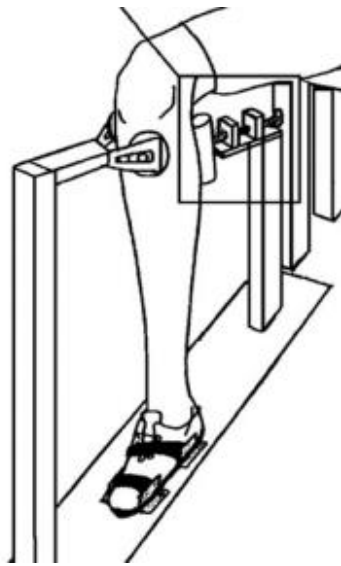


Figure 24 A) indentation experiment on the leg [29]

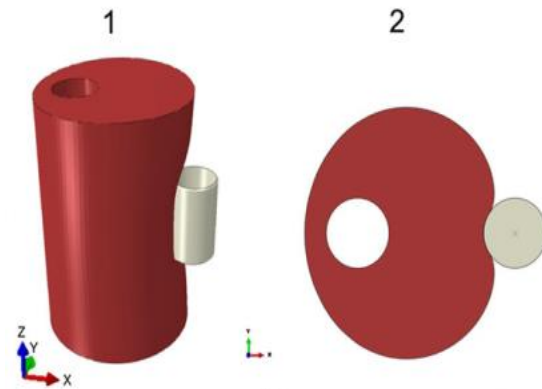


Figure 21 B) 3D simulation and plain strain simulation on 3D leg finite element model [29]

In R. Cuccaro et al. [30] study, a detailed description of the experimental apparatuses for the sound speed and the attenuation coefficient measurements is given. Tissue-mimicking phantoms play a crucial role in medical ultrasound research because they can simulate biological soft tissues. In last years, many types of polymeric tissues have been proposed and characterized from an acoustical and a thermal point of view. In this work, considering the necessity to develop laboratory standards for the measurement of ultrasonic exposure and dose quantities, the attention is focused on the uncertainty evaluation both result and analysis algorithms. Furthermore, the realisation of multi-components phantoms, Agar and Phytigel based tissue-mimicking gels along with others long chain molecules (dextrane or polyvinyl alcohol) and scattering materials (silicon carbide and kieselguhr) are investigated.

This paper reported accurate speed of sound and attenuation coefficient measurements. Speed of sound is measured by a pulse-echo technique in far-field condition, using an optical glass buffer rod; while attenuation coefficient is determined by an insertion technique, using demineralized water as reference material. To identify the material parameters of both constitutive models an inverse method was implemented: (a) Extraction of force-displacement curves from the bi-dimensional model, (b) Definition of a cost function quantifying the mismatch between numerical and experimental force-displacement curves, (c) Minimization of the cost function with the genetic algorithm implemented in Matlab®.

Kevin M. Moerman et al. [31] assess the use of Digital image correlation (DIC) in combination with finite element modelling to determine the bulk material properties of human soft tissue. A two camera DIC setup was then used to record the 3D surface deformation. The experiment was simulated using a finite element model. Two camera DIC configuration combined with FE modelling to determine the bulk

mechanical properties of materials leads to represent it using hyperelastic Neo-Hookean constitutive laws. To verify this method, indentation tests were performed on a silicone gel phantom.

The soft tissue phantom was moulded in a cylindrical polypropylene container and black paint speckles (0.22 mm) were applied to the top surface of the gel. A circular indenter was then used to apply compression up to 11,7 N (*figure 25*). The deformation of the top surface of the gel and the indenter displacement was then calculated by a software analysis. To simulate the compression, an axisymmetric finite element model of the gel indentation was created. The material parameters were iteratively altered until a good match with both the experimental indenter force and deformation was obtained.

Overall, from this study results raised that when the correct bulk material properties are applied, the finite element model has a good capability of reproducing the experimental boundary conditions.

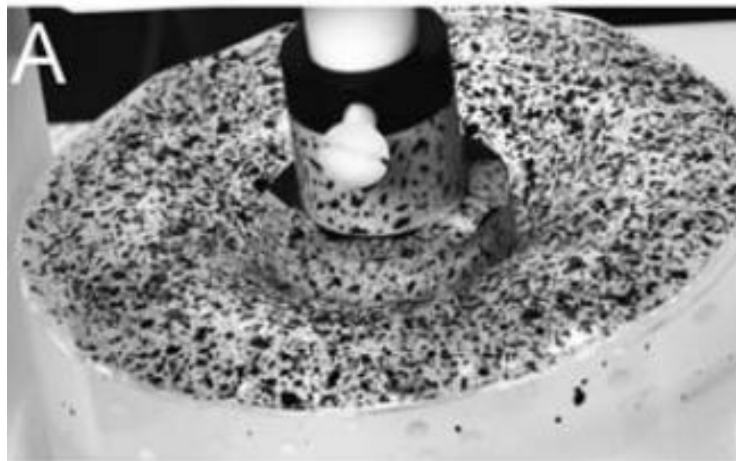


Figure 22 silicone gel phantom model and piston [31]

Biological soft tissues are not easy characterizable because exhibit a strongly nonlinear viscoelastic behaviour. So, it is often necessary to study them from different points of view to get a complete information. As a solution The S. Nicolle et al. study [32] aimed to develop a new constitutive law capable of predicting our experimental data in both linear and nonlinear viscoelastic regime with as few parameters as possible. The authors worked in particular to report additional material properties of kidney and liver tissues in oscillatory shear and constant shear rate tests. Considering soft tissues as a single-phase continuum, many attempts have been made to theoretically depict their gross material response. The linear behaviour at small strain is usually fitted with a generalised Maxwell or Kelvin model to account for the time dependence of their properties. Few models based on the fractional calculus were suggested for describing the linear viscoelastic response of biological soft tissues.

After considering literature, it was decided to create one-layer implants in silicone material. Some of silicone materials utilized in mentioned studies, were compared to manufacture implants to be used in our tests. *Table 6* shows mechanical parameters values of biological tissue and silicone materials, according to literature studies.

Table 6 silicone material mechanical characteristics

	SHEAR MODULUS (kPa)	STRAIN HARDENIN G INDEX	POISSON RATIO	YOUNG MODULUS (kPa)	DENSITY (g/cc)	TENSILE STRENGTH (Mpa)	ELONGATION (AT BREAK) %	VISCOSITY (cps)
MUSCLE	51-105 [21]		0.43 [28]*	32.15 [28]	1.0599			
SKIN	2.8-31.9 [21]	2.61-4.72 [26]*	0.46 [28]*	47.75 [28]		1-20 [27]	30-70 [27]	0.3-6.5 [26]*
FAT	1.9-31.9 [21]	(")	0.44 [28]	16.36 [28]*	0.9094			(")
DRAGON SKIN	75.449 [21]	5.836 [21]	0.4999 [21]		1,073	3,28	1000	23
ECOFLEX 0010	72.605 [21]	4.32 [21]	0.4999 [21]		1,041	0,83	800	14
ECOFLEX 0030	22.081 [21]	0.825 [21]	0.4999 [21]		1,065	1,38	900	3
TC 5005 C					1,09	3,27	550	15,25
Soma Foama					0,24-0,4			10

* referred to soft tissue (liver&kidney)

**Averaged values gathered from multiple sources on the web

Considering which materials had more similar characteristics with soft tissues, both ECOFLEX 0030 (Smooth -On, Inc., Easton, Pa) and ECOFLEX 0010 (Smooth -On, Inc., Easton, Pa) [34] were fitted to the use. However, taking into account that density values of two silicones were almost equal, ECOFLEX 0030 was finally chosen.

Therefore, two silicone implants have been manufactured (*figure 26*) to be used as soft tissue simulators. ECOFLEX 0030 is a platinum-catalysed silicone whose two components *Part A* and *Part B* are mixed 1A:1B weight or volume. To prepare implants the procedure indicated by the producer has been followed:

- 1) Pre-mix part B
- 2) Dispense amounts of parts A and B into mixing container
- 3) Amalgamate the mixture for 3 minutes paying attention on scrapping the sides and the bottom of the mixing container several times
- 4) Let silicone implants to cure at room temperature (18°C-23°C) for at least 24 hours

5) Remove the silicone implants from the moulds.

Two different moulds were used to manufacture implants used in this work. The smallest implant (diameter 9cm, thickness 2,5cm) was used to simulate soft tissue on the shank (*Figure 26-1*), while the other one (diameter 9,5-10,5cm, thickness 3,5cm) was used on the thigh (*Figure 26-2*), where soft tissues are greater.

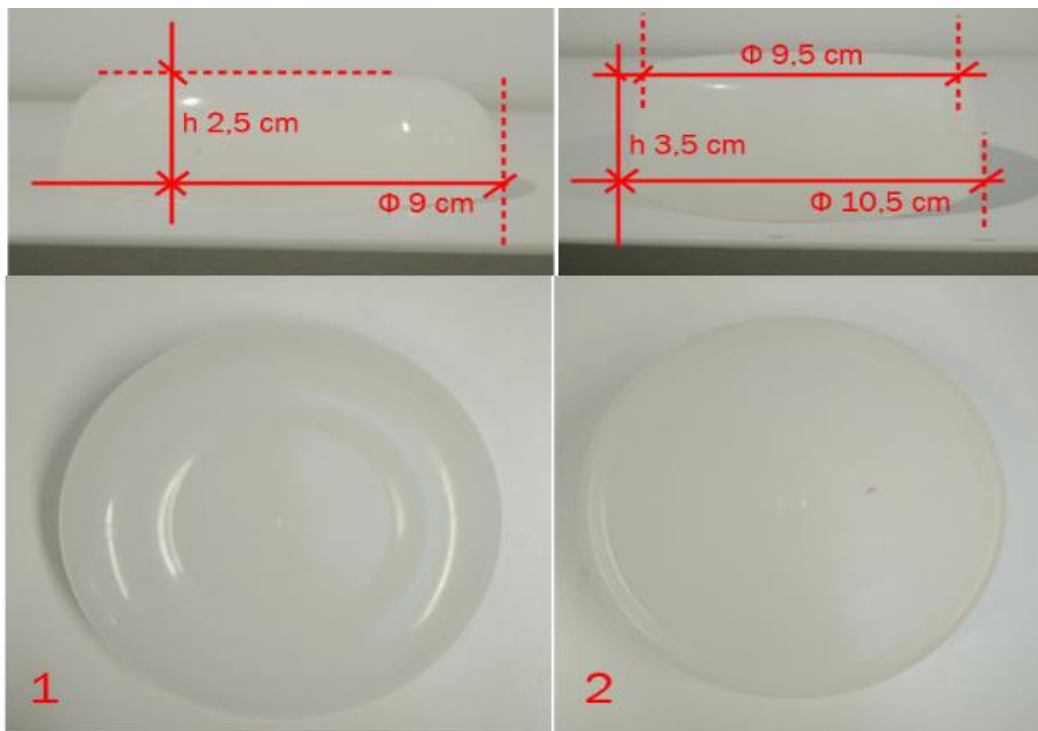


Figure 23 ECOFLEX 0030 implants

3.1.4. KINOVEA SOFTWARE

Kinovea is an open-source software designed and developed to perform video analysis, especially in the sport field. In addition to 3D optoelectronic systems, which are the gold standard for motion analysis, 2D analysis with traditional videos can be a good compromise, especially when the performance cannot be carried out in a laboratory, as some sportive tasks. Kinovea allows to perform 2D analysis of the movement, therefore it is necessary to place camera utilized as far as possible perpendicular to the plane of motion considered. Most of the video formats available on the market are compatible with the software, files from compact cameras, smartphones, tablets, and professional video cameras. ^[35] In *figure 27* is reported Kinovea interface.

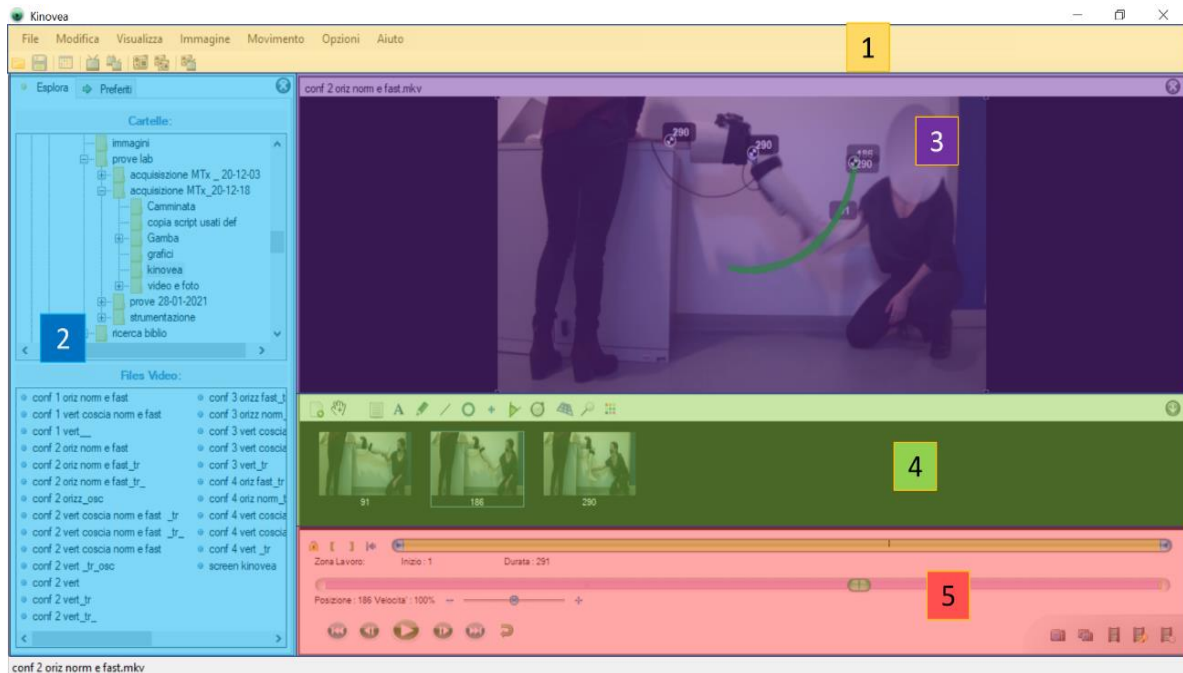


Figure 24 Kinovea workspace. 1: principal menu', 2: file explorer area, 3:video area, 4: key image control area, 5: play control area. [35]

Kinovea is organized around four core missions related to studying human motion:

- **OBSERVATION:** it is possible to slow down time for high-speed movement analysis or performs images transformation like “rotate”, “zoom”, “mirror”, “deinterlace”, “fix aspect ratio”. In addition, videos with heterogeneous framerates can be synchronized and also overlaid on top of each other. Time in Kinovea can be represented in various units like the frame number, the total milliseconds since start, or a classic timecode format.
- **ANNOTATION:** key images of interest can be created with also text comment attaches to them. Basic annotation (labels, numbers, lines, markers, etc) or annotation drawings can be copied and pasted around the frames videos and can also be painted permanently on the video frames. It is also possible let to draw attention to something using the spotlight or magnifier tools. Annotations are saved to KVA files (XML); they are vector based and can be modified at any time. The KVA file associated with a video is automatically reloaded. Other export options allow to save the individual frames or key images to separate files, create video slideshows and create videos with pauses on key images.
- **MEASUREMENTS:** Kinovea measures time spans using the chronometer and distance and angles using the line, angle and goniometer tools. Even if the plane motion is not aligned with the camera, using a grid-based calibration lets perform measurement. The program is also able to track single point trajectory or track the evolution of a multi-point object. Then, linear

kinematics based on trajectories of points or multi-point object can be obtained, as well as angular kinematics for angle tools and custom tools containing angles.

- CAPTURE: the main interface to capture and record camera streams can be configured for a single camera, two cameras or one camera and one playback screen. Image rotation is supported in the capture module and allow more flexible options in camera placement and orientation. Annotation tools can be used to create alignment guides and get posture feedback. When recording, these guides will be saved in a separate file and reloaded when playing the camera performance: save the camera frames in real time, with corresponding video. Various recording approaches can be used depending on use-case and delay, or in a batch operation at the end of the recording period. [35]

3.2. METHODS

3.2.1. PRELIMINARY TESTS PROTOCOL

Preliminary laboratory tests were carried out using the polycentric knee model and the silicone implants fixed under sensors. Four different sensors configurations were considered to evaluate sensors position influence on measurement. The aim of the preliminary tests was to identify the best inertial sensors setup in calculating knee flex-extension angle. Preliminary tests were also intended to verify the suitability of the process utilized to estimate knee angle, during the flex-extension (FE) movement performed with the leg model and also during a real walk.

The four configurations involved one sensor placed on the thigh and one on the shank and a fixed sensor as reference. During the preliminary tests a sample frequency of 100 Hz was used. Sensors were cascaded so that sensor on the shank was connected with sensor on the thigh, that related to a reference sensor, which interfaced with the control unit that communicates with MT software. The reference sensor was firmly fixed on the table and its coordinate system has been considered as the local global coordinate system (GCS), so that measurement of sensors placed on the leg model have been referred to this GCS (*figure 28*).

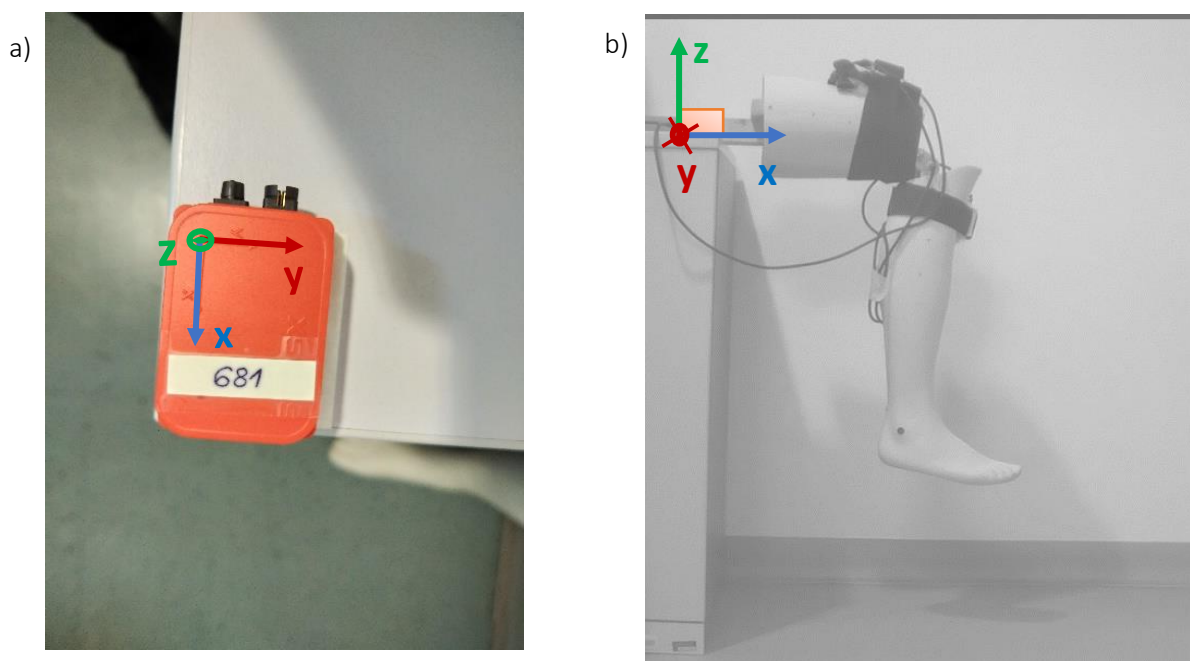


Figure 25 a) Top view of the laboratory fixed sensor. b) lateral view of the laboratory fixed senso, near the leg model

Implants were fixed between the leg and the sensor without any adhesive tape since strapping of the sensor bandage was enough to holding them tightly (*figure 29*). As specified before, implant 1 was placed on the thigh, while implant 2 on the shank.



Figure 29 silicone implant under sensor on the leg



Figure 30 Orientation of coordinate system on sensors on the shank and on the thigh.

For the thigh, three different positions were considered: frontal, lateral, and posterior. Medial position was excluded because during gait the sensor could be easily hit by the contralateral lower limb. For the shank just two position were evaluated: on the lateral side and on the tibial plateau. Posterior and medial position were not assessed primarily to avoid placing the sensor on the gastrocnemius muscle, that could provoke disturbance in collecting signals, and, for the medial position, also for the reason considered for the thigh sensor. Sensors position in any configuration are resumed in *table 7* and represented in *figure 31*. In any configurations, sensors, both on the thigh and on the shank, considering leg in vertical position, were placed with X axis positive pointing down; consequently, Y axis were also on the case sensor plane and Z axis positive pointing outside sensor case (*figure 30*). Sensor fixed in the laboratory was positioned on a horizontal plane, meaning XY plane was approximately parallel to the floor; Z axis was positive pointing up. Trials were performed positioning leg model so that foot pointed as positive X axis of the GCS (*figure 29 b*).

Table 7 Configuration: sensors position

CONFIGURATION	REFERENCE SENSOR	THIGH SENSOR	SHANK SENSOR
1	GROUND	LATERAL	TIBIAL PLATEAU
2	GROUND	FRONTAL	TIBIAL PLATEAU
3	GROUND	POSTERIOR	TIBIAL PLATEAU
4	GROUND	LATERAL	LATERAL

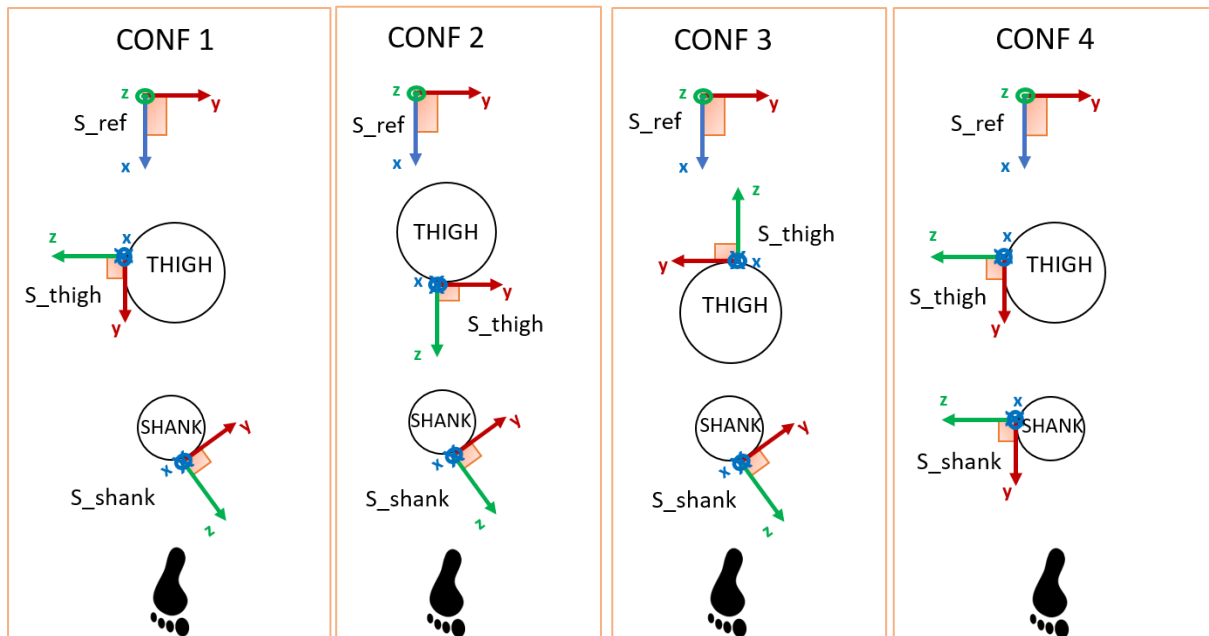


Figure 31 Top view of sensor coordinate systems in each configuration.

All evaluated movements were recorded with a camera from the lateral side, so that relative rotation between shank and thigh could be analysed with Kinovea software, on the sagittal plane (2D). A camera being positioned laterally to the leg model, record the flex-extension movement. The purpose was to frame in such a way that the obtained image 2D represented as much as possible the plane of the movement. Then, with Kinovea tracking tool, coordinates of three marked points were defined during each frame (sample frequency of 50 Hz) of the movement. Markers were chosen so that lines passing through them contain the knee angle.

To assess the influence of sensors placement, in the preliminary laboratory tests, FE movements with the polycentric knee model were recorded using the four configurations. Flex-extension movement has been performed keeping steady the thigh segment horizontally, placing it on the horizontal table surface. Shank segment acted passively the movement, starting from a flexed position (about 90°, as showed in *figure28b*). Relative angle between thigh and shank was calculated from orientation matrix Xsens output. From the three obtained angles, approximation of FE angle was identified and compared

to knee angle derived with Kinovea 2D analysis. Comparing results, one of the four configurations was identified as the best to be used in the following tests.

Then, to evaluate the behaviour of silicone implant and confirm that angle estimation method utilized still result reliable a real gait task was performed. Measurement test was conducted placing sensors on the thigh and on the shank and the two implants were fixed in between the sensors and the lower limb (*figure 32*). Sensors were attached using configuration 1 only on the right leg with their elastic bandages. Test consisted in a one direction straight walk, 5 meters long, at a self-selected speed. The trajectory of the completed route was approximately parallel to the x-axis of the GCS, with opposite direction.

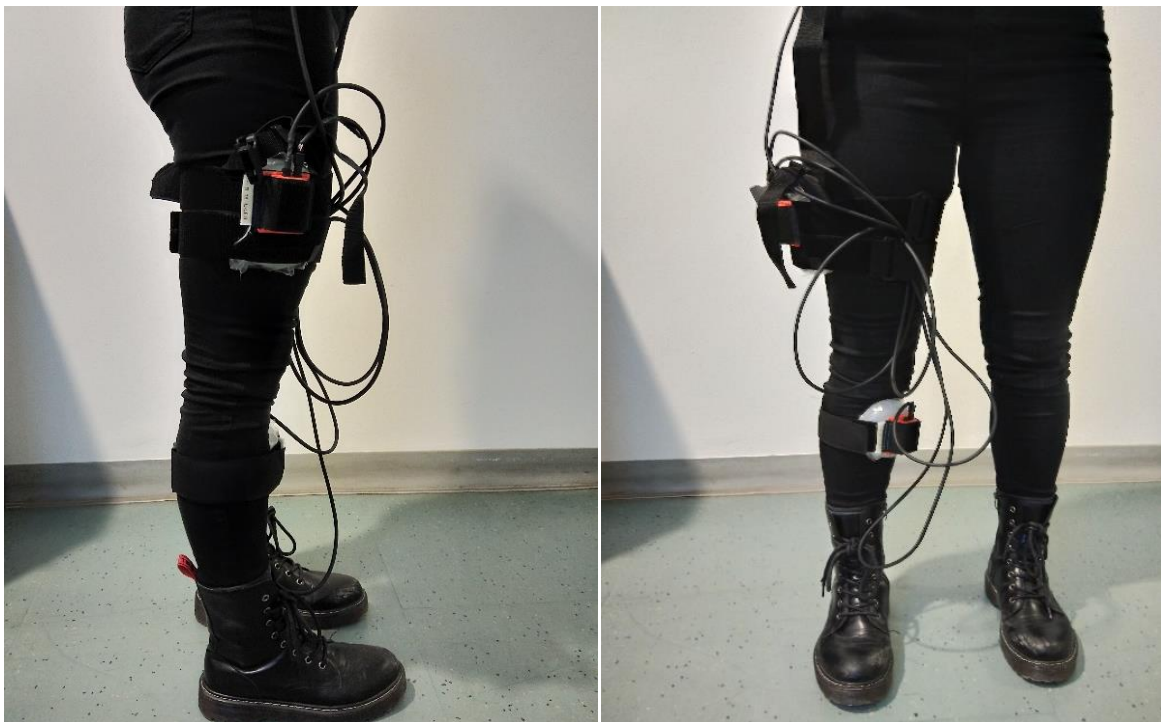


Figure 32 walk test sensors placement (configuration 1)

3.2.2. PROTOCOL: EXPERIMENTAL TEST

The effective experimental trials were performed placing sensors in configuration 1 on the leg model and with a sample frequency of 50 Hz. Trials were carried out placing two sets of sensors on the body segments. Both on the thigh and on the shank, a sensor was placed on the implant and one directly on the leg model. Sensors on the same segment were placed as much as possible one beneath the other, so that each set of sensors was in configuration 1. Implants were attached to the leg model by adhesive tape, and also the sensor were fixed to the silicone implant with another adhesive tape. No elastic bands

were used to fix sensors on the implants or implant on the rigid segment. The aim was to better simulate soft tissue, avoiding an unrealistic steady behaviour of the implants kept in place by the sensors' bandage (figure 33,34). Instead, sensors on the rigid leg surface were firmly fixed using their elastic bands.

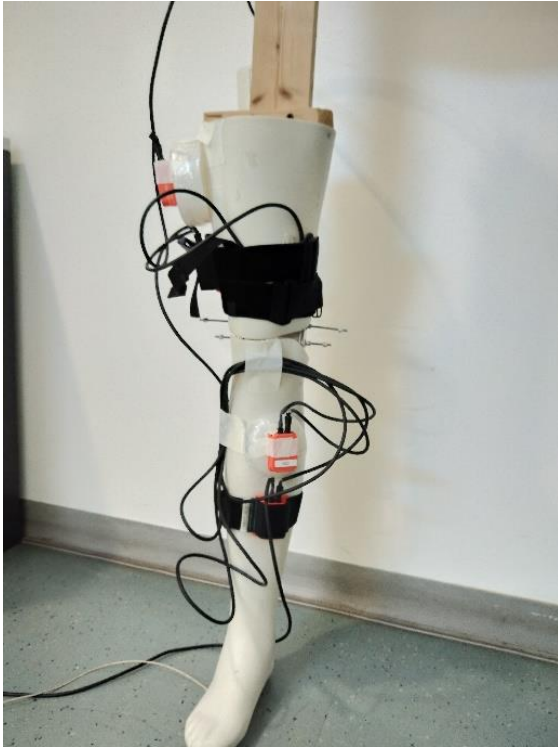


Figure 33 Two sets of sensors placed in configuration 1.



Figure 34 Sensors on the thigh: the top one placed on the silicone implant and the lowest directly fixed un the leg model by the bandage.

Two trials were performed. Firstly, the same trial as the preliminary test was conducted. In addition, to get closer to a real walking movement, flex-extension movement were performed with the leg in vertical position. So, the two trials were (figure 35):

- TRIAL 1: thigh segment was kept steady in horizontal direction and shank segment performed the flex-extension.
- TRIAL 2: thigh segment was kept steady in vertical direction and shank segment performed flex-extension.

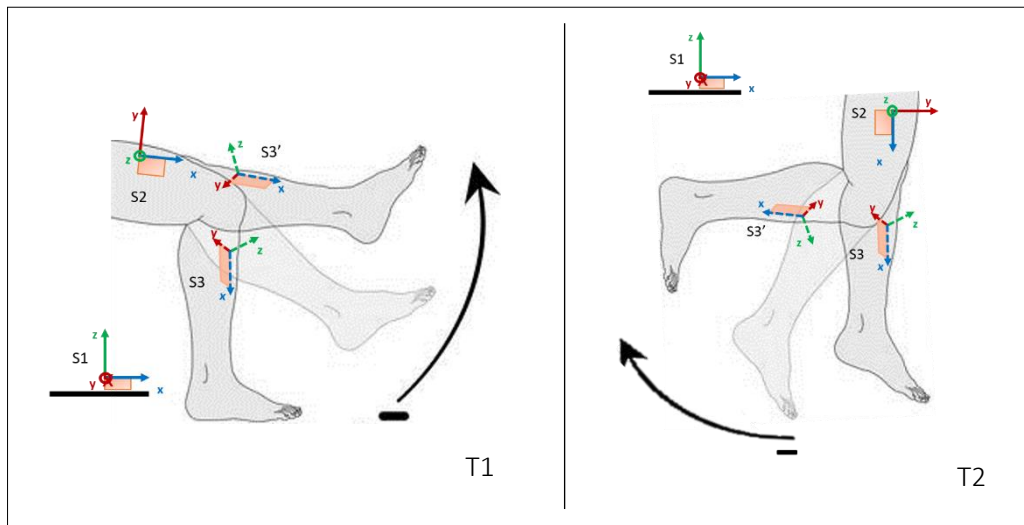


Figure 35 Trial 1 (T1), trial 2 (T2), in configuration 1

For each trial, flex-extension movement has been simulated moving manually the shank segment. To avoid an overly controlled movement, the leg-model foot has been tied to a lanyard through which the movement of the body segment has been induced. Trials have been performed at two different velocity (normal and fast) to evaluate the influence of this parameter on sensor measurements, in presence of soft tissue. Tests performed are resumed in *Table 10*.

Table 10 Test with two sets of sensors in configuration 1

TRIALS		1		2	
VELOCITY		Norm.	Fast	Norm.	Fast
IMU configuration 1	Two sensors on the rigid leg model (thigh and shank)	✓	✓	✓	✓
	Two sensors in the silicone implant (thigh and shank)	✓	✓	✓	✓

Knee angle for trials performed has been firstly estimated from Xsens orientation, as in the preliminary tests. Then, raw data of the gyroscope and of the accelerometer were considered to alternatively calculate sensor orientation, utilizing *imufilter* Matlab function. Orientation data obtained were utilized to estimate angle between thigh and shank segment with same process applied on Xsens output.

After analysing results, the effort has been to improve *imufilter* results by tuning parameter of *imufilter*. *Tune* Matlab function has been utilized to automatically optimize the parameters of the

implemented filter. The optimization algorithm on which tune is based has as its objective a “ground true”, that in this case was the measure provided by Xsens.

3.2.2. DATA ANALYSIS TO CALCULATE KNEE ANGLE

In this section is described how the knee angle was calculated with Kinovea, from Xsens orientation matrix, and finally from linear acceleration and angular velocity using imufilter.

KINOVEA

FE knee angle has been evaluated firstly by a 2D dimension analysis. Each test has been recorded with a video camera and then videos have been processed with Kinovea software, exploiting the program function that allows to identify the trajectory of a single point. After setting the origin of the reference system, three markers have been created in correspondence of three point on the leg model, that define the knee FE angle: M, on the malleus prominence; CoR, approximately on knee model center of rotation; S1, roughly on the thigh segment axis. The three points identified two lines intersecting in CoR point and that describe the knee FE angle (*figure 36*). Trajectories of these three points provide their respective 2D coordinates at each time frame. From points coordinate, angular coefficients of two lines have been calculated and therefore the knee FE angle has been estimated.

Kinovea track output is extracted as .xlsx file and points coordinates are in matrix form:

$$S1 = \begin{bmatrix} x_{S1} & y_{S1} \\ \vdots & \vdots \\ x_{SN} & y_{SN} \end{bmatrix} \quad (N = 1, \dots, N \text{ samples}) \quad (11)$$

$$CoR = \begin{bmatrix} x_{C1} & y_{C1} \\ \vdots & \vdots \\ x_{Cn} & y_{Cn} \end{bmatrix} \quad (12)$$

$$M = \begin{bmatrix} x_{M1} & y_{M1} \\ \vdots & \vdots \\ x_{Mn} & y_{Mn} \end{bmatrix} \quad (13)$$

To define the angular coefficients m_1 and m_2 , the definition of this parameter has been utilized:

$$m = \frac{\Delta y}{\Delta x} \quad (14)$$

So, angular coefficient for each line has been calculated:

$$m_1 = \frac{y_{S1} - y_{CoR}}{x_{S1} - x_{CoR}} \quad (15)$$

$$m_2 = \frac{y_{CoR} - y_M}{x_{CoR} - x_M} \quad (16)$$

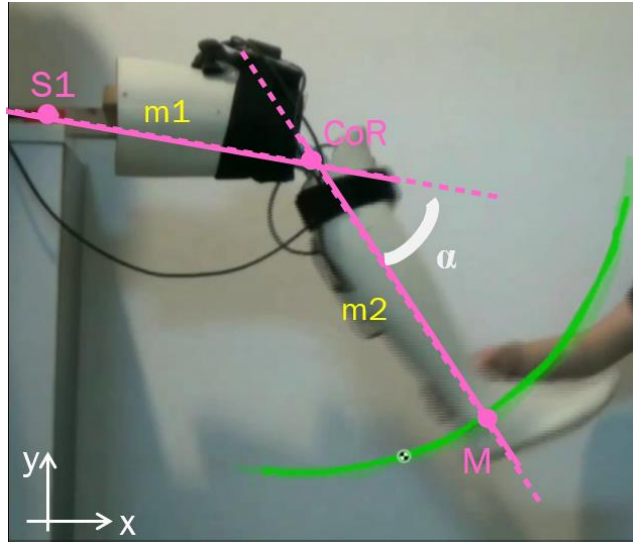


Figure 36 schematic representation of knee FE angle estimation with Kinovea: m_1 and m_2 are the angular coefficient of two lines passing through the three tracked point and determining a knee angle. The green curve represents the M point trajectory.

The value of the angle α between the two identified lines is calculated and it results to vary at each time frame during FE movement:

$$\alpha = \arctg \left(\left| \frac{m_1 - m_2}{1 + m_1 \cdot m_2} \right| \right) \quad (17)$$

Equation (17) identify the acute angle between two lines, means the “external angle” in this case (figure 36). Considering the supplementary angle, instead of the absolute value between thigh and shank segment, allows to obtain a result that is more coherent with the direction of negative rotation in the extension phase.

The trend of the angle value obtained in this phase were used to check the knee flex-extension angle calculated from inertial sensors measurements.

XSENS

In both preliminary test and experimental trials, knee angle has been derived from orientation output by Xsens algorithm. The Xsens “Rotation matrix” output mode returns for each time frame an

array with a row of data in three directions from accelerometer, gyroscope, and magnetometer and the nine elements of the sensor orientation matrix (*table 8*).

Table 8 sensor output "Rotation matrix" mode

1	2	3	4	5	6	7	8	9	10	...
Counter (time)	acc. x	acc. y	acc. z	gyr. x	gyr. y	gyr. z	mag. x	mag. y	mag. z	...

...	11	12	13	14	15	16	17	18	19
	R_{11}	R_{21}	R_{31}	R_{12}	R_{22}	R_{32}	R_{13}	R_{23}	R_{33}

From R_{ij} elements, the rotation matrix, that describes the orientation of the sensor coordinate system (SCS) to the earth fixed coordinate system (ECS), is reshaped:

$${}^{EF}R_S = \begin{bmatrix} R_{11} & R_{12} & R_{13} \\ R_{21} & R_{22} & R_{23} \\ R_{31} & R_{32} & R_{33} \end{bmatrix} \quad (18)$$

The rotation matrix R_{GS} is defined in terms of Euler angles as the combination of three elemental rotations about each of the directions of the reference system.

$${}^{EF}R_S = R_{\psi}^Z R_{\theta}^Y R_{\varphi}^X \quad (19)$$

$${}^{EF}R_S = \begin{bmatrix} \cos\theta\cos\psi & \sin\varphi\sin\theta\cos\psi - \cos\varphi\sin\psi & \cos\varphi\sin\theta\cos\psi + \sin\varphi\sin\psi \\ \cos\theta\sin\psi & \sin\varphi\sin\theta\sin\psi + \cos\varphi\cos\psi & \cos\varphi\sin\theta\sin\psi - \sin\varphi\cos\psi \\ -\sin\theta & \sin\varphi\cos\theta & \cos\varphi\cos\theta \end{bmatrix} \quad (20)$$

For each sensor, a rotation matrix that expresses the orientation of the sensor to the earth fixed system has been achieved. So, for the early two tests phases, in which three sensors have been used, three rotation matrixes have been obtained:

- ${}^{EF}R_G$: orientation of sensor used as a reference in the Earth fixed reference system,
- ${}^{EF}R_{thigh}$: orientation of the sensor on the thigh in the Earth fixed reference system,
- ${}^{EF}R_{shank}$: orientation of the sensor on the shank in the Earth fixed reference system.

To calculate the knee FE angle starting from the initial position, it is necessary to refer measurement of dynamic trial to the correspondent static condition. Before starting each test, the polycentric knee was left in position for five seconds. Therefore, the orientation during this period could be considered not changing significantly and for this reason the orientation matrix of a single instant (e.g., the first or

the last time frame) of time could be assumed sufficient to describe the orientation in static condition. However, for a more reliable and meaningful measurement, the static reference has been considered as the average of all output rotation matrixes during static recording.

For each sensor, this static reference matrix ${}^{EF}R_{Sn_{ST}}$ (Sn identify a generic sensor) is obtained extracting three angles of rotation around axes, for each instant of time, from the output matrix, according to convention described on Xsens Manual.

$$\varphi = \arctan2(R_{32}, R_{33}) \quad (21)$$

$$\theta = -\arcsin(R_{31}) \quad (22)$$

$$\psi = \arctan2(R_{21}, R_{11}) \quad (23)$$

Then, the mean value of each angle has been calculated and the averaged rotation matrix has been derived from them. This procedure has been repeated for all sensors on leg-model segments and for each different trial performed.

$$\varphi_{mean} = \frac{\sum_{i=1}^{N'} \varphi_i}{N'} \quad i = 1, \dots, N' \text{ static samples} \quad (24)$$

$$\psi_{mean} = \frac{\sum_{i=1}^{N'} \psi_i}{N'} \quad (25)$$

$$\theta_{mean} = \frac{\sum_{i=1}^{N'} \theta_i}{N'} \quad (26)$$

$${}^{EF}R_{Sn_{ST}} = \begin{bmatrix} c\theta_m c\psi_m & s\varphi_m s\theta_m c\psi_m - c\varphi_m s\psi_m & c\varphi_m s\theta_m c\psi_m + s\varphi_m s\psi_m \\ c\theta_m s\psi_m & s\varphi_m s\theta_m \sin\psi + c\varphi_m c\psi_m & c\varphi_m s\theta_m s\psi_m - s\varphi_m c\psi_m \\ -s\theta_m & s\varphi_m c\theta_m & c\varphi_m c\theta_m \end{bmatrix} \quad (27)$$

where $\theta_m = \theta_{mean}$, $\varphi_m = \varphi_{mean}$, $\psi_m = \psi_{mean}$.

Orientation in static condition of sensors on the shank and on the thigh, has been referred to the GCS. Sensor that defined the GCS has been placed with the aim to orientate one of its axes almost parallel to the leg-model AoR, so that the plane identified from the other two axis, resulted the one where the FE movement was most. Matrix (28) and (29) describe the orientation of thigh and shank sensors placed with respect to the GCS, in static measurement.

$${}^G R_{thigh_{ST}} = \text{inv}({}^{EF}R_{G_{ST}}) \cdot {}^{EF}R_{thigh_{ST}} \quad (28)$$

$${}^G R_{thigh_{ST}} = \text{inv}({}^{EF}R_{G_{ST}}) \cdot {}^{EF}R_{thigh_{ST}} \quad (29)$$

Similarly, the orientation of the sensors on the leg-model have been referred to the GCS for each instant of time of the dynamic measurements.

$$[{}^G R_{thigh}]_i = inv\left([{}^{EF} R_G\right]_i) \cdot [{}^{EF} R_{thigh}]_i \quad i = 1, \dots, N \text{ samples} \quad (30)$$

$$[{}^G R_{shank}]_i = inv\left([{}^{EF} R_G\right]_i) \cdot [{}^{EF} R_{shank}]_i \quad i = 1, \dots, N \text{ samples} \quad (31)$$

Therefore, to calibrate dynamic trials, the obtained orientation of the sensors on the thigh and on the shank to the GCS have been pre-multiplied by the orientation matrix determined in static condition for the respective trial. This calibration procedure enables to consider orientation of the sensors relatively to their initial position.

$$[{}^G R_{thigh}]_i = {}^G R_{thigh_{ST}} \cdot [{}^G R_{thigh}]_i \quad i = 1, \dots, N \text{ samples} \quad (32)$$

$$[{}^G R_{shank}]_i = {}^G R_{shank_{ST}} \cdot [{}^G R_{shank}]_i \quad i = 1, \dots, N \text{ samples} \quad (33)$$

Then to obtain the orientation of sensor on the shank to the sensor on the thigh, the relative rotation matrix has been determined, for each time frame:

$${}^{thigh} R_{shank} = inv\left([{}^G R_{thigh}]_i\right) \cdot [{}^G R_{shank}]_i \quad (34)$$

The obtained matrix has the same configuration reported on Xsens Manual and so the Euler angles, correspondent to segments relative orientation, have been calculated using equations (21), (22), and (23). Angles have been extracted for each instant to observe the variation during knee flex-extension movement.

A summary of the procedure described here is reported in *figure 37*. It has been applied both in preliminary tests to four configuration and in experimental tests to each set of sensors placed in configuration 1.

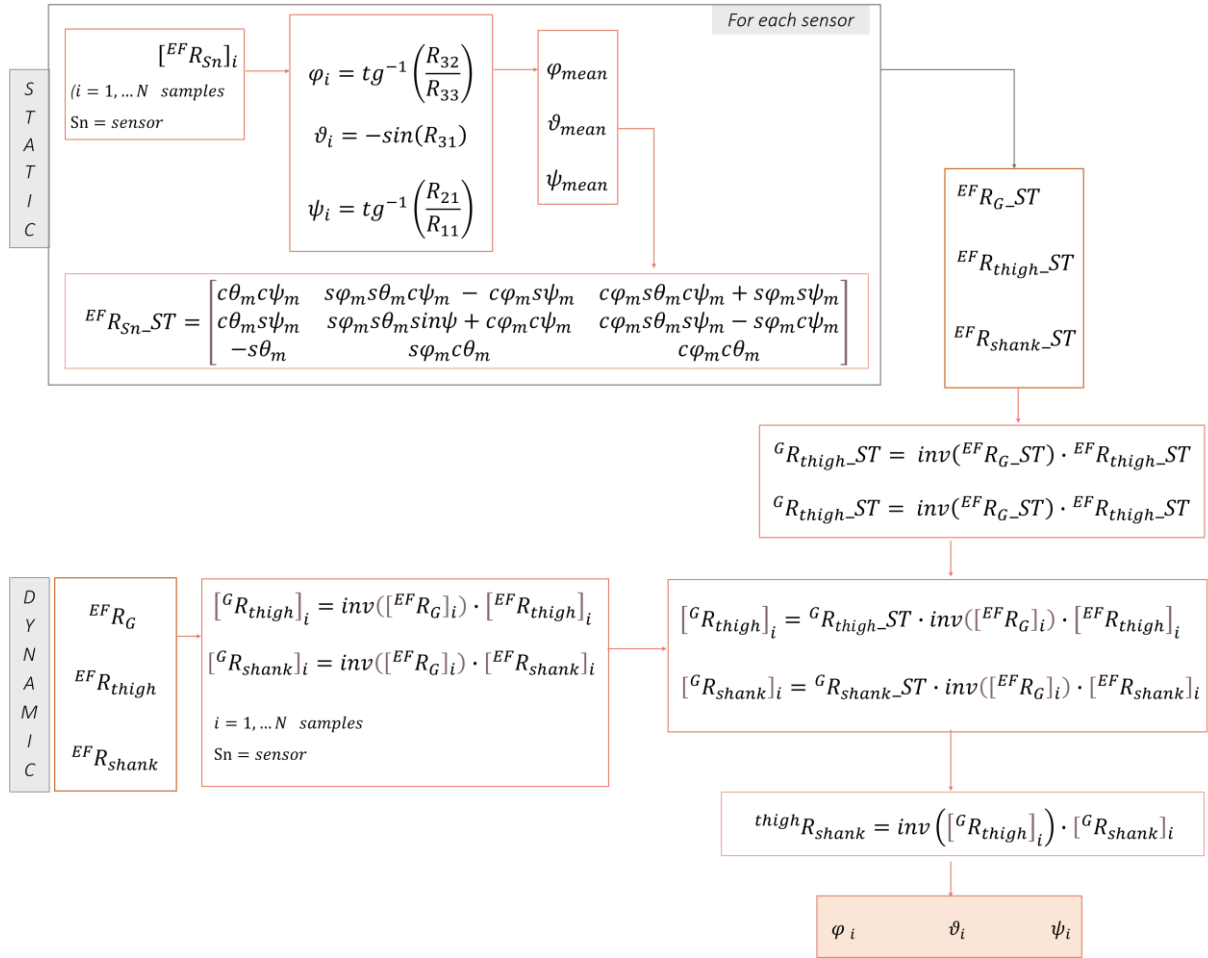


Figure 37 block diagram of knee angle calculation from Xsens output orientation

ORIENTATION FROM RAW DATA: IMUFILTER

Moreover, raw data from accelerometer and gyroscope have been considered to calculate orientation from a post elaboration procedure. The aim was to achieve knee flexion-extension results in agreement with those obtained from Xsens, but starting from linear acceleration and angular velocity data. The raw data considered have been elaborated with *imufilter* Matlab function, that takes as input linear acceleration and angular velocity from sensor readings and output orientation and filtered angular velocity. The system object created by this function is an indirect Kalman filter, that uses a nine-element state vector to track error in the orientation estimate, the gyroscope bias estimate and the

linear acceleration estimate. The system object defined for this study had the properties resumed in *table 9*.

Table 9 Imufilter properties

PROPERTIES	VALUES
Sample Rate (Hz)	Sensor measurement frequency: 50
Decimation Factor	Default: 1
Accelerometer Noise (m/s ²) ²	0.0006
Gyroscope Noise (rad/s) ²	0.0002
Gyroscope Drift Noise (rad/s) ²	Default: 3.0462e-13
Linear Acceleration Noise (m/s ²) ²	0.0025
Linear Acceleration Decay Factor	Default: 0.5
Initial Process Noise (Matrix 9x9)	Default
Orientation Format	Rotation Matrix

The first 9 columns in the Xsens rotation matrix output mode (*table 8*) contain linear acceleration, angular velocity, and magnetic field measurement, in three directions of the SCS. As well as for orientation matrix, also for raw data it is possible to know values for each instant of time (in rows), so as to be able to evaluate the trend in time. Indeed, imufilter allows to reconstruct the orientation matrix for each instant starting from linear acceleration and angular velocity data. Therefore, the purpose is to obtain rotation matrix similar to the ones directly output from sensors filter and calculate flex-extension angle with the same procedure related before.

To calibrate measurements, sensors orientation during dynamic trials have been referred to the static orientation, as in the previous procedure. As static reference, firsts 15 samples of record were considered to calculate an averaged orientation matrix. From static period, the mean value of acceleration and angular velocity have been computed.

$$acc_{Sn,mean} = \frac{\sum_{i=1}^{N'} [acc_{Sn}]_i}{N'} \quad i = 1, \dots, N' \text{ static instant} \quad (21)$$

$$gyr_{Sn,mean} = \frac{\sum_{i=1}^{N'} [gyr_{Sn}]_i}{N'} \quad (22)$$

$acc_{S,mean}$ and $gyr_{S,mean}$ values have been used as input in imufilter function, obtaining a unique orientation matrix, relative to the static record. This procedure has been repeated for any sensor, obtaining a static matrix describing the orientation the earth fixed coordinate system with respect to

the sensor system. As well as in previous described procedure, to define relative orientation between shank and thigh, matrixes that expressing orientation of SCS to ECS are needed. Therefore, *imufilter* output matrixes have been inverted obtaining ${}^{EF}R_{thigh_{ST}}$, ${}^{EF}R_{shank_{ST}}$, and ${}^{EF}R_{G_{ST}}$.

Then orientation in static condition, of each sensor attached on a body segment, has been referred to the static GCS, by pre-multiplication to the static matrix of the fixed sensor. (equation 29 and 30)

As regards dynamic trials, for any instant, acceleration and angular velocity vectors have been input in *imufilter* function, that calculates the correspondent orientation. Also, these matrixes have been inverted to obtain orientation of SCS to ECS. Then the orientation of sensor on the thigh and on the shank were referred to the GCS. (equation 31 and 32)

Therefore, for each sensor, orientation during dynamic measurement, expressed in GCS, has been calibrated with respect orientation in static condition, also in GCS. For achieve this result, the dynamic rotation matrix relative is pre-multiplied, at any instant of time, by the static rotation matrix. (equation 34)

As well as for matrix output from Xsens, knee angles were extracted from rotation matrix obtained, describing relative orientation between thigh and shank. Convention declared by the Xsens manual was considered and Euler angles were calculated with equations (21), (22), (23). This procedure is summed up in *figure 38*.

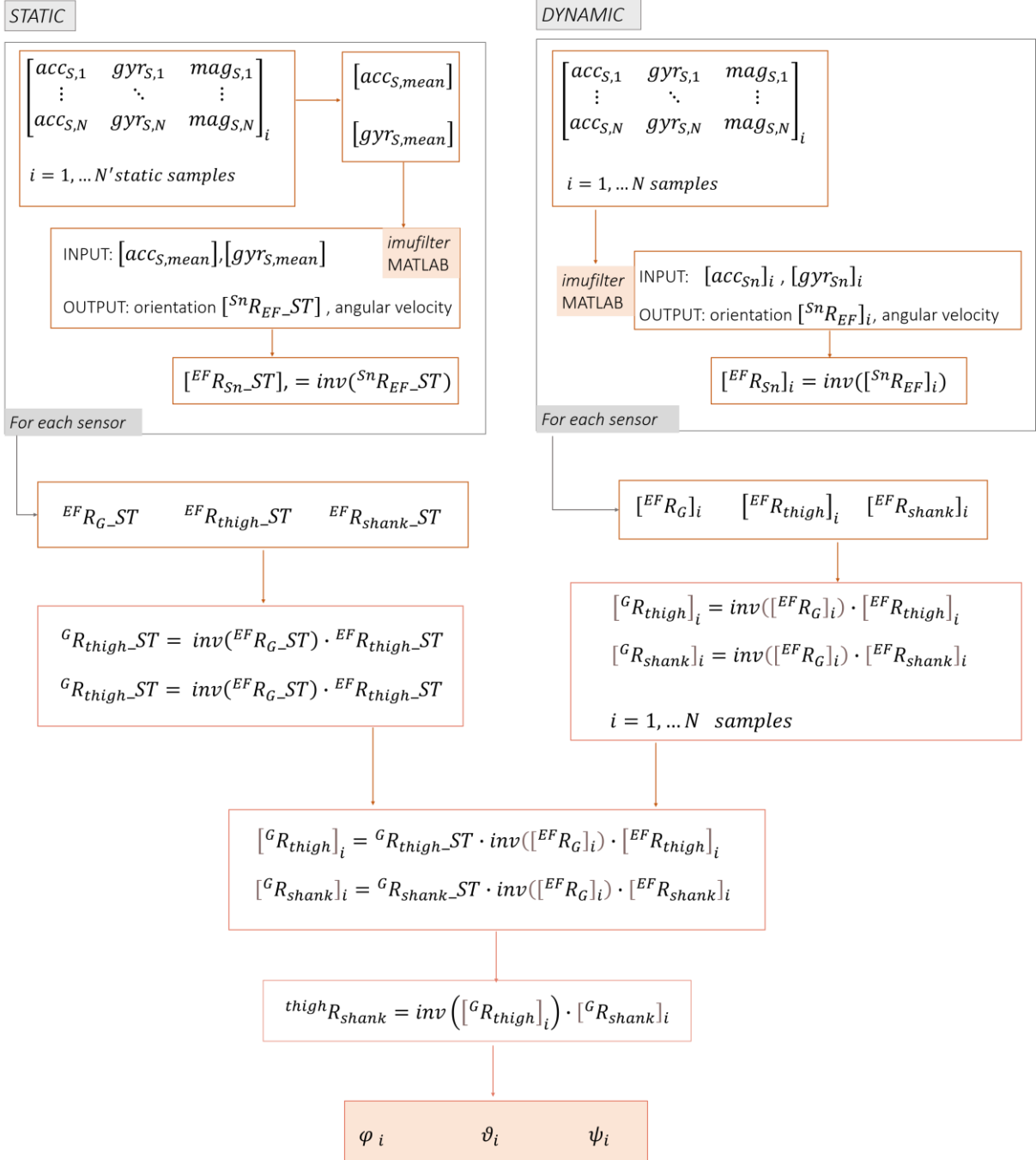


Figure 38 Block diagram of process to estimate knee angles from raw data.

To improve knee flex-extension results achieved, parameters of the implemented filter could be modified to identify a better performance. So, the Matlab function *tune* has been used to automatically adjust the properties of the *imufilter* to reduce estimation error. The function fuses the sensor data to estimate the orientation and uses the comparison to the orientation considered as reference, means orientation output from Xsens algorithm, to enhance estimation. *Tune* consists of an

optimization algorithm, that utilises as initial condition the property values in the imufilter implemented. Parameters optimized with this function are accelerometer noise, gyroscope noise, gyroscope drift noise, linear acceleration noise and linear acceleration decay factor. The function computed a hundred iterations, five iteration for twenty cycles.

Sensor orientation has been estimated again with filter updated with tuned parameters. As with initial filter, raw accelerometer and gyroscope data were input in the filter and angle between thigh and shank has been estimated as described before. *Figure 39* is an infographic of this procedure.

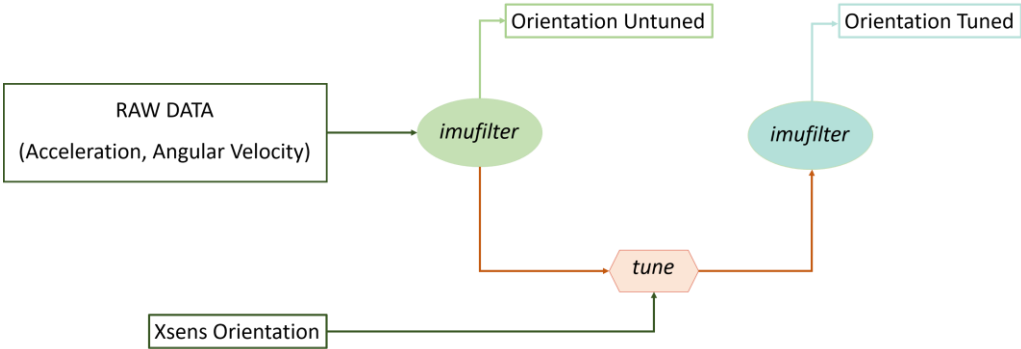


Figure 39 Block diagram tune functioning

4. RESULTS

4.1 PRELIMINARY TESTS

First tests performed aimed to evaluate two aspects: (i) the best sensors' configuration and (ii) testing the manufactured silicone implants.

The 2D evaluation of knee FE angle, defined with Kinovea, were used to monitor the trend of the angle of interest, on the approximate sagittal plane. Angle values obtained with Kinovea tracking, depend greatly on point tracked position, are influenced by camera position, from which depends the orientation of the plane which calculation are done on. Nevertheless, with the necessary measures, good results can be achieved and can be used to monitor knee flexion-extension movements. So, angles estimated from Xsens output orientation, have been compared with Kinovea angles. Graphics (*figures 40-43*) show angles referred to respective firsts static samples averaged values. Time axis cannot be overlapped since sensor and camera registration were not synchronized.

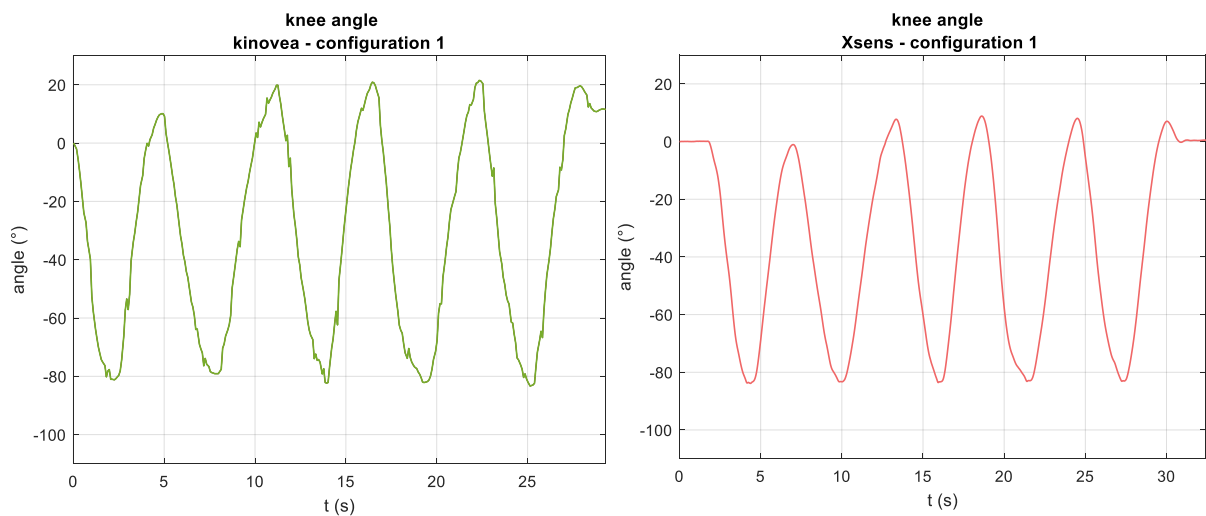


Figure 40 Knee angle estimated with Kinovea track (left) and with Xsens algorithm (right). configuration 1

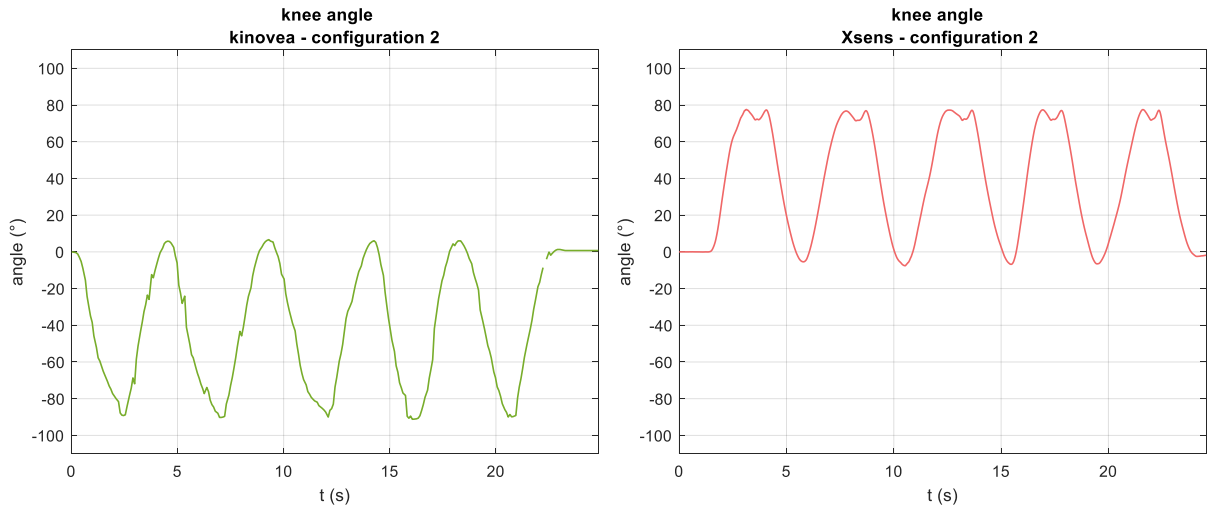


Figure 41 Knee angle estimated with Kinovea track (left) and with Xsens algorithm (right). configuration 2

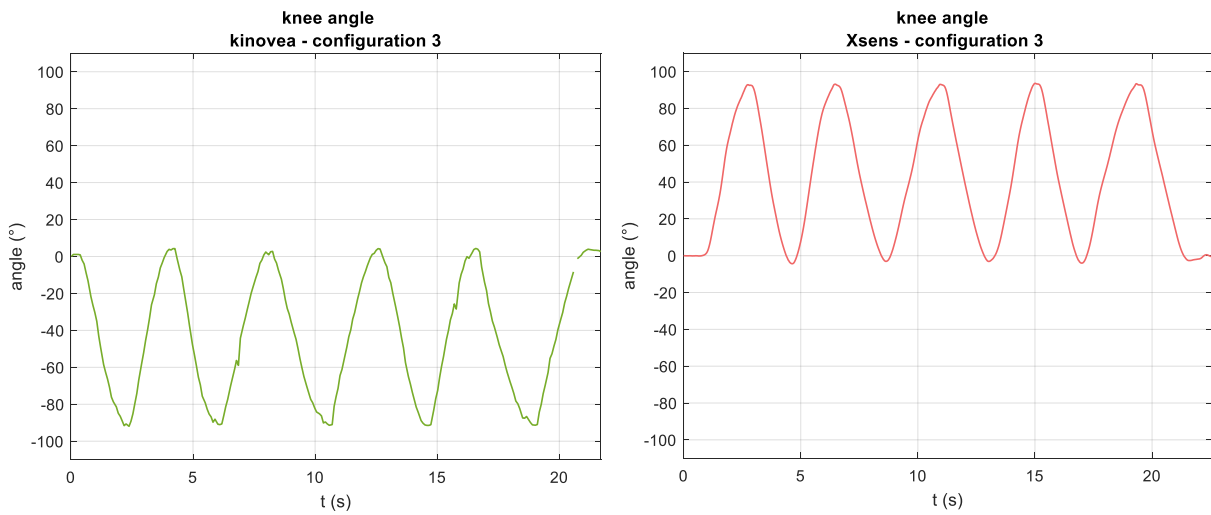


Figure 42 Knee angle estimated with Kinovea track (left) and with Xsens algorithm (right). configuration 3

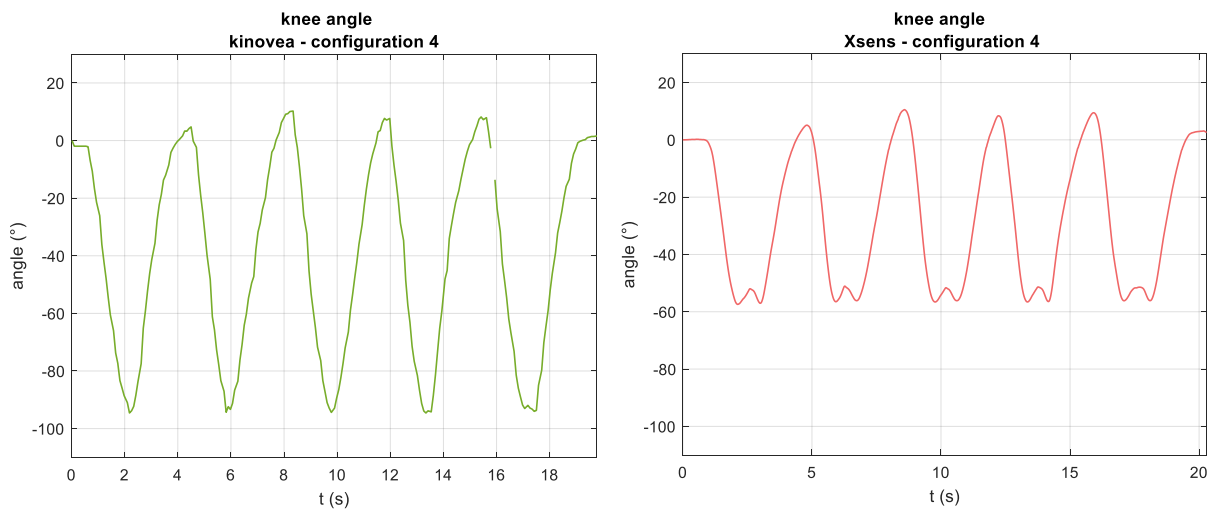


Figure 43 Knee angle estimated with Kinovea track (left) and with Xsens algorithm (right). configuration 4

Overall, it could be observed that Xsens algorithm is able to output orientation data that allow to estimate pretty correctly knee FE angle values. Indeed, for three out of four configuration (configurations 1,2,3), a sinusoidal trend, with an amplitude of approximately 90°, has been obtained. Only with sensors placed in configuration 4, the angle of interest results underestimated. Since this is the unique configuration in which sensor on the shank was placed lateral side instead of on the tibial plateau. The different performance could be due to the shank sensor position. Configuration 2 and 3 leads to estimate the angle with opposite direction of rotation, to the expected one.

To assess quantitatively difference in angle estimated with the two methods, range of motion (ROM) of the flex-extension movement has been calculated. First, the ROM values for each cycle have been compared. Then, both for Kinovea and Xsens data, the mean value and the standard deviation parameter have been derived. Finally, the difference of the two means was calculated for each configuration. *Table 10* summarizes the numerical values considered.

Bar plots in *figure 44* compare ROM values, showing mean values and standard deviation interval for any configuration. Overall Xsens algorithm appears to output sensors' orientation that lead to underestimated knee angle amplitude. Nevertheless, barring configuration 4, differences between Kinovea mean and Xsens mean values, in any configuration, are below 15°. So, discrepancies can be considered acceptable, allowing to confirm that Xsens algorithm is reliable also in presence of the implants to simulate soft tissues and to assess that angle estimation procedure is appropriate.

Therefore, the preliminary tests allow to identify the configuration 1 as the best configuration for the next test phase.

Table 10 Knee angle minimum and maximum values estimated by Kinovea (K) and Xsens (X) for each cycle, for any configuration. For each configuration maximum, minimum and ROM value for each cycle and relative mean and standard deviation values.

Configuration		CYCLE 1		CYCLE 2		CYCLE 3		CYCLE 4		CYCLE 5		Mean ROM ± Dev.St ROM (°)		Mean ROM _K – mean ROM _X (°)
		K	X	K	X	K	K	K	X	K	X	K	X	
1	Max	21.4	46.2	23.2	47.9	22.6	48.7	11.8	47.6	21.5	38.8			
	Min	-85.1	-46.1	-83.8	-46.2	-84.0	-46.6	-80.8	-46.3	-82.9	-46.9			
	ROM	94.7	85.7	102.3	93.9	106.6	95.3	107.0	93.1	106.4	94.1	104.9 ± 5.3	92.4 ± 3.8	12.5
2	Max	3.4	83.4	8.1	83.1	8.2	83.7	8.8	83.7	7.9	83.5			
	Min	-91.4	2.5	-92.6	-1.6	-91.5	-1.8	-91.7	-2.6	-90.6	-0.5			
	ROM	97.9	86.3	99.8	84.0	99.0	85.6	100.1	84.6	94.1	81.0	98.8 ± 2.4	84.3 ± 2.1	14.5
3	Max	5.4	65.9	5.8	66.5	5.7	66.7	4.2	66.1	5.7	66.2			
	Min	-92.8	-32.4	-92.9	-33.8	-92.8	-32.9	-92.5	-32.9	-93.4	-34.2			
	ROM	99.8	99.6	97.3	100.8	99.2	99.8	99.3	101.2	98.8	99.6	99.5 ± 0.4	100.2 ± 0.7	0.7
4	Max	-4.7	9.7	0.6	9.1	1.7	11.7	2.8	6.2	-2.7	-68.0			
	Min	-95.7	-66.7	-96.3	-67.1	-96.1	-67.2	-96.0	-67.1	-96.3	-68.0			
	ROM	102.5	64.7	107.7	67.1	105.2	69.3	105.9	68.2	97.1	61.4	104.1 ± 4,1	66.1 ± 3.1	38.0

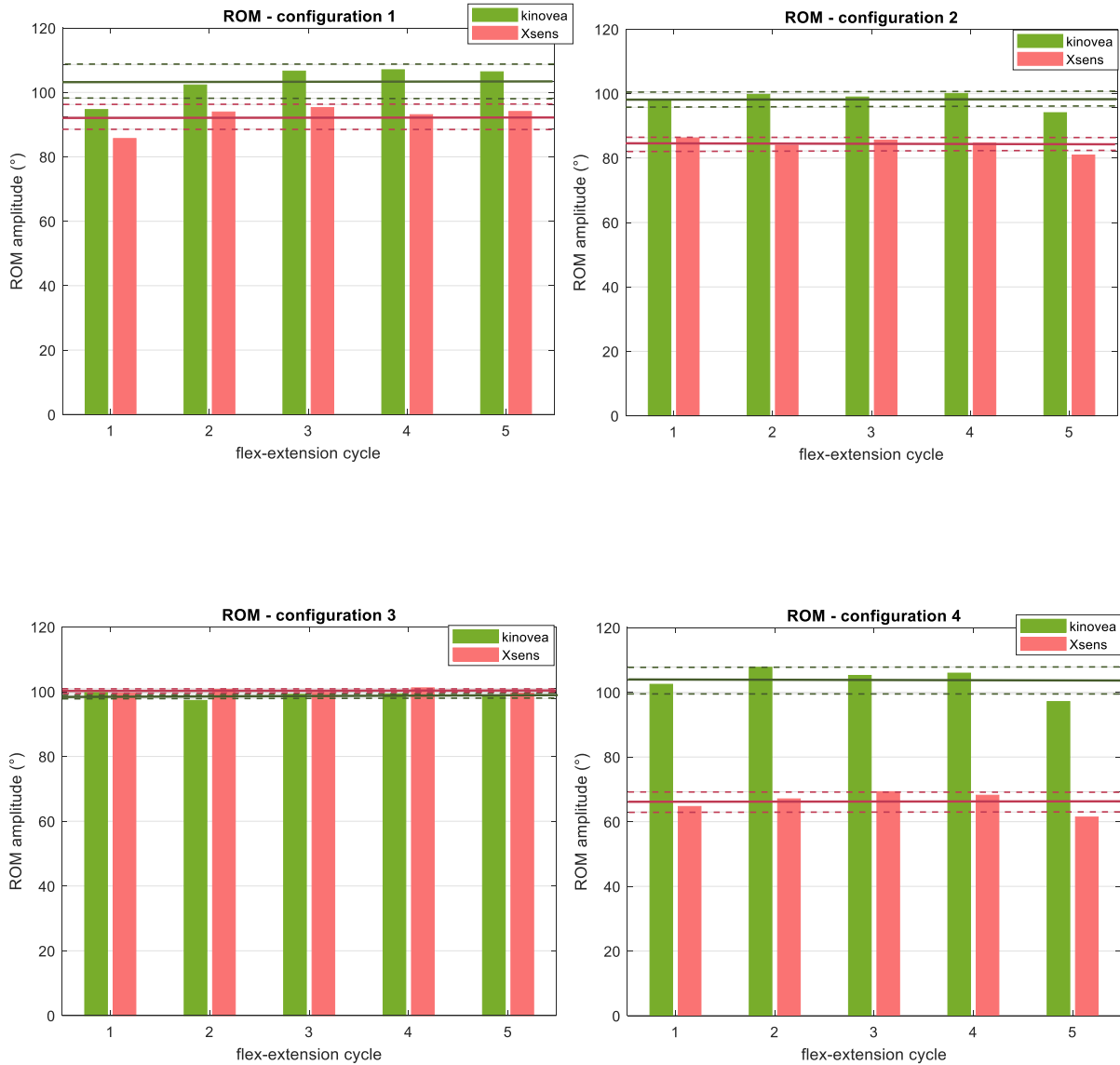


Figure 44 Comparison between Kinovea (green) and Xsens (red) ROM absolute value for each cycle of flex-extension movement. Mean value (continuous line) and standard deviation (broken lines) on all cycles are represented.

Walking test has been carried out to evaluate the estimation of knee angles in presence of simulated soft tissues, during a real gait movement with sensors placed in configuration 1. Knee angle has been calculated from Xsens output orientation, with the same procedure utilised for precedent test on leg model. So also in this case orientation of sensors on the thigh and on the shank have been referred to the laboratory fixed reference sensor. The walk was carried out with a trajectory approximately parallel to the X axis of the laboratory GCS, but with opposite direction, as subject feet point negative X axis. Consequently, the Y axis is positive pointing from medial to lateral side of the right leg on which sensors are attached. For this reason, the flexion movement is represented as a negative rotation, while extension has positive value.

Knee angle estimated in this trial (*figure 45*) has an average ROM value of $(49.2 \pm 6.3)^\circ$ (*table 11*). Angle graphic shows a periodical trend with a higher frequency compared with precedent trial, compatible with a faster movement performed. The shape of the signal differs a little from the knee angle standard one. Leaving aside possible specific characteristics of the subject walk, anomalies could be due to the coordinate system to which measurement are referred, since real functional axes of the joint are not being involved. However, it can be stated that also during a real gait, sensors and angle estimation procedure are suitable, even in presence of simulated soft tissues.

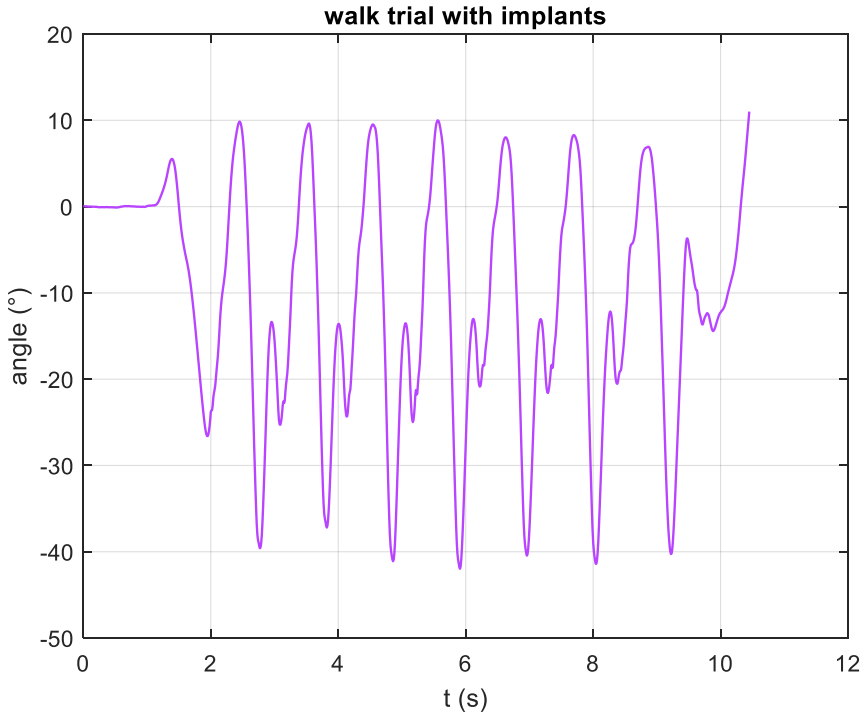


Figure 45 Knee angle during walk trial, in presence of simulated soft tissues

Table 11 Knee range of motion during walk trial

	ROM (°)								Mean ROM ± Dev.St ROM (°)
CYCLE	1	2	3	4	5	6	7	8	
	34.3	51.6	48.9	52.7	54.1	50.6	51.8	49.3	49.2 ± 6.3

4.2 EXPERIMENTAL TRIALS

4.2.1 XSENS RESULTS

For the next phase, sensors were attached to the leg both with and without implants, to better compare measurement in presence of soft tissues. Indeed, it allows to compare Xsens measurement in presence of soft tissue artifact, with the same Xsens algorithm' result in case of soft tissue absence. So, for these tests, angle estimated from sensors on the rigid part of the leg model were considered as the "real values" and the distance from them was evaluated for angles estimated from sensors fixed on the implants.

Angles estimated with Xsens orientation output, from the two sensors set (on the rigid part or on the implant) have been directly compared on the same graphic, since they regard the same performed movement. Comparison has been assessed for horizontal trial (trial 1, *figure 46*) and also for a vertical trial (trial 2, *figure 47*), that better approximates the walk movement. Graphic generated indicate a really good match of the two angle signals in trial 2, while for trial 1 measurement with sensors on the implants do not reaches the peaks values measured by sensors on the rigid part. The inversion of the peak observed could be related to the oscillatory movement due to the silicone implant presence. It could be more evident in trial 1, where the thigh segment is held fix in a more stable way, making the silicone oscillation freer. It is possible that in trial 2, where the thigh segment was kept steady holding it in hands, the silicone implant followed more the leg-model movement, without suffering a "recoil". In addition, compared to previous tests in which this behaviour was not observed in configuration 1, the different way in which implants and sensors were attached can be considered. In the firsts tests silicone was less free to oscillate as held by sensors band.

It also can be observed that, for both trials, while for the first cycles the two signals are almost perfectly overlapped, towards the end the matching decreases. Signals compared are affected by different drift errors that are better corrected at the beginning of the measurements.

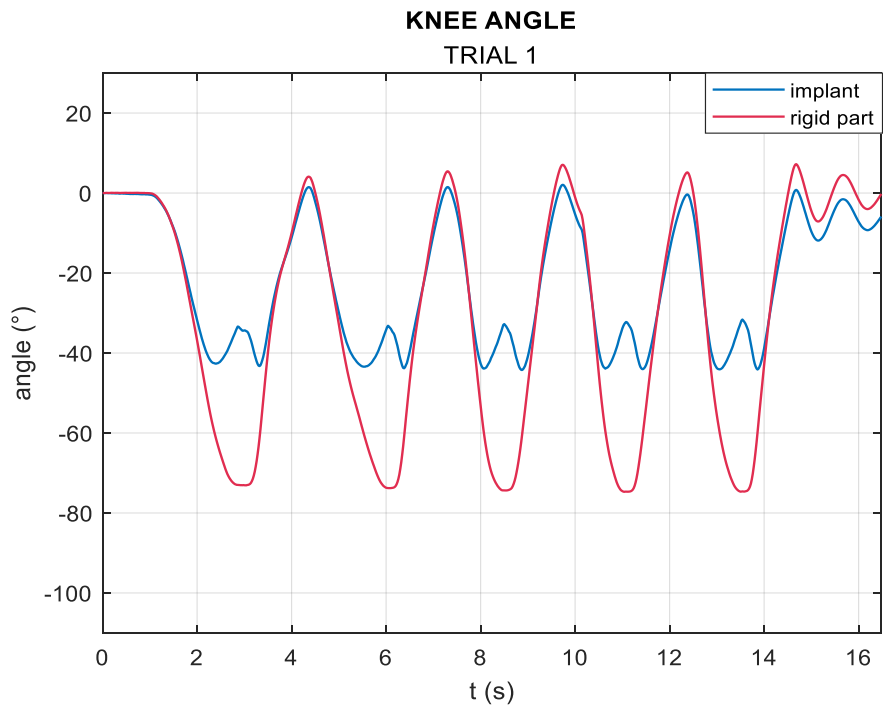


Figure 276 Comparison between knee angle estimated by sensors on the implants and sensors directly on the rigid leg surface. (Trail 1)

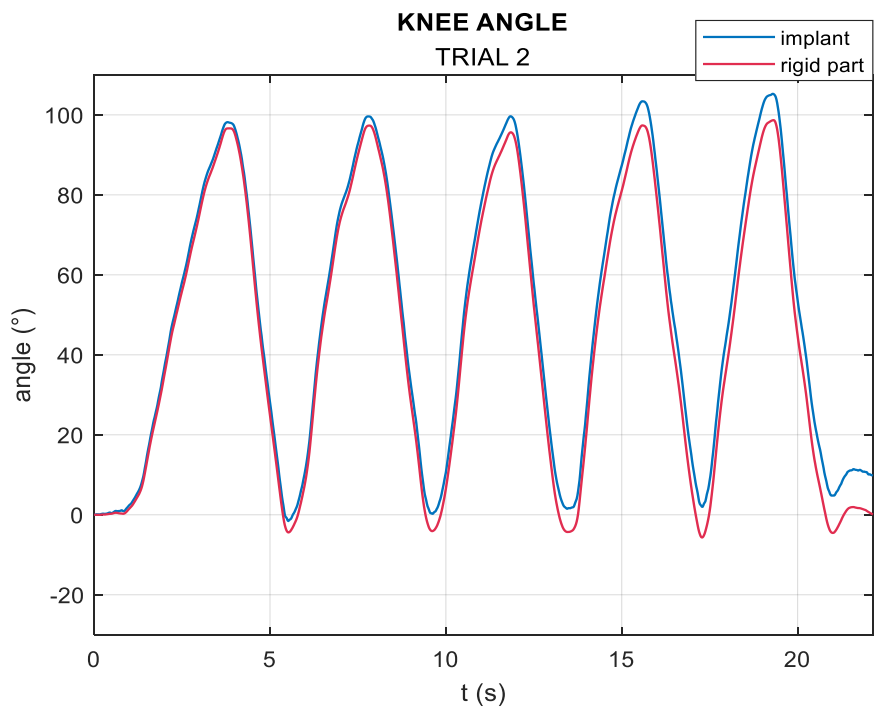


Figure 47 Comparison between knee angle estimated by sensors on the implants and sensors directly on the rigid leg surface. (Trail 2)

Angular signals analysed in the two trials have been compared quantitatively with RMSE (Root Mean Square Error) parameter that indicates the mean discrepancy between the values of angle calculated from sensors on the implant measurement and of angle from sensors on the rigid part. RMSE results are reported in *Table 12*.

$$RMSE = \sqrt{\frac{\sum_{i=1}^N (\vartheta_{i,implant} - \vartheta_{i,rigid_{part}})^2}{N}} \quad N \text{ samples} \quad (35)$$

Table 12 RMSE between measurement of the two set of sensors utilized, for trial 1 and trail 2.

	T1	T2
RMSE (°)	17.2	5.4

Obtained values verified what expected, since in trial 1 RMSE results higher demonstrating a worse match between measurement. Moreover trial 2 has a low RMSE, confirming that, at least for vertical trial, the Xsens algorithm results reliable despite of soft tissue artifact influence.

4.2.2 IMUFILTER RESULTS

Furthermore, the *imufilter* Matlab function has been utilised to evaluate the orientation measurement from raw data of accelerometer and gyroscope. Parameters of the implemented filter have been tuned by *tune* Matlab function, as described. Knee angle has been calculated before and after parameters tuning. If sensors orientation obtained with *imufilter* untuned do not allow to calculate a realistic angle value, tuned parameters lead to significantly better results. Knee angles derived from Xsens algorithm and from *imufilter* untuned and tuned have been compared in a unique plot, both for sensors directly attached to the leg and for sensors on the silicone implants (*figures 48-51*).

Angles calculated for the trial 2 can be considered a good result since signals have similar shapes, differing for amplitude of the wave. In addition, as expected, *imufilter* tuned lead to an intermediate value of the knee angle, closer to the Xsens result than *imufilter* untuned one. On the contrary, in the trial 1, untuned *imufilter* does not allow to achieve a realistic flex-extension angle. With tuned *imufilter* a signal similar to Xsens angle is obtained, but with opposite values. This aspect cannot be considered totally negative, because if *imufilter* signal was inverted, it would match rather with Xsens signal. The opposite sign of the angle may be due to the behaviour in the static condition to which the dynamic orientation is referred.

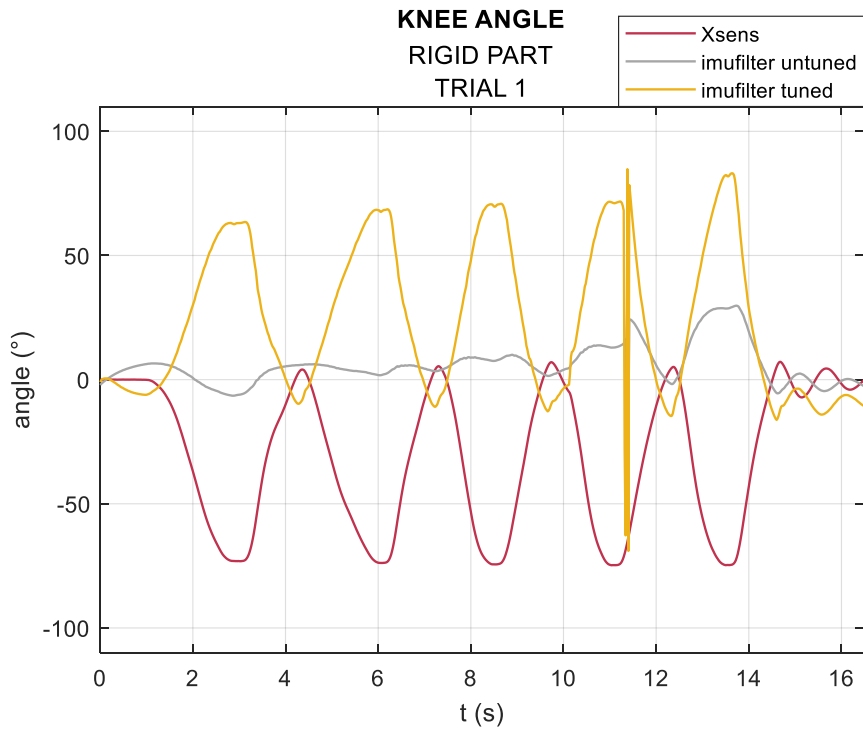


Figure 48 Comparison of knee angle obtained with Xsens algorithm, imufilter function untuned and tuned, for sensors on the rigid part. Trial 1

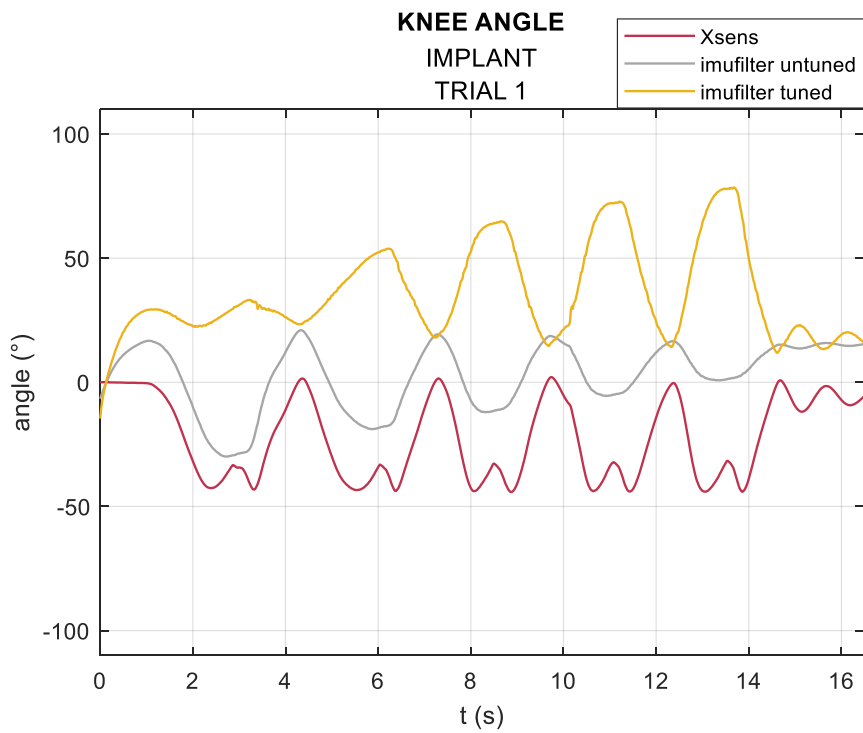


Figure 49 Comparison of knee angle obtained with Xsens algorithm, imufilter function untuned and tuned, for sensors on the implants. Trial 1

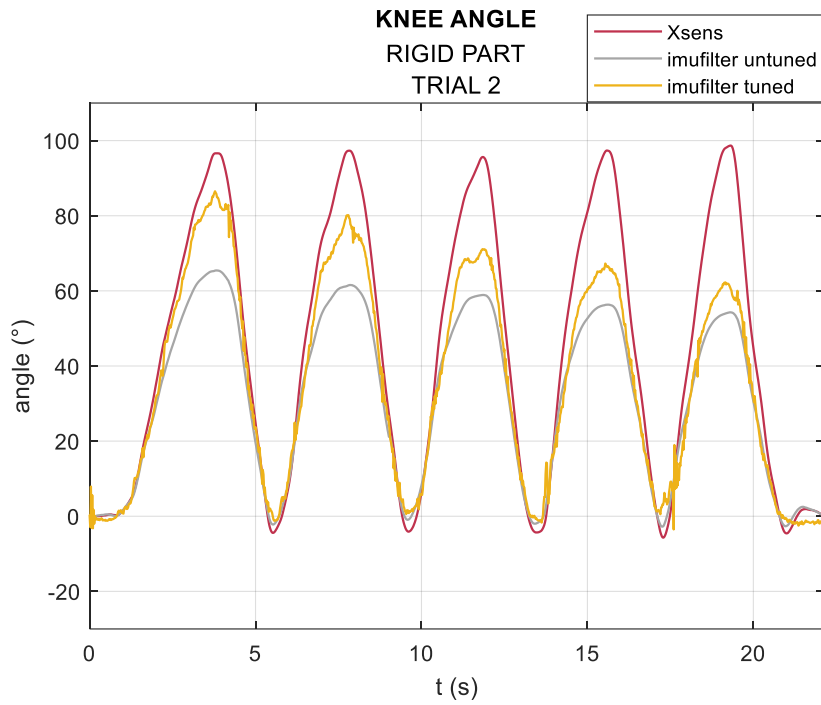


Figure 50 Comparison of knee angle obtained with Xsens algorithm, imufilter function untuned and tuned, for sensors on the rigid part. Trial 2

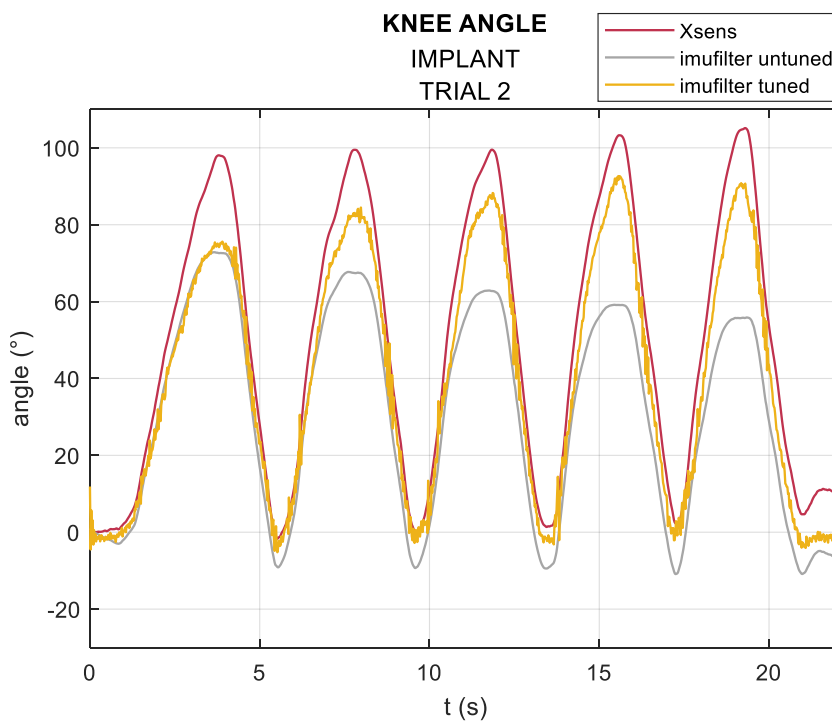


Figure 51 Comparison of knee angle obtained with Xsens algorithm, imufilter function untuned and tuned, for sensors on the implants. Trial 2

Fast trials (figure 52-55) carried out both in horizontal and in vertical position lead to similar considerations of trials at normal speed. Indeed, also for fast trials, differences related to the type of movement can be found. Moreover, application of *imufilter* tuned enhance results particularly in presence of simulated soft tissue. However, what is worth considering is the comparison between correspondent trials at different velocities. Specifically, it can be observed that in fast trials knee angle does not result negative, in opposition to the expected value. Instead, an anomalous shape is observed for the trial 2, for the angle derived from sensors on the rigid leg surface, while sensors on the implants maintain an attitude similar to that of the trial at normal speed. Focusing on the measurement of the fast trial 2 relative to sensor on the rigid part, it can also be noticed that *imufilter* untuned leads already to a signal really matching with Xsens angle. Maybe for this reason the tuning of parameters gets worse.

So, it can be assumed that the velocity of the movement influenced the *imufilter* performance and that, overall, a faster movement lead to better results. However, it needs to consider the variability of each trial, since also other environmental variables can affect measurements. Next experimental tests concern only the slow trials to decrease the number of variables and focus on filter characteristics.

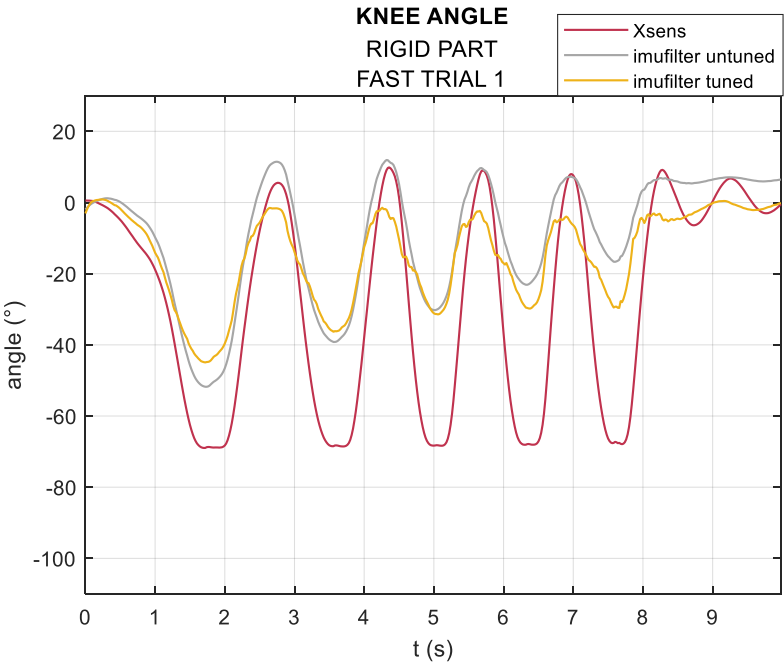


Figure 52 Knee angle from orientation output of Xsens, *imufilter* untuned and *imufilter* tuned of sensors on rigid part. Trial 1 fast

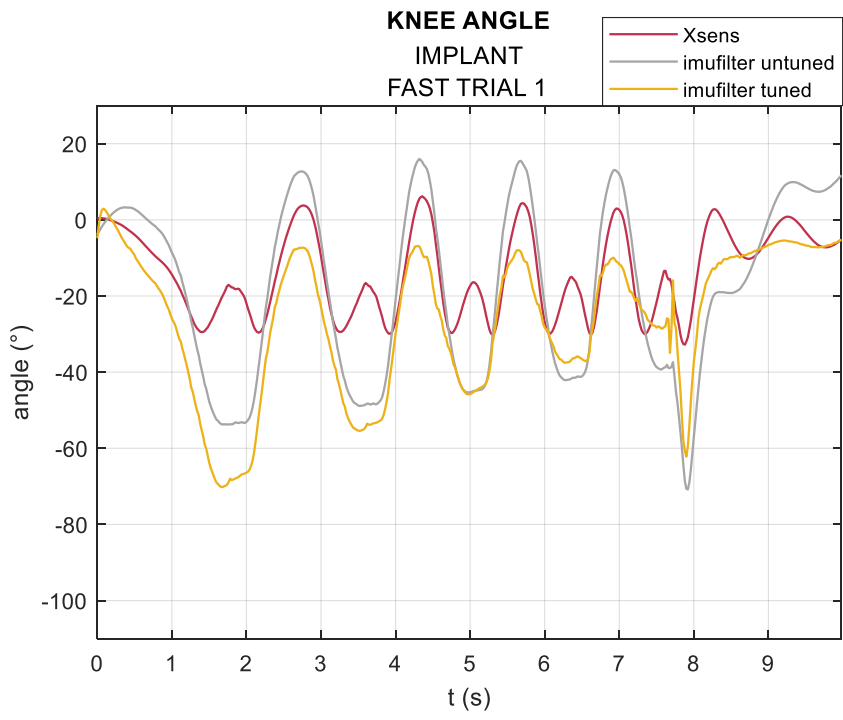


Figure 53 Knee angle from orientation output of Xsens, imufilter untuned and imufilter tuned of sensors on implants. Trial 1 fast

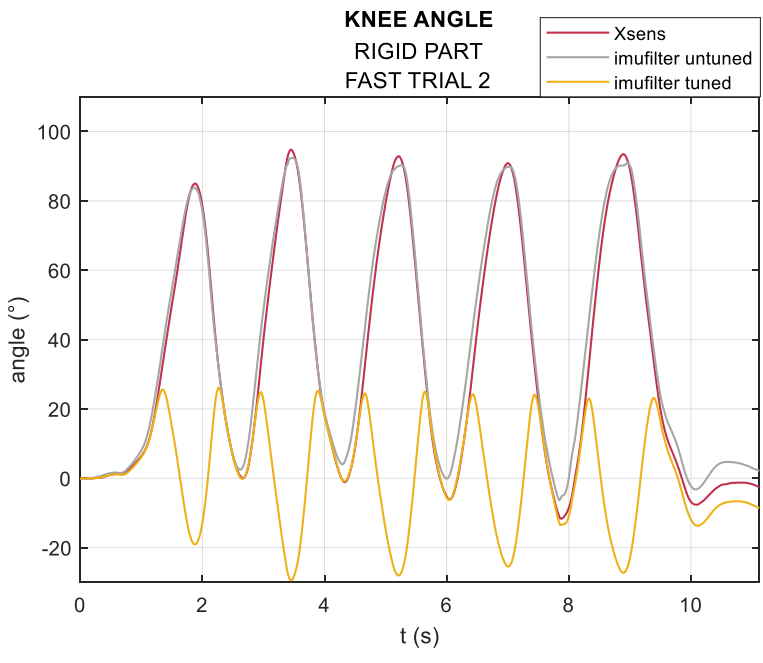


Figure 54 Knee angle from orientation output of Xsens, imufilter untuned and imufilter tuned of sensors on rigid part. Trial 2 fast

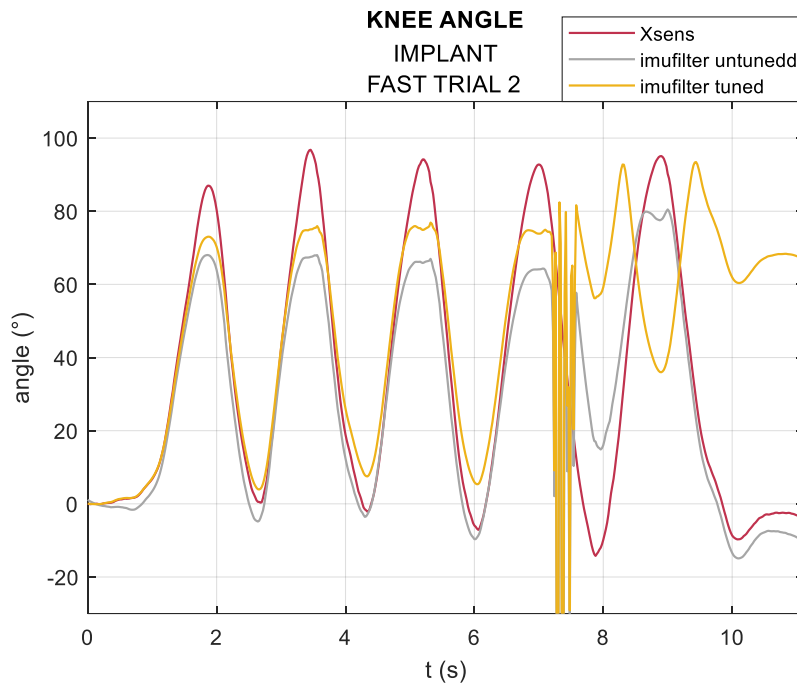


Figure 55 knee angle from orientation output of Xsens, imufilter untuned and imufilter tuned of sensors on implant. Trial 2 fast

So, for the slow trials, the distance between the imufilter orientation output (both tuned and untuned) from aimed orientation (obtained with Xsens) has been calculated, with an appropriate Matlab function, to quantitatively understand derived graphics of the knee angle (figures 48-51). These distances have been compared both for sensors on the implants and for sensors on the rigid part (figures 56-659). For the graphics of the trial 2, on which the imufilter works better, the tuned distance appears significantly lower than untuned distance. A trend is observed in all graphics, representing increasing error during the time, that is in agreement with what observed in precedent plots.

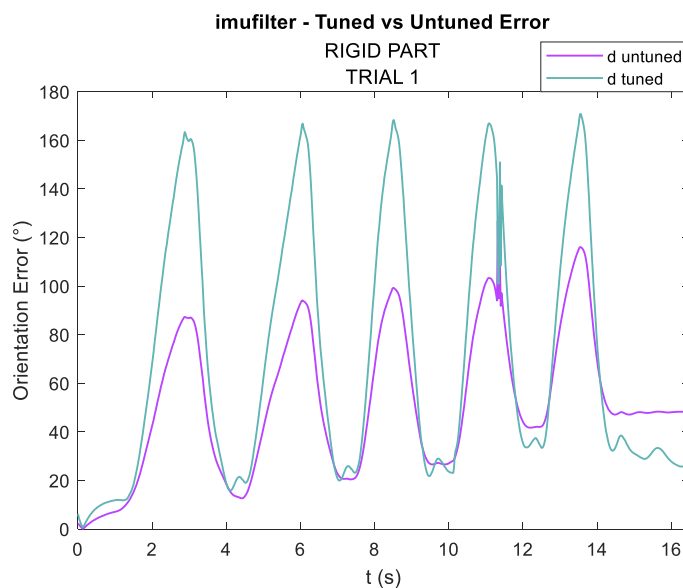


Figure 56 Orientation error: tuned and untuned filter output comparison, for set of sensors on the rigid leg surface. Trial 1

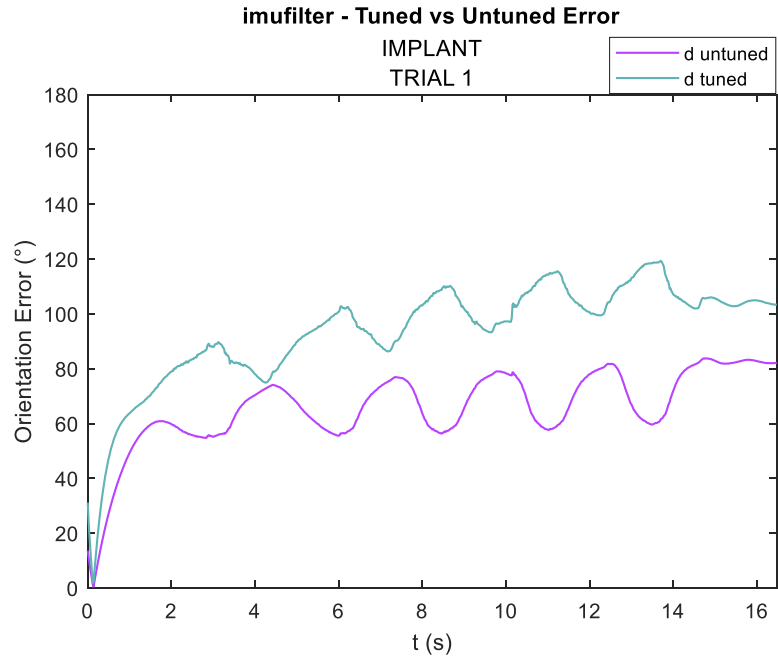


Figure 57 Orientation error: tuned and untuned filter output comparison, for set of sensors on the rigid leg implants. Trial 1

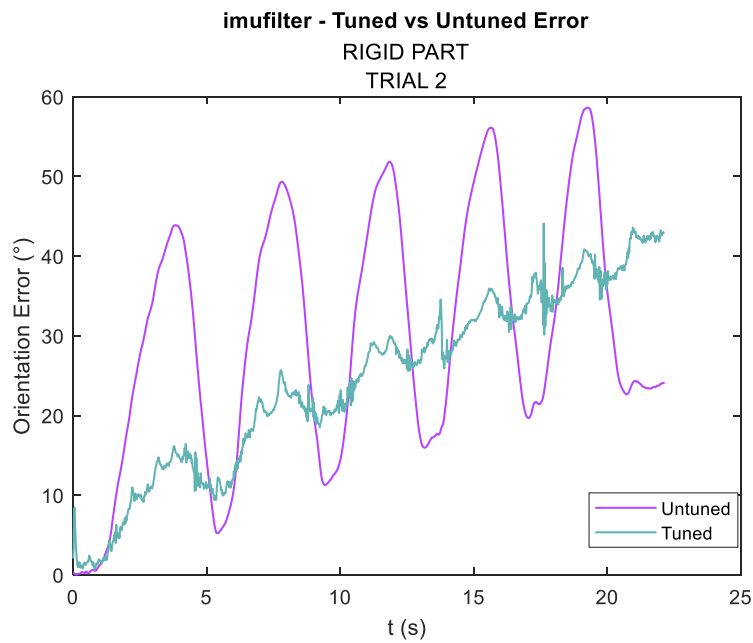


Figure 58 Orientation error: tuned and untuned filter output comparison, for set of sensors on the rigid leg surface. Trial 2

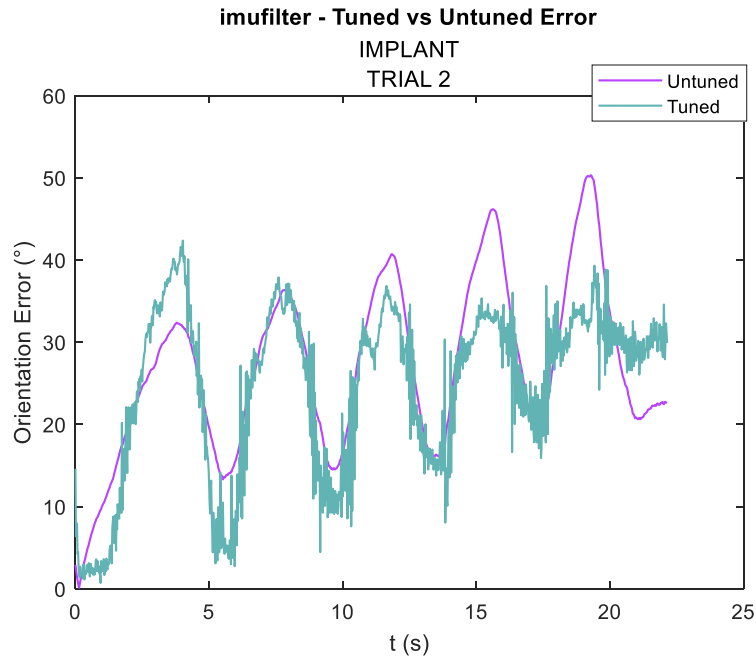


Figure 59 Orientation error: tuned and untuned filter output comparison, for set of sensors on the implants. Trial 2

The Root Mean Square (RMS) of the distance considered have been determined. RMS parameter gives a measure of the estimation error with respect to the orientation computed from the Xsens algorithm. Obtained values are resumed in *table 13*.

$$RMS = \sqrt{\frac{\sum_{i=1}^N d_i^2}{N}} \quad \begin{array}{l} N = \text{samples} \\ d = O_{Xsens} - O_{imufilter} \\ O = \text{orientation} \end{array} \quad (36)$$

The assessment of the RMS parameter allows to observe a lower estimation error for the trial 2 in any considered condition, since RMS values are significantly smaller than those of the trial 1. For the trial 2 it also possible to check that for tuned filter the difference between RMS values for sensor without and with implants under is less than that obtained with the untuned filter. For each trial, for both sensors on implants and on the rigid leg, the imufilter tuned corresponds to a lower RMS value compared to the corresponding RMS from the untuned filter.

Table 13 rms values of sensor orientation calculated with tuned and untuned filter.

RMS (°)						
T1	<i>imufilter</i> untuned	<i>imufilter</i> tuned		T2	<i>imufilter</i> untuned	<i>imufilter</i> tuned
IMPLANT	67.4	95.5		IMPLANT	28.8	26.7
RIGID PART	59.7	86.8		RIGID PART	33.9	26.9

Therefore, the performances of *imufilter* untuned and tuned in absence or in presence of simulated soft simulated soft tissues are compared. Knee angles obtained with both sets of sensors have been plotted on the same graphic as for Xsens initial considerations (*figure 60-63*). RMSE parameter has been determined to evaluate the difference between the two angular signals (*table 14*).

Table 14 RMSE between knee angle estimated from *imufilter* untuned and tuned output, of the two set of sensors utilized, for trial 1 and trail 2. *Imufilter* tuned result compared to those obtained from Xsens measures.

RMSE (°)		
	T1	T2
Xsens	17.2	5.4
<i>Imufilter</i> untuned	15.5	4.8
<i>Imufilter</i> tuned	22.5	9.9

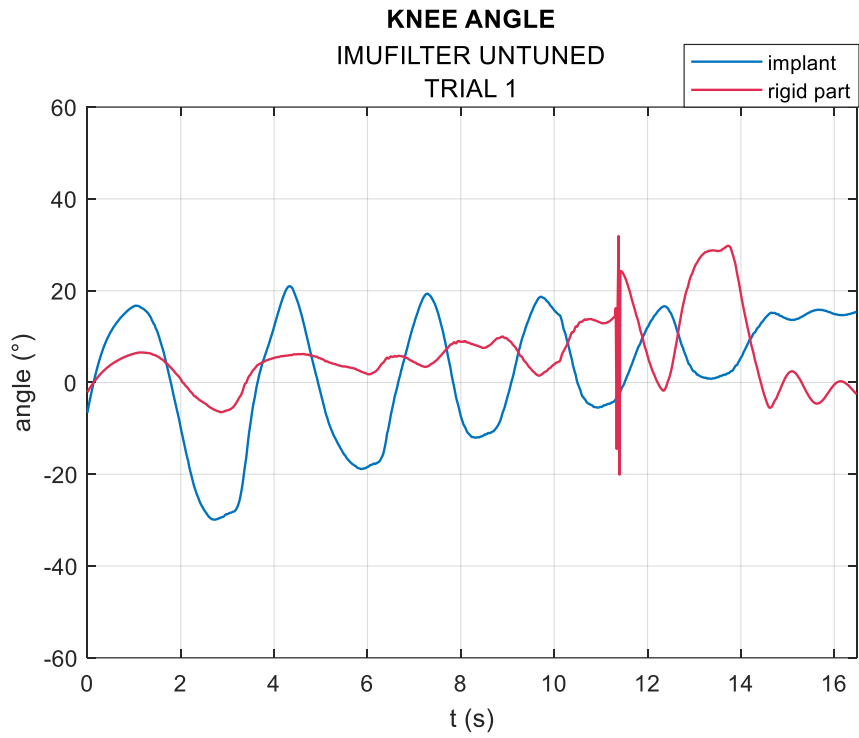


Figure 60 Comparison between knee angle estimated by sensors on the implants and sensors directly on the rigid leg surface, from imufilter untuned orientation estimation. (Trail 1)

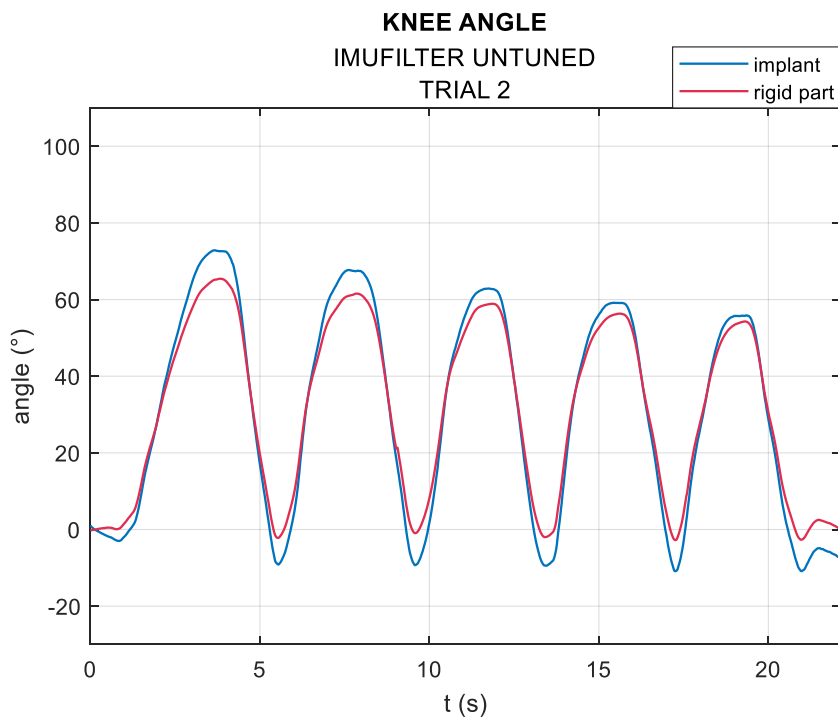


Figure 61 Comparison between knee angle estimated by sensors on the implants and sensors directly on the rigid leg surface, from imufilter untuned orientation estimation. (Trail 2)

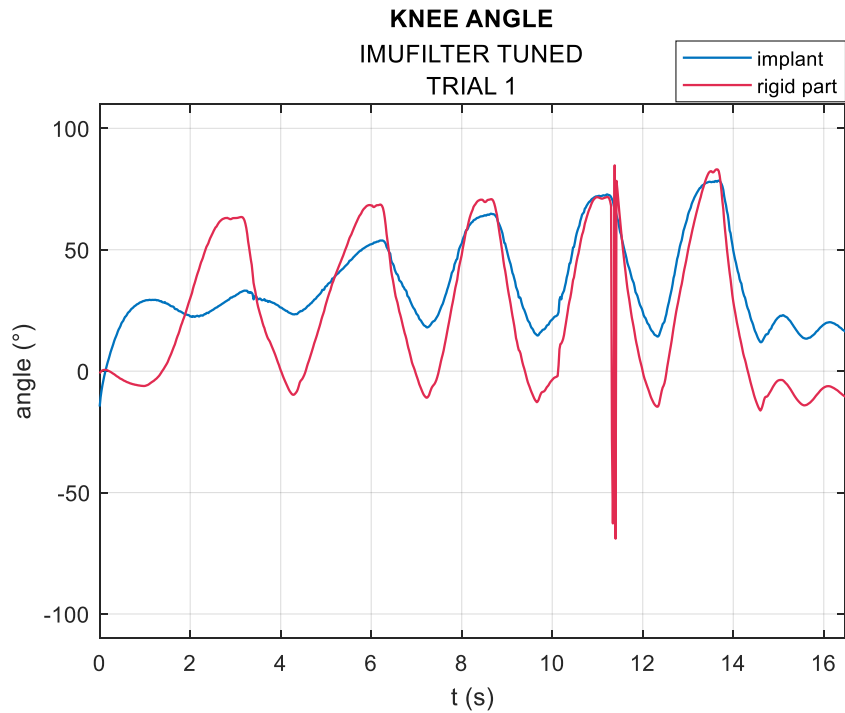


Figure 62 Comparison between knee angle estimated by sensors on the implants and sensors directly on the rigid leg surface, from imufilter tuned orientation estimation. (Trail 1)

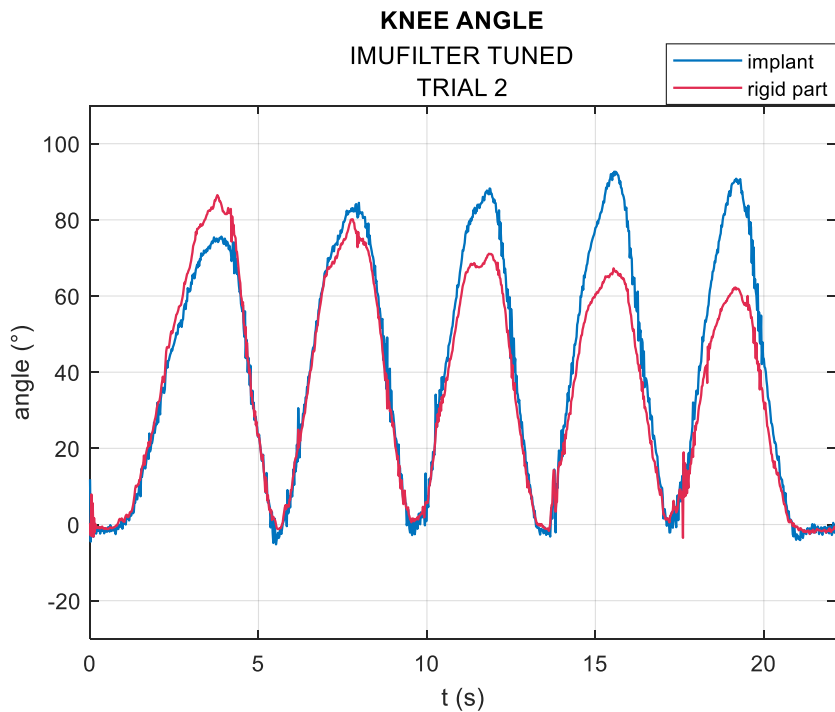


Figure 63 Comparison between knee angle estimated by sensors on the implants and sensors directly on the rigid leg surface, from imufilter tuned orientation estimation. (Trail 2)

RMSE values comparing sensors on rigid leg and on implant calculated from *imufilter* untuned are lower than those calculated from Xsens. It means that the presence of silicone implants does not particularly affect the filter performance. However, considering precedent observations, since this filter does not lead to a good angle estimation, a low RMSE value is a side aspect.

Instead, RMSE comparing sensors on rigid leg and on implant estimated from *imufilter* tuned result greater than those obtained from Xsens orientation output. Indeed, as it can be observed from graphics regarding Xsens measurements (*figures 46,47*), except for the peaks value, the two signals match rather well. The advantage of *imufilter* tuned is that the orientation of the sensor at the end of the flexion/extension movement seems to be better estimated, since relative knee angle signals better represent the peak trend. Nevertheless, RMSE values result higher because two signals in *figures 63* are never as overlapped as are those related to Xsens measures in some intervals. So, although the numerical values do not confirm the improvement in the angle estimation, it is worth considering the contribution of *imufilter* tuned, in addition to Xsens algorithm.

The *imufilter* tuned performance depends on the initial parameters considered for the *imufilter* implementation. Variables optimized by *tune* function are measures of noises variance tolerated by the filter, that define filter accuracy. So, to achieve better results, initial parameters have been changed examining different combinations. Actually, an improvement has been found by increasing noises values, as if the initial implemented filter was too filtering, also in agreement with the obtained lower amplitude values. It is possible that since Xsens sensors tolerate a greater noise than *imufilter* implemented, increasing noise parameters values, the new implemented filter results more similar to Xsens algorithm. It could also be considered that a coarser filter allows to obtain less oscillating orientation values better describing the orientation trend.

To evaluate knee angles obtained with parameters variations and compare them to precedent ones, the RMS value on the distance from Xsens orientation output has been calculated both for untuned and tuned *imufilter* orientation outputs. A resume of attempted parameter changes, and derived RMS values is presented in *table 15*.

RMS defines the discrepancy between the *imufilter* output and the Xsens orientation output, that has been considered the gold standard for these trials. However, the study tries also to understand if using *imufilter* could improve the Xsens algorithm downside, that mainly regards the peaks trend of the knee angle derived from sensors on the implants. To evaluate this aspect, the RMSE between angle signals obtained from sensors attached with or without the silicon implant under them has been considered for any filter implementation (*table 16*).

Table 15 RMS between distance of imufilter tuned or untuned to Xsens orientation. (p=implant, r=rigid part, u=untuned, t=tuned)

RMS (°)											
		default		v1		v2		v3		v4	
Gyroscope noise (rad/s) ²		0.0002		0.002		0.0002		0.0002		0.002	
Accelerometer noise (m/s ²) ²		0.0006		0.0006		0.006		0.0006		0.006	
Linear acc. Noise (m/s ²) ²		0.0025		0.0025		0.0025		0.025		0.025	
		u	t	u	t	u	t	u	t	u	t
T1	p	67.4	65.1	55.5	33.9	66.2	114.4	65.1	45.6	59.8	37.0
	r	59.7	54.8	30.1	14.7	47.6	93.4	23.5	30.1	18.6	13.9
		u	t	u	t	u	t	u	t	u	t
T2	p	28.8	26.7	21.8	20.4	27.6	26.0	27.5	116.7	22.0	14.1
	r	33.9	26.9	25.1	29.1	30.4	26.8	23.0	20.1	19.4	30.3

Table 16 RMSE between angle signals derived from sensors on the implants and from sensors on the rigid part. (v1, v2, v3, v4 refer to parameters variation described in table 14)

RMSE (degree)												
		Xsens	imufilter tuned									
			default		v1		v2		v3		v4	
			u	t	u	t	u	t	u	t	u	t
T1		17.19	15.5	22.5	7.4	17.2	10.8	14.0	18.4	7.6	16.6	14.7
T2		5.38	4.8	9.9	3.0	10.9	4.0	11.9	2.5	12.0	2.2	9.9

In first filter variations, one parameter at a time has been modified to understand which type of result it influenced. Overall, any considered parameter modifications allow to achieve a minor distance from Xsens orientation for sensors placed on the rigid surface of the leg model and also for almost all measurements from sensors on implants. Variation of gyroscope noise (v1) leads to a significant reduction of RMS for both tuned and untuned orientation, and for both trials. Instead,

increasing the linear acceleration noise, result in a greatly reduction of difference between measurements of sensors on implants and sensors on rigid part, for the trial 1; unfortunately, this filter makes worse performance for the trial 2.

Then a fourth attempt was considered, combining all the previous tests and modifying all the parameters at the same time. The filter implemented with these parameters seems, on the whole, to lead to the best results. Therefore, knee angles obtained with sensor tuned orientations, have been analysed comparing them to untuned relative orientation and Xsens orientation. *Figures 64-67* show the graphics that compare the three angles, updated in agreement with the new imufilter implemented.

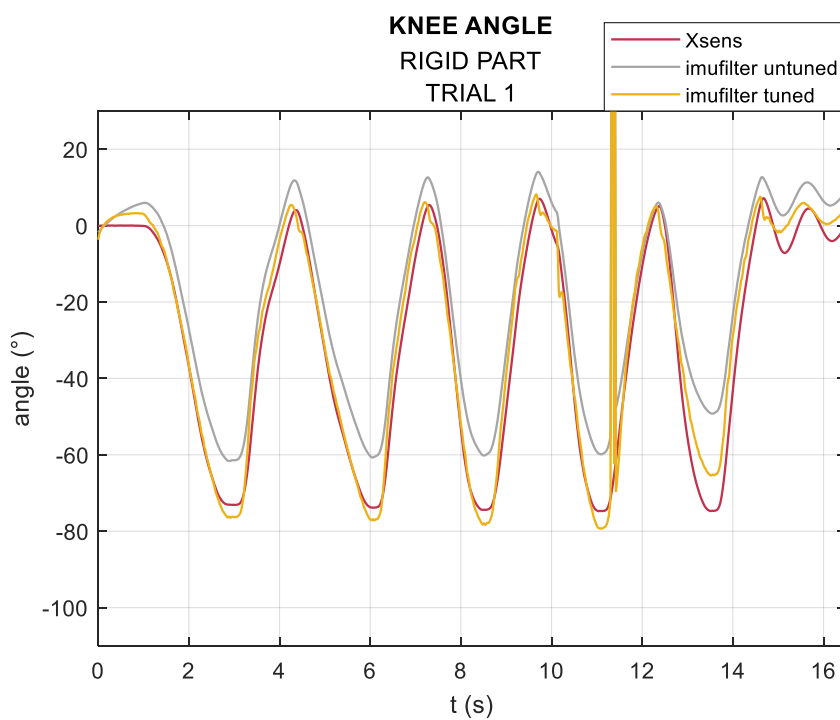


Figure 64 knee angle from Xsens, imufilter v4 untuned and tuned comparison. Trial 1, sensors on rigid part

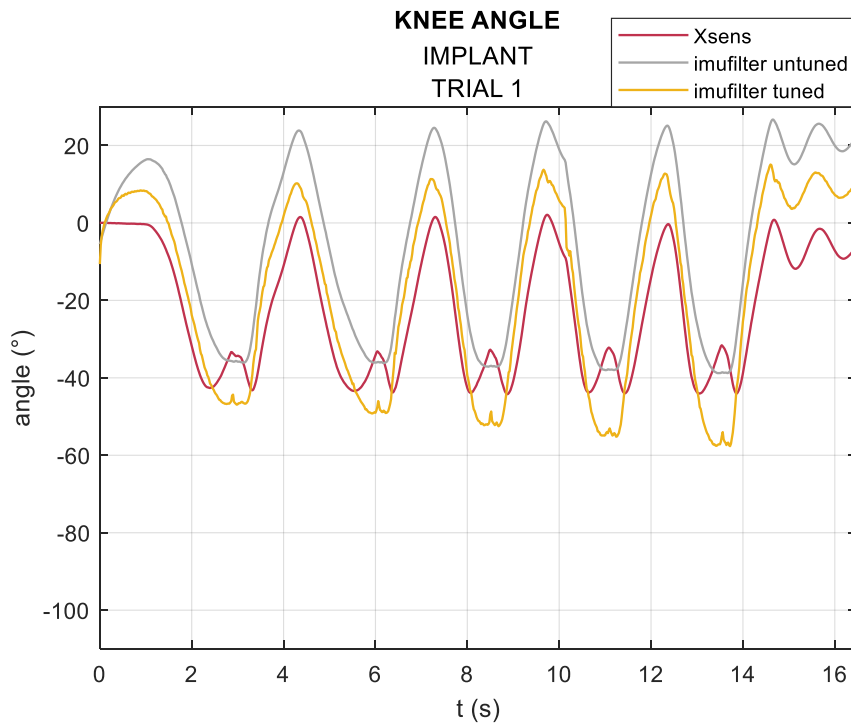


Figure 65 Knee angle from Xsens, imufilter v4 untuned and tuned comparison. Trial 1, sensors on implants

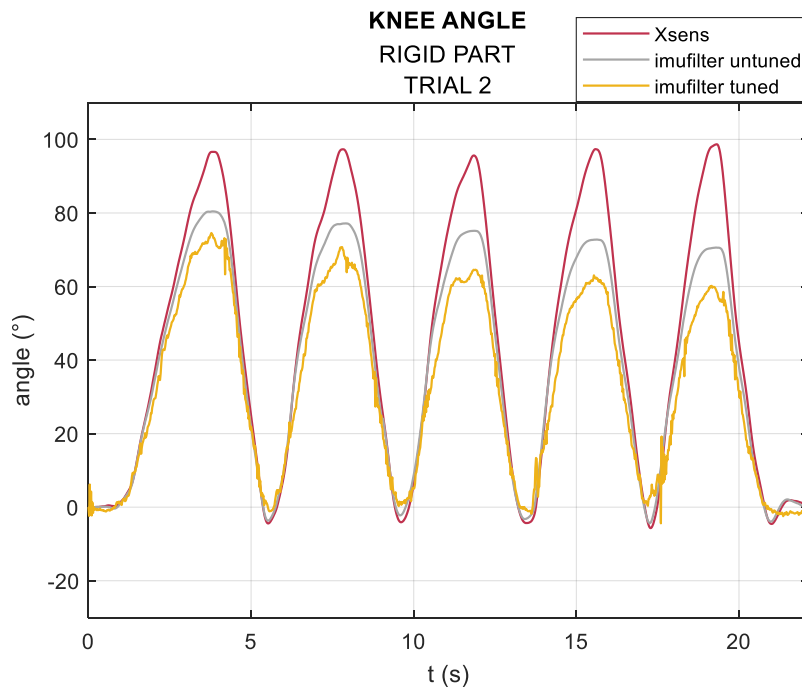


Figure 66 knee angle from Xsens, imufilter v4 untuned and tuned comparison. Trial 2, sensors on the rigid part

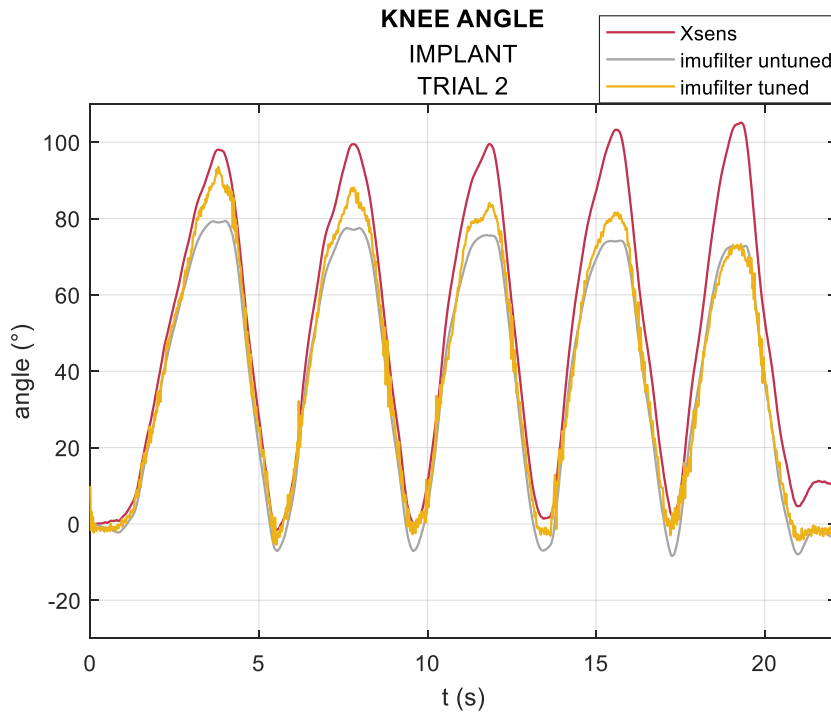


Figure 67 knee angle from Xsens, imufilter v4 untuned and tuned comparison. Trial 2, sensors on the implants

Graphics in figures 68-71 represent the distances between the orientation output from imufilter tuned and untuned, and the Xsens orientation estimation. As expected, based on RMS values calculated, distance from Xsens orientation is evidently smaller than in precedent graphics, especially for the trial 1.

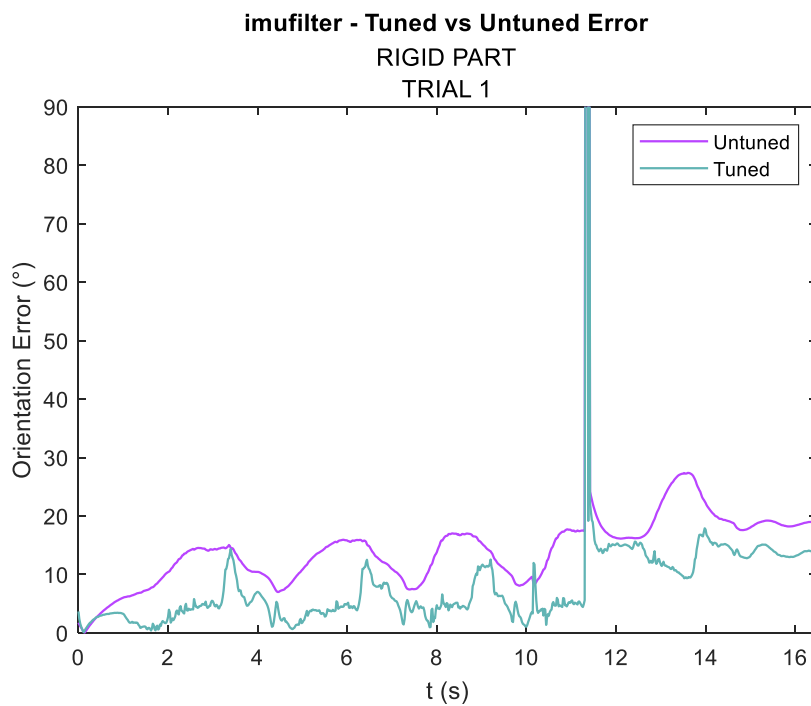


Figure 68 imufilter v4 tuned vs untuned orientation distance from Xsens orientation output. Trial 1, sensors on the the rigid part

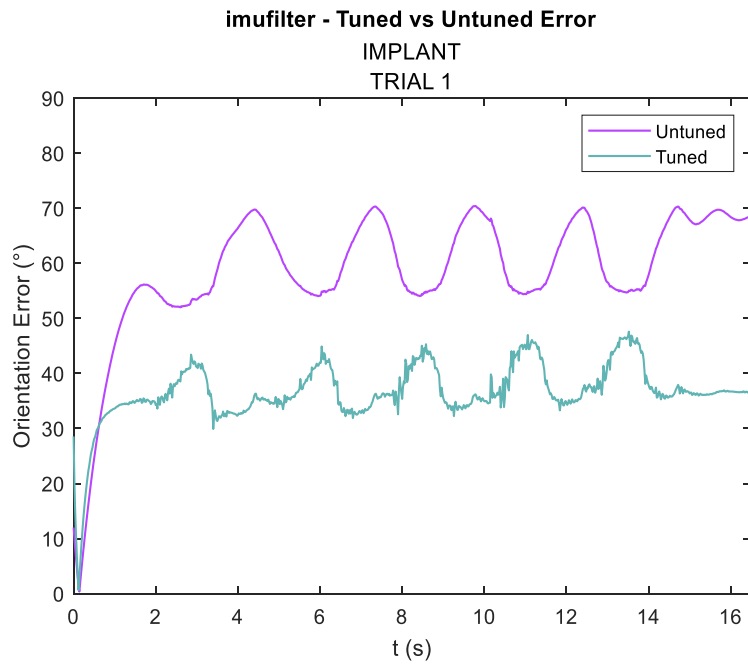


Figure 69 29 imufilter v4 tuned vs untuned orientation distance from Xsens orientation output. Trial 1, sensors on the implants

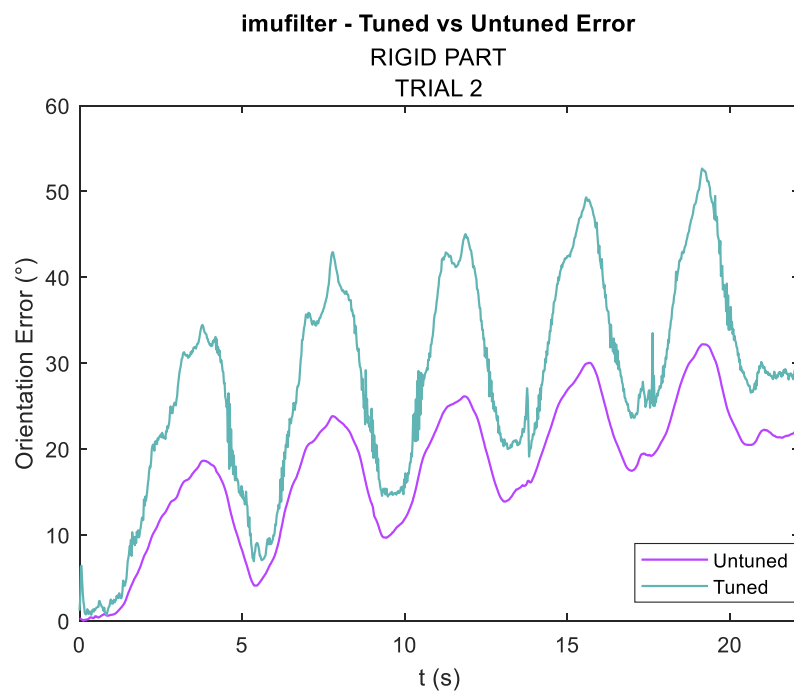


Figure 70 imufilter v4 tuned vs untuned orientation distance from Xsens orientation output. Trial 2, sensors on the rigid part

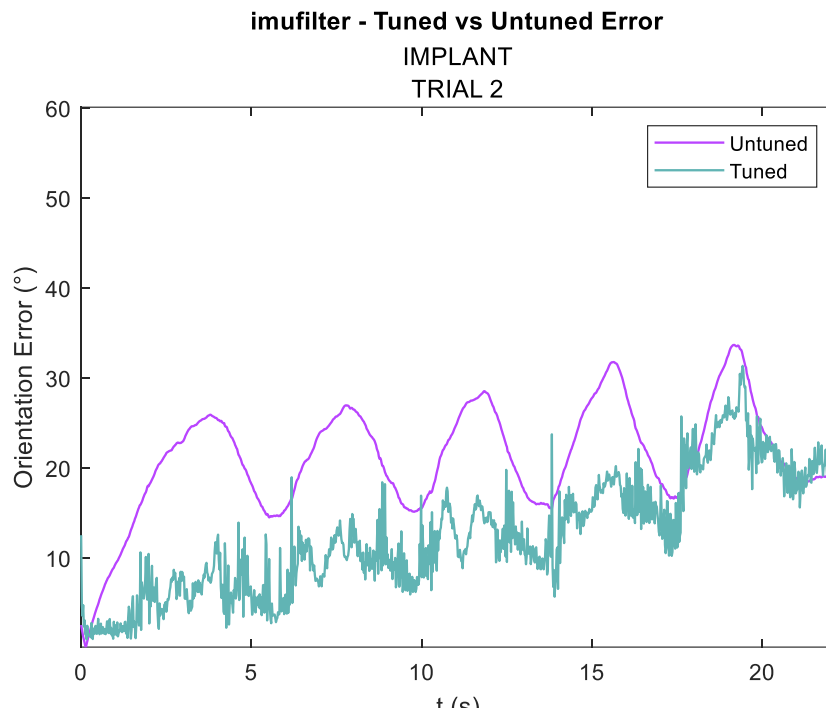


Figure 71 *imufilter* v4 tuned vs untuned orientation distance from Xsens orientation output. Trial 2, sensors on the implants

As it could be already deduced from RMS values, tune *imufilter* in this case has a better performance on the trial 1. Indeed, it starts from a worse untuned orientation, resulting in angle signal more distant from the Xsens goal, and it achieves angles really similar to the ones of Xsens after the tuning of parameters. *Imufilter* tuned applied to sensors on the implant in the trial 1 also allows to reconstruct the peak trend.

Instead, in the trial 2 the tuning of the filter parameters leads to a worse result, as the angle obtained from the orientation output by *imufilter* tuned gets away from the Xsens angle estimated. From this observation it is possible to consider that the type of movement carried out influenced the tuning of the parameters. So, to achieve better results, depending on the movement, it would need to set different initial parameters of the *imufilter* implemented.

Finally, the influence of the simulated soft tissues has been evaluated also for *imufilter* implemented with the described variation (v4). Figures 72-75 show signals directly compared. RMSE values calculated before (table 16) indicate that utilizing *imufilter* tuned v4, in addition to Xsens algorithm, similitude between signals is greater. This observation leaves to deduce a lower dependence of *imufilter* tuned from the simulated soft tissue artifact.

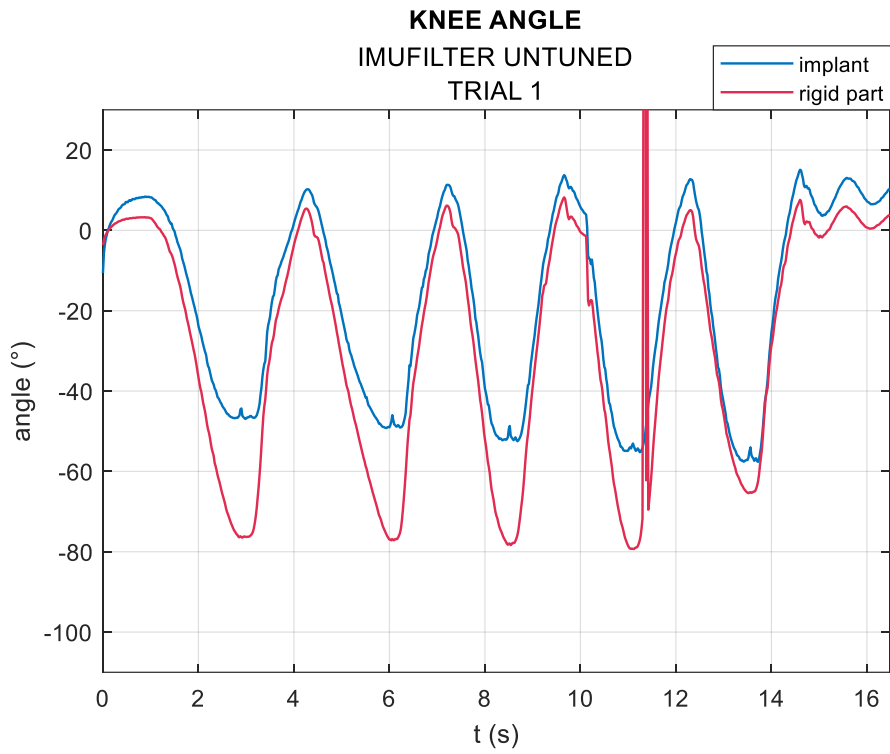


Figure 72 knee angle estimated from orientation output by imufilter (v4) untuned. comparison between measurement from sensors on the rigid part and on the

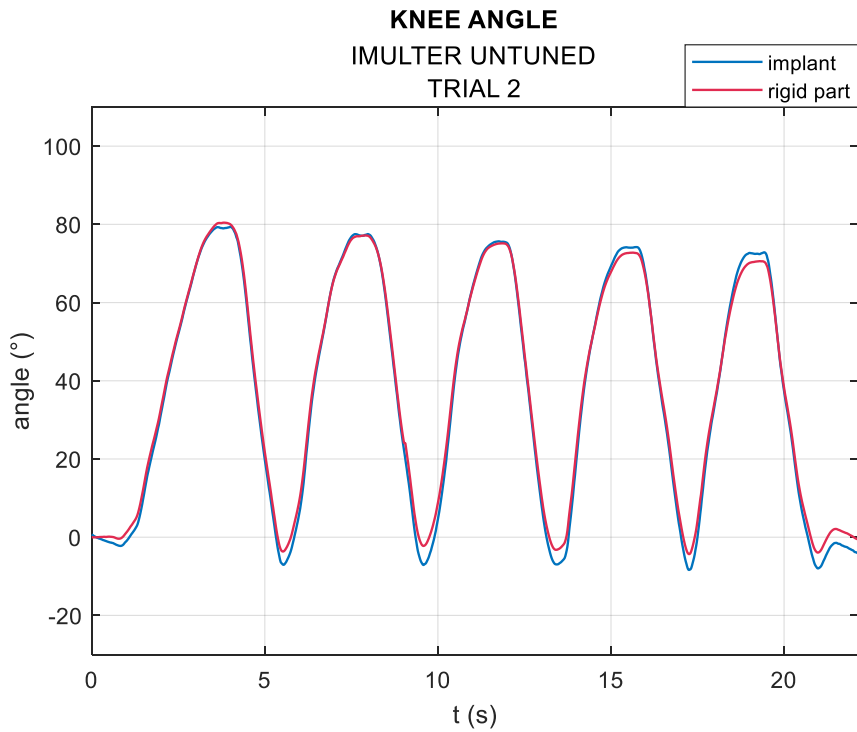


Figure 73 knee angle estimated from orientation output by imufilter (v4) untuned. comparison between measurement from sensors on the rigid part and on the implants. Trial 2

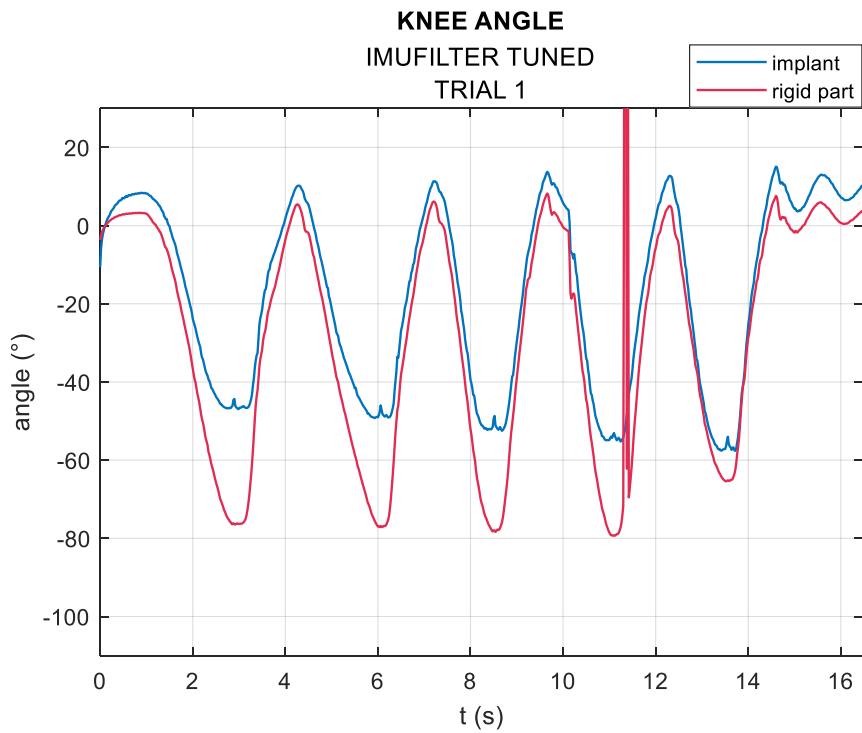


Figure 74 knee angle estimated from orientation output by imufilter (v4) tuned. comparison between measurement from sensors on the rigid part and on the implants. Trial 1

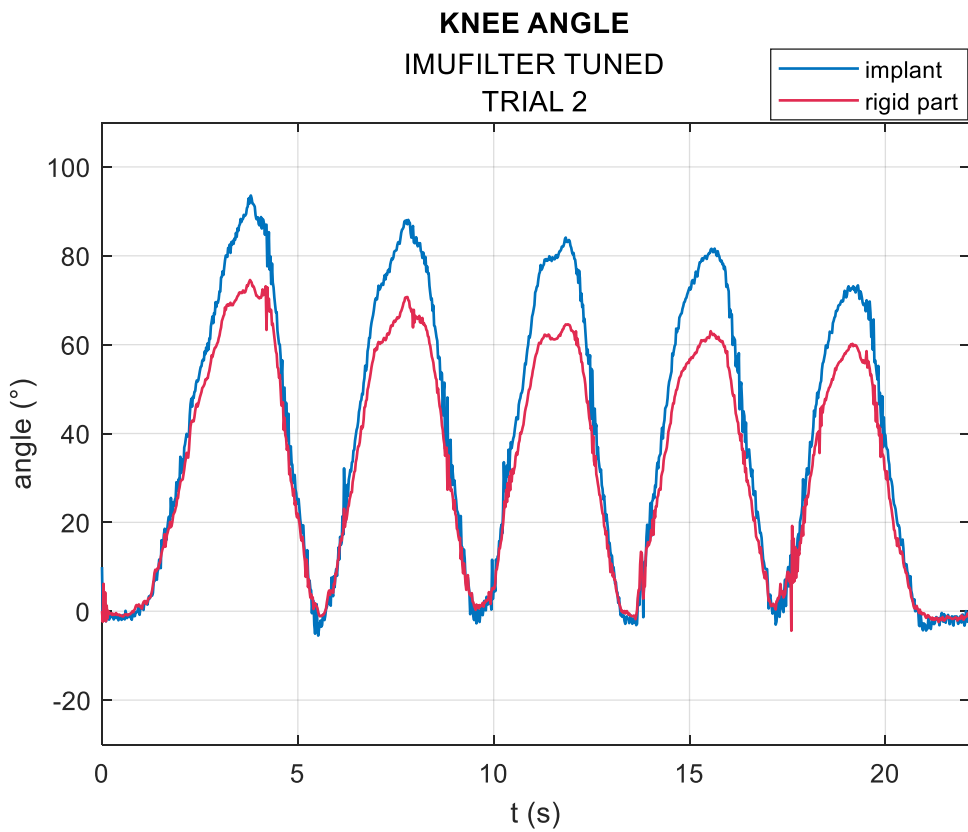


Figure 75 knee angle estimated from orientation output by imufilter (v4) tuned. comparison between measurement from sensors on the rigid part and on the implants. Trial 2

5. CONCLUSIONS

The aim of this thesis was the measurement of the knee angle using IMU sensors in presence of soft tissue. A literature review was carried out to define the state of the art reducing the influence of the soft tissue artifact on the human movement analysis. Indeed, optoelectronic systems represent the gold standard that is usually adopted and on which most of the studies have been carried out. IMUs represent an emerging technology with numerous advantages that can be exploited to obtain promising results. The conducted literature research also moved to deepen the use of inertial sensors on overweight children for gait analysis, since the purpose of this work was to focus on this category. When children are involved, some extra measures should be taken into account, considering that standard protocols could be not usable due to different body dimension or to less collaborative response.

More in detail, this work consists in a pilot study focused on the estimate of the angle between two body segments starting from orientation data of the sensors on them. Accordingly, experimental tests of flexion-extension movements were performed on a leg-model with a polycentric knee, by positioning inertial sensors both directly on the rigid part and on silicone implants simulating soft tissues behaviour.

Preliminary tests carried out with the thigh segment in a horizontal position aimed to evaluate four different configurations of sensors placement and to identify one of them for subsequent tests. The selected configuration provided that the sensor on the thigh was attached on the lateral side and the sensor on the shank was placed on the tibial plateau. Moreover, these initial tests intended to verify the process utilized to estimate angle between two sensors, having as input their orientation with respect to the global coordinate system. In addition, these first tests also assessed the reliability of the Xsens algorithm in presence of simulated soft tissue. Obtained angle signals were compared to angles derived from a 2D evaluation of the movement with Kinovea software. Overall, preliminary tests allowed concluding that the angle estimation process is able to output realistic results, at least in terms of amplitude, and that Xsens measures are not too disturbed by silicone implants effects. Positive angle obtained with two of the configurations may be dependent by sensors positioning, but it is also possible that the estimation procedure is not suitable for any position of the sensors.

Another preliminary test conducted on a participant consisted in a walking trial. Sensors were positioned according to the configuration 1. Results lead to assume that the angle estimation procedure and the Xsens orientation output, in presence of simulated soft tissue, work well.

The effective experimental tests consisted in performing flexion-extension movements on the leg-model. Two different trials were carried out, by positioning the leg both horizontally and vertically. In both trials, two sets of sensors were placed contemporarily on the leg-model, one on silicone implants and one fixed on the rigid model. This configuration allows to directly compare measurements of the two sets, highlighting the soft tissue effects, that resulted more evident for the trial 1, where the RMSE value between the two compared signals was greater.

Then, a sensor fusion procedure was considered to estimate sensors orientation from accelerometer and gyroscope data. The *imufilter* Matlab function was utilized to create an object system based on the inverted Kalman filter, from which the orientation value can be obtained. To assess the suitability of the implemented filter, angles extracted with the precedent procedure were compared to angles obtained from Xsens output orientation. In addition, *imufilter* parameters were optimized with *tune* Matlab function, to improve results with respect to the Xsens ones. From these tests, it can be assumed that *imufilter* tuned could improve results in some case, depending on the performed type of movement.

To make the filter more suitable for sensors characteristics, initial properties of *imufilter* were manually varied to find a combination that led to better results. So, a different *imufilter* untuned and tuned were created and used to estimate sensors orientation. The knee angles calculated with this filter are similar to the Xsens results, meaning that the created *imufilter* has a good reliability. Indeed, the use of *imufilter* *tune* allows in some trials to better reconstruct the shape of peaks. Difference of performance were noticed particularly for angles estimated by sensors on silicone implants.

So, it is worth considering the use of *imufilter* *tune* in addition to Xsens algorithm, for measurement of overweight subject, to achieve better results. A future improvement in this direction could be obtained by defining *imufilter* parameters directly providing a greater performance, without the need to a post-processing with *tune* function and without a dependence from the Xsens algorithm.

REFERENCES

- [1] <https://musculoskeletalkey.com/methods-of-gait-analysis>
- [2] Cereatti, Andrea & Trojaniello, Diana & Della Croce, Ugo. (2015). **Accurately measuring human movement using magneto-inertial sensors: Techniques and challenges**. 2nd IEEE International Symposium on Inertial Sensors and Systems, IEEE ISISS 2015 - Proceedings. 10.1109/ISISS.2015.7102390.
- [3] Caruso, Marco & Knaflitz, Marco & Cereatti, Andrea. (2018). Caruso, Knaflitz and Cereatti: **An innovative MIMU-based procedure for the estimate of the knee flexion-extension angle**.
- [4] Crabolu M, Pani D, Raffo L, Conti M, Cereatti A. **Functional estimation of bony segment lengths using magneto-inertial sensing: Application to the humerus**. PLoS One. 2018 Sep 12;13(9):e0203861. doi: 10.1371/journal.pone.0203861. PMID: 30208109; PMCID: PMC6135500.
- [5] Yuan, Q., I. Chen and A. W. Sin. **Method to calibrate the skeleton model using orientation sensors**, *2013 IEEE International Conference on Robotics and Automation* (2013): 5297-5302.
- [6] Tadano, Shigeru; Takeda, Ryo; Miyagawa, Hiroaki. 2013. **Three Dimensional Gait Analysis Using Wearable Acceleration and Gyro Sensors Based on Quaternion Calculations** *Sensors* 13, no. 7: 9321-9343.
- [7] M. Crabolu, D. Pani, L. Raffo, A. Cereatti, **Estimation of the center of rotation using wearable magneto-inertial sensors**, *Journal of Biomechanics*, Volume 49, Issue 16, 2016, Pages 3928-3933, ISSN 0021-9290,
- [8] Frick E, Rahmatalla S. **Joint Center Estimation Using Single-Frame Optimization: Part 1: Numerical Simulation**. *Sensors (Basel)*. 2018 Apr 4;18(4):1089. doi: 10.3390/s18041089. PMID: 29617331; PMCID: PMC5948776.
- [9] Frick, E. and S. Rahmatalla. **Joint Center Estimation Using Single-Frame Optimization: Part 2: Experimentation**. *Sensors (Basel, Switzerland)* 18 (2018)
- [10] Forner-Cordero A, Mateu-Arce M, Forner-Cordero I, Alcántara E, Moreno JC, Pons JL. **Study of the motion artefacts of skin-mounted inertial sensors under different attachment conditions**. *Physiol Meas*. 2008 Apr;29(4):N21-31. doi: 10.1088/0967-3334/29/4/N01. Epub 2008 Apr 9. PMID: 18401071.
- [11] Igarashi, Y., Akira Komatsu, T. Iwami, Hiroaki Tsukamoto and Y. Shimada. **Comparison of MARG Sensor Results for Different Mounting Positions and Physiques for Accurate Knee Joint Motion Measurement.**, *2019 4th Asia-Pacific Conference on Intelligent Robot Systems (ACIRS)* (2019): 49-52.
- [12] Öhberg, Fredrik, Ronnie Lundström, and Helena Grip. **Comparative Analysis of Different Adaptive Filters for Tracking Lower Segments of a Human Body Using Inertial Motion Sensors**. *Measurement Science and Technology* 24, no. 8 (2013): 085703. doi:10.1088/0957-0233/24/8/085703.
- [13] Montella, Corey. (2011). **The Kalman Filter and Related Algorithms: A Literature Review**.
- [14] Favre J, Jolles B M, Siegrist O and Aminian K 2006, **Quaternion-based fusion of gyroscopes and accelerometers to improve 3D angle measurement** *Electron. Lett.* 42 612-4
- [15] Madgwick, Sebastian O. H., **An efficient orientation filter for inertial and inertial / magnetic sensor arrays**. (2010).
- [16] S. Voss, J. Joyce, A. Biskis, M. Parulekar, N. Armijo, C. Zampieri, R. Tracy, A. S. Palmer, M. Fefferman, B. Ouyang, Y. Liu, E. Berry-Kravis, J. A. O'Keefe, **Normative database of spatiotemporal gait parameters using inertial**

- sensors in typically developing children and young adults, *Gait & Posture*, Volume 80, 2020, Pages 206-213, ISSN 0966-6362,
- [17] Joel L. Lanovaz, Alison R. Oates, Tanner T. Treen, Janelle Unger, Kristin E. Musselman, **Validation of a commercial inertial sensor system for spatiotemporal gait measurements in children**, *Gait & Posture*, Volume 51, 2017, Pages 14-19, ISSN 0966-6362,
- [18] Cutti, A.G., Ferrari, A., Garofalo, P. et al. **'Outwalk': a protocol for clinical gait analysis based on inertial and magnetic sensors**. *Med Biol Eng Comput* 48, 17 (2010).
- [19] Pathare, Neeti PT, PhD; Haskvitz, Esther M. PT, PhD, ATC; Selleck, Marjane PT, DPT, MS, PCS **Comparison of Measures of Physical Performance Among Young Children Who Are Healthy Weight, Overweight, or Obese**, *Pediatric Physical Therapy: Fall 2013 - Volume 25 - Issue 3 - p 291-296* doi: 10.1097/PEP.0b013e31829846bd
- [20] Shultz SP, Hills AP, Sitler MR, Hillstrom HJ. **Body size and walking cadence affect lower extremity joint power in children's gait**. *Gait Posture*. 2010 Jun;32(2):248-52. doi: 10.1016/j.gaitpost.2010.05.001. Epub 2010 May 31. PMID: 20570152.
- [21] Nantel, Julie & Brochu, Martin & Prince, François. (2006). **Locomotor Strategies in Obese and Non-obese Children***. *Obesity* (Silver Spring, Md.). 14. 1789-94. 10.1038/oby.2006.206.
- [22] Cimolin V, Cau N, Sartorio A, Capodaglio P, Galli M, Tringali G, Leban B, Porta M, Pau M. **Symmetry of Gait in Underweight, Normal and Overweight Children and Adolescents**. *Sensors* (Basel). 2019 May 2;19(9):2054. doi: 10.3390/s19092054. PMID: 31052569; PMCID: PMC6539288.
- [23] Madeti, Bhaskar & Rao, Ch.Srinivasa & Pragada, S.. (2015). **Biomechanics of knee joint — A review**. *Frontiers of mechanical engineering*. 10. 176-186. 10.1007/s11465-014-0306-x.
- [24] Galetto M, Gastaldi L, Lisco G, Mastrogiacomo L, Pastorelli S., **Accuracy evaluation of a new stereophotogrammetry-based functional method for joint kinematic analysis in biomechanics**. *Proceedings of the Institution of Mechanical Engineers, Part H: Journal of Engineering in Medicine*. 2014;228(11):1183-1192. doi:10.1177/0954411914559736
- [25] Xsens Technologies B.V, **MTi and MTx User Manual and Technical Documentation**, Document MT0100P, Revision N, 27 May 2009
- [26] Xsens Technologies B.V, **MT Manager User Manual**, Document MT0605P, Revision 2019.A, 11 Jan 2019
- [27] https://en.wikipedia.org/wiki/Soft_tissue
- [28] Sparks, J.L.; Vavalle, N.A.; Kasting, K.E.; Long, B.; Tanaka, M.L.; Sanger, P.A.; Schnell, K.; Conner-Kerr, T.A. **Use of silicone materials to simulate tissue biomechanics as related to deep tissue injury**. *Adv. Ski. Wound Care* 2015, 28, 59–68.
- [29] Thomas Neil Trotta, Marco Island FL (US); Jennifer Anne Trotta, Marco Island, FL (US); Siobhain Lowe, Miami, FL (US), **Human tissue models, materials and methods, patent No US 10,438,510 B2**; October, 8, 2019;
- [30] Frauziols, F., Chassagne, F., Badel, P., Navarro, L., Molimard, J., Curt, N., and Avril, S., 2016, **"In Vivo Identification of the Passive Mechanical Properties of Deep Soft Tissues in the Human Leg"** *Strain*, 52(5), pp. 400–411;

- [31] Cuccaro R, Musacchio C, Giuliano Albo PA, Troia A, Lago S., **Acoustical characterization of polysaccharide polymers tissue-mimicking materials**. Ultrasonics. 2015 Feb;56:210-9. doi: 10.1016/j.ultras.2014.03.018. Epub 2014 Apr 18. PMID: 24794507;
- [32] Kevin M. Moerman, Cathy A. Holt, Sam L. Evans, Ciaran K. Simms, **Digital image correlation and finite element modelling as a method to determine mechanical properties of human soft tissue in vivo**, Journal of Biomechanics, Volume 42, Issue 8, 2009, Pages 1150-1153, ISSN 0021-9290;
- [33] S. Nicolle, P. Vezin, J.-F. Paliarne, **A strain-hardening bi-power law for the nonlinear behaviour of biological soft tissues**, Journal of Biomechanics, Volume 43, Issue 5, 2010, Pages 927-932, ISSN 0021-9290;
- [34] Tang, Wen & Wan, Tao. (2014). **Constraint-Based Soft Tissue Simulation for Virtual Surgical Training**. IEEE transactions on bio-medical engineering. 61. 10.1109/TBME.2014.2326009.
- [35] <https://www.smooth-on.com/products/>
- [36] Holzapfel, Gerhard. (2001). **Biomechanics of Soft Tissue**. The Handbook of Materials Behavior Models. 3. 1049-1063. 10.1016/B978-012443341-0/50107-1.
- [37] <https://www.kinovea.org>
- [38] <https://it.mathworks.com>